Master of Science Thesis

Redesigning the Jockey Seat for fast planing crafts

Integration of composite resilient mounting

Kevin Stouten

Faculty of Aerospace Engineering · Delft University of Technology

TU Delft Delft University of Technology

Redesigning the Jockey Seat for fast planing crafts

Integration of composite resilient mounting

Master of Science Thesis

For obtaining the degree of Master of Science in Aerospace Engineering
at Delft University of Technology

Kevin Stouten

19-04-2018

Faculty of Aerospace Engineering · Delft University of Technology

The work in this thesis was supported by TNO Netherlands. Their cooperation is gratefully acknowledged.

Copyright © Kevin Stouten
All rights reserved.

Delft University of Technology
Faculty of Aerospace Engineering
Department of Aerospace Structures and Materials

GRADUATION COMMITTEE

Dated: 19-04-2018

Chair holder:

Prof.dr.ir. R. Benedictus

Committee members:

Dr.ir. O. Bergsma

Dr.ir. R. Notenboom

Ir. A.W. Vredeveldt

Abstract

In this thesis persistent problems with the shock isolating behaviour of the Jockey Seat are identified and analysed. These Jockey Seat are used on fast planning crafts like the FRISC which is in service with the Royal Netherlands Navy. Past research and existing technology were presented along with two redesign directions. Furthermore, several tools to further analyse the problem in both a static and dynamic setting have been developed.

Both analytical and FE-models were used to efficiently analyse a large amount of design variations. This resulted in the production of a first prototype, the Sigma seat. This seat has been tested both statically and dynamically at TNO. The results have been compared with the static and dynamic models and are in agreement.

Based on the above the author of this thesis concludes that currently used seat cause excessive loads on occupants when the FRISC operates in more severe conditions. Therefore, a redesign like the one proposed in this thesis is necessary. Furthermore, redesigning the seat should focus on the worst-case scenarios for peak accelerations and pulse duration which have been identified.

In the process of (re)designing a combination of static and dynamic models are needed along with testing of prototypes in practice. It is recommended to further experiment with the design tools and develop a solid platform for prototype testing.

Other recommendations are to further experiment with the Sigma seat and research the effects of accelerations and force in planes other than the vertical one. Furthermore, an adjustable damper should be introduced into the design so the seat can be adjusted for different occupant weights.

Table of Contents

List of Figures

List of Tables

Preface

This is my thesis written in fulfilment of the requirements for obtaining my degree in Aerospace Engineering. The topic of choice is a redesign project for the Jockey Seats used on fast planing crafts, which will be further introduced in the first chapter. The creation of this thesis was a long and creative learning process taking its time. Nevertheless, the final product is now in front of you. I would like to take the opportunity to thank the ones involved.

First of all, my supervisor from TNO Netherlands and member of the TNO resilient mounting workgroup, ir. Alex Vredeveldt. As a sparring partner with great in field knowledge and an adaptive way of thinking you have been of great help to me. Dr. ir. Otto Bergsma and dr. ir. Ronald Notenboom for their creative thinking and help with especially the analytical and theoretical parts of my thesis and ensuring my work is up to academic standard. And last but not least, friends and family for their enduring support during challenging times.

Introduction

In the Royal Netherlands Navy the marines make use of the so-called Fast Raiding Interception and Special Forces Crafts (FRISC) for their missions which is shown in figure 1. The FRISC can reach speeds up to 45 knots (80 km/h). During their service time unsatisfactory behaviour of the jockey seats was reported. In extreme conditions, like strong winds and high sea states, the seat is isolating the impact load insufficiently. To gain further insight into the problems concerning the FRISC seats test runs were conducted by the Netherlands Royal Navy (RNLN). Both the 9.6 meter FRISC and the 12 meter FRISC were tested. The crafts were outfitted with the ScottSeat S2J. Several test runs with different speeds and directions have been performed. Furter research done by TNO Netherlands among others confirmed that the problems are caused by the suspension, also called resilient mounting.

This topic is of interest to both the Royal Netherlands Navy and academics. A good resilient mounting will prevent injuries and increase the operational capabilities of the marines. From an academic point of view research into the modelling and development of lightweight high performance suspension, such as this, is taking technology to the next level.

A redesign of the resilient mounting for the FRISC used by the RNLN should be the endpoint of TNO's research. This thesis should serve as a solid foundation in solving the resilient mounting problem. In collaboration with TNO the main research objective was therefore defined as follows:

> Advice TNO Netherlands and the Royal Netherlands Navy by designing a composite suspension for the FRISC with integrated damping and improved characteristics compared to the current design

Figure 1: Example of a FRISC

Chapter 1

Problem Analysis and Diagnosis

This chapter describes the status quo by presenting relevant research on the topic, which is discussed afterwards. Before we continue it is important to elaborate on the current situation. The current designs of resilient mountings consist of steel leaf springs or coil springs, depending on the seat chosen and a separate damping device. These do not perform as desired and the despite a large amount of time spent on theoretical research no practical modification or solution has been found yet.

The main goal of this research project will be to design a new resilient mounting. The design space is limited by physical size and cost. There is freedom in materials and shape. The most important requirement is performance. Preferably, this design is made of a composite. Composites can be tailor-made for specific load cases, offer weight reduction and high strength in combination with large displacements. Also the feasibility of the integration of the damping device in the suspension itself should be investigated.

The initial work for this research project has been done by the RNLN, TNO and the Netherlands Defence Academy (NLDA) providing an excellent starting point. It is therefore of importance to present and discuss the starting point of this thesis. This is done by presenting the problem analysis done by TNO and the bachelor thesis of a NLDA student. While her thesis mainly concerns the problem diagnosis of the FRISC seat suspension problem, this thesis pertains to the design phase of the intervention cycle [9,10]. In the following section results of the problem analysis performed by these participants will be presented and explained.

1.1 Previous studies, problem analysis and diagnosis

Research done by TNO

As mentioned in the introduction test runs were conducted by the Netherlands Royal Navy (RNLN) in collaboration with TNO. These runs were performed with the 9.6m FRISC outfitted with the jockey seat as shown in figure 1.1. The seat is equipped with a coil spring-damper combination and a parallel motion mechanism. This mechanism constrains the motion of the seat in the horizontal plain and allows for movement in the vertical plane. The whole is mounted to the boat with a mounting plate that is connected to the rest of the mechanism. This seat will be referred to as the Parallel Coil Spring jockey seat (PCS).

Figure 1.1: Parallel Coil Spring jockey seat

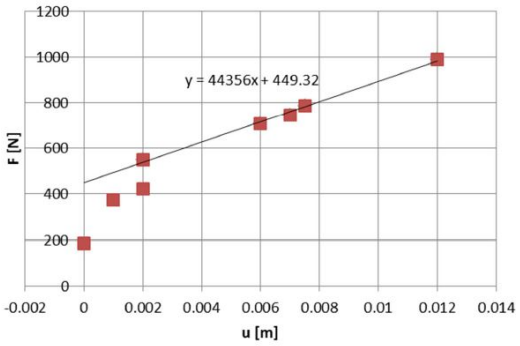

Figure 1.2: Load-displacement for PCS

Before the test runs TNO performed static tests with the jockey seat. The deflection was checked each time a weight was added. The results are depicted in figure 1.2. As can be seen the maximum deflection achieved was about 12 centimetres in combination with a load of 100 kilograms. The resulting average spring stiffness is 44 kN/m. Non-linear effects are seen in the first part of the deflection. These are mainly due to geometric non-linearity as described in [9].

In addition to the static test a dynamic drop test has been performed by TNO. For this purpose a so-called drop tower was used. This tower consists of a 1000 kg drop weight on which two seats are mounted. The drop weight is then hoisted up and dropped from different heights corresponding with the load cases one wishes to verify. Instead of dropping down on the ground the drop weight plunges into a stack of foam blocks. By altering the amount of foam blocks one can influence the duration of deceleration. In appendix A the test set-up is shown.

The base and seat are outfitted with accelerometers. The data provided by these during the drop tests have been processed by TNO yielding the following results. Drop heights of 100, 150 and 200 mm were used resulting in accelerations of respectively 30, 44 and 60 m/s^2 with a pulse duration between 150 ms and 200 ms. The performance of the seat is mediocre at best offering no isolating behaviour at all. This results in passengers being subjected to accelerations exceeding these values. In the 200 mm drop height scenario the seat even hits the bottom support of the suspension. This results in the occupant experiencing an acceleration exceeding 100 m/s^2. This phenomena is called "bottoming" as the suspension is forced beyond the end of it's stroke. A graphical representation is shown in figure 1.3.

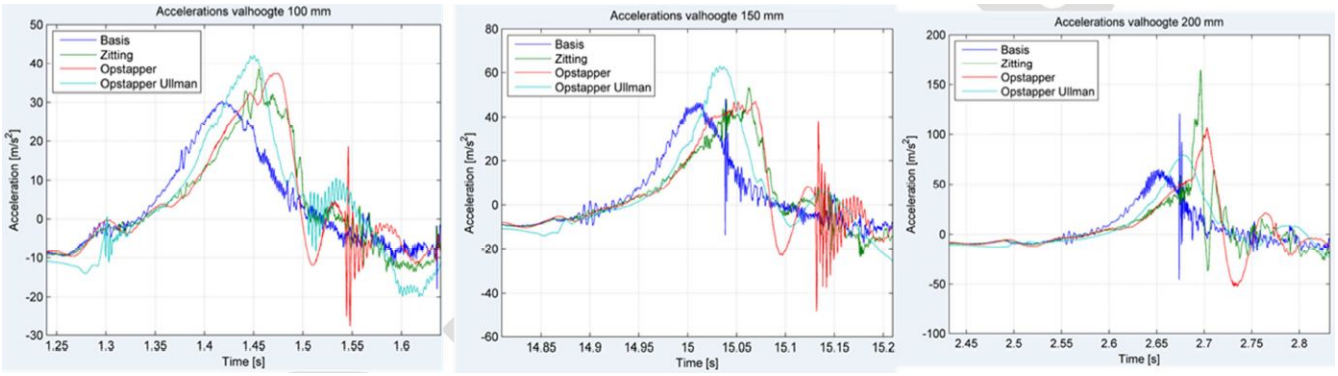

Figure 1.3: Initial pulse and response of drop tower and seat [1]

Research done by the Royal Netherlands Navy

Besides TNO the Defence Material Organisation (DMO) also conducted several tests in the form of sea trials with ScottSeat equiped FRISC's. The speed was varied from ten knots up to thirty knots. The direction was either head sea, following sea or sixty degrees head sea. Results were processed in MatLab, giving results like figure 1.4.

The three graphs represent the accelerations in the x,y and z-direction of the seat. The x-direction is the direction in which the craft travels, the y-direction represents the sideways motion of the craft and the z-direction represents the vertical motion of the boat. The recorders that were used are not able to record rotational accelerations.

Shocks and vibrations in the y-direction are compensated by the occupants own bodies. This is due to the seat design. When using the so-called jockey seats the occupants are required to keep their feet at the crafts deck and clamp their legs around the seat, much like horseriding. The seat itself should isolate the impact events in the vertical x-z plane. The accelerations in the x-z plane can be seen in the third graph of figure 1.4

In figure 1.4 several large peaks can be noticed. The largest peak represents a value of 9g acceleration lasting about 200 ms. Large undesirable accelerations of both the boat bottom and seat are observed. These low frequency impact events are called Repeated Shocks. In contrast to high frequency vibrations, called Whole Body vibrations, Repeated Shocks pose a bigger risk for the crew and can cause serious injury.

Furthermore, it is important to realize that these shock loads not only lead to physical injury but are also experienced as physically exhausting. According to research done by the United Kingdom's Ministry of Defence the performance of marines can drop up to 26 % after a rough RIB transfer with unsuspended seats [11].

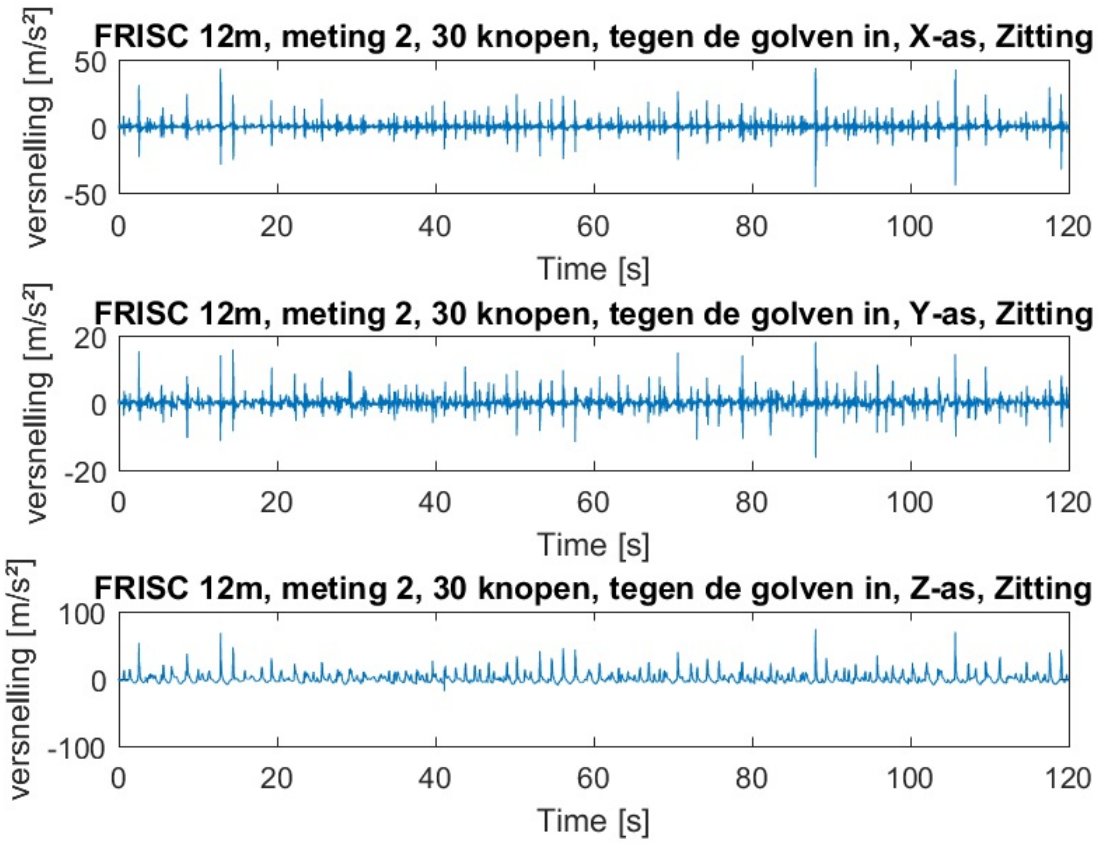

Figure 1.4: Example of FRISC test run measurement at 30 knots with head sea [1]

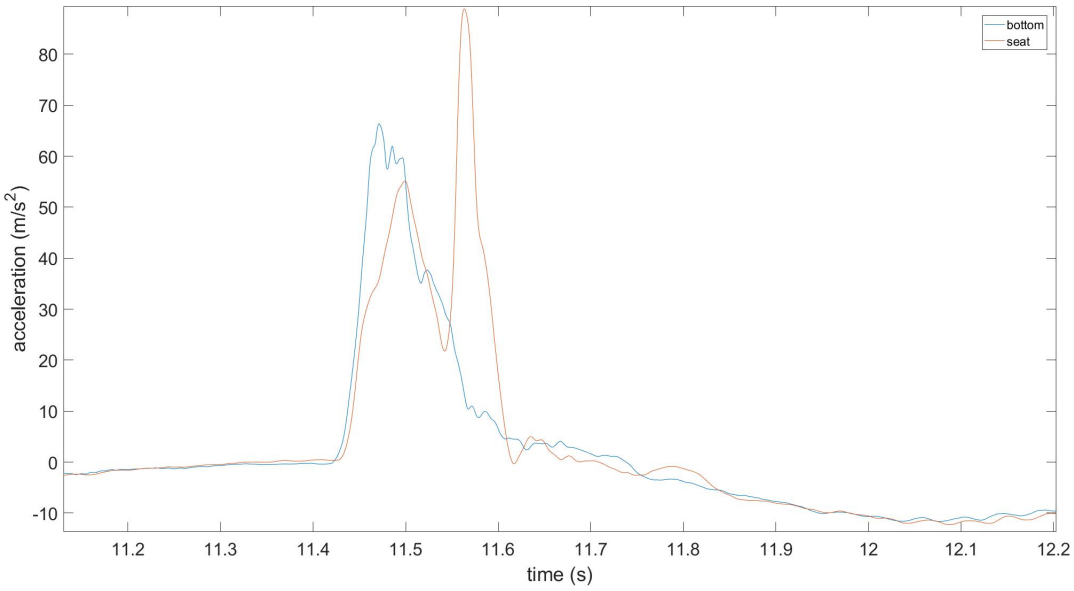

Figure 1.5: A representative pulse from a 9.6m FRISC test run

The results of the problem analysis have been processed into a final test report [12] with the most important conclusions being:

- The resilient mounting does not perform as desired and needs to be changed.
- The impact events on the FRISC 9,6 meter are more severe than on the FRISC 12 meter
- Repeated shock pose a bigger risk than Whole Body Vibration
- Peak loads occur occasionally increasing the risk for acute injury.
- The load does not only cause acute injury but is also physically exhausting

Research done by the NLDA

As mentioned before the problem has been further analysed by NLDA student. To further analyse the problem this student has developed a calculation model simulating the PCS jockey seat behaviour. This model is based on the Euler-Lagrange equations in which the seat is regarded as a mass-damper system. The model has been validated by a number of standard drop tests performed at TNO. A representative impact event can be defined from these measurements together with literature about impact events [13]. This representative impact event can be seen in figure 1.5.

Subsequently, A simplified acceleration pulse simulating a single impact event based on figure 1.5 was used as an input for a mass-spring-damper model. The pulse shape is that of a sine wave and an example can be seen in figure 1.6. In this example the input pulse has an amplitude of 40 m/s^2 and a pulse duration of 200 ms. The value of amplitude of the input pulse will be discussed later.

It is noted that a pulse with an amplitude of 40 m/s^2 was used. However, the amplitude of the pulse was of minor importance in the research thesis referred to here. The pulse has been used to investigate the effect of changing variables and system parameters for the PCS jockey seat in particular. Finally, a list of adjustments is suggested by the author to achieve the desired improvements in the system's parameters.

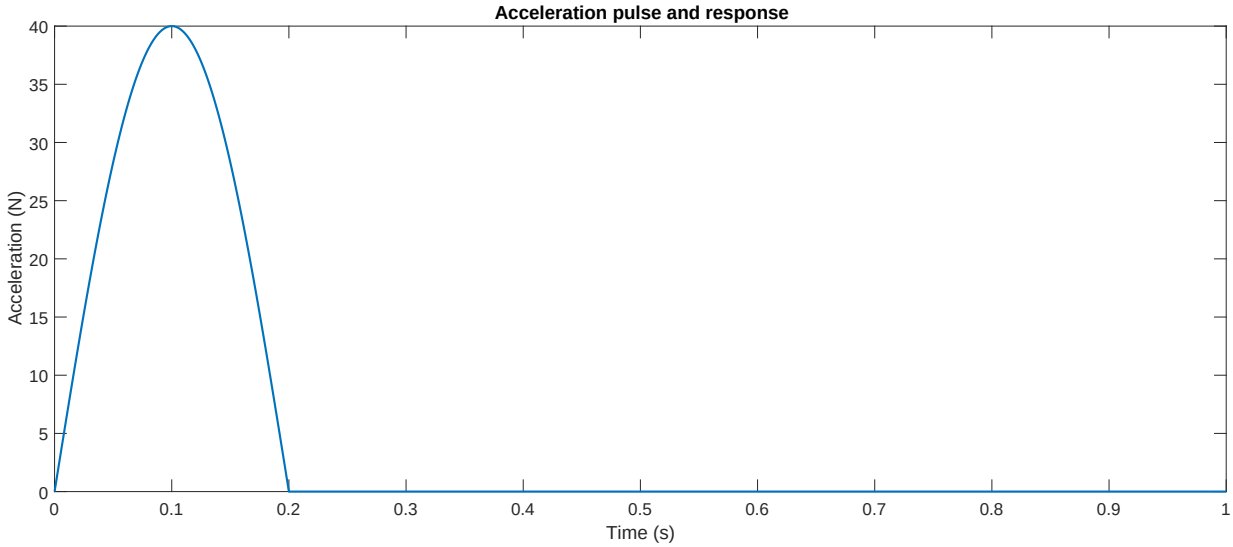

Figure 1.6: Simplified acceleration input pulse of 200ms

The most important relevant observations made [9]:

- The travel of the resilient mounting is about 7 centimetres instead of 15 centimetres mentioned in the specifications [14].
- In case of peak loads the resilient mounting tends to "bottom out". During this bottoming extreme accelerations, exceeding 15g, have been measured. These are acting on the seat and thus the human subject.
- The impact event can be simulated by a simplified half sine pulse with a pulse time of 200 milliseconds and a peak value of 4g.

The most important relevant conclusions and recommendations drawn:

- To prevent the mounting from bottoming out the spring travel, stiffness and damping should be increased.
- To improve the shock isolating behaviour of the system the spring stiffness and damping should be decreased, which conflicts with the first conclusion.
- The spring stiffness and damping coefficient of the ScottSeat might not be constant but displacement dependent. It should therefore be determined more accurately.
- The integration of an extra damping device at the bottom out points should be researched
- Seats have to be easily adjustable to the person's posture.
- Regulations for Whole Body Vibration and Repeated Shocks are not clear enough.

1.2 Discussion

The problem analysis and diagnosis will be presented along with supporting arguments and calculations. First the excitation pulse will be discussed and four worst-case excitation pulses will be presented. These have been analysed with a mass-spring-damper model.

Excitation pulse

Aside from TNO more research regarding impact for fast raiding crafts has been done by T.E Coe et all [2]. They not only identified representative impact events, but also gathered a large amount of data concerning pulse duration and maximum acceleration. This data was gathered during a large amount of test runs. The results can be seen in figure 1.7.

The FRISC weighs around 7500 kg. This weight class is represented by the blue dots in figure. 1.7. The load cases with the longest impact duration and highest peak acceleration are the most interesting when designing a new resilient suspension, because these load cases result in the maximum responses one may expect during a run.

Therefore four distinctive representative load cases have been selected from figure 1.7. These are indicated by the letters A till D. Where A represents a peak acceleration of $3.9g$ with a impact duration of $290ms$, B is located at $4.8g$ and lasts $250ms$, C at $5.6g$ and lasts $210ms$ and finally point D, which is located at $7.1g$ and lasts $135ms$ in figure 1.7.

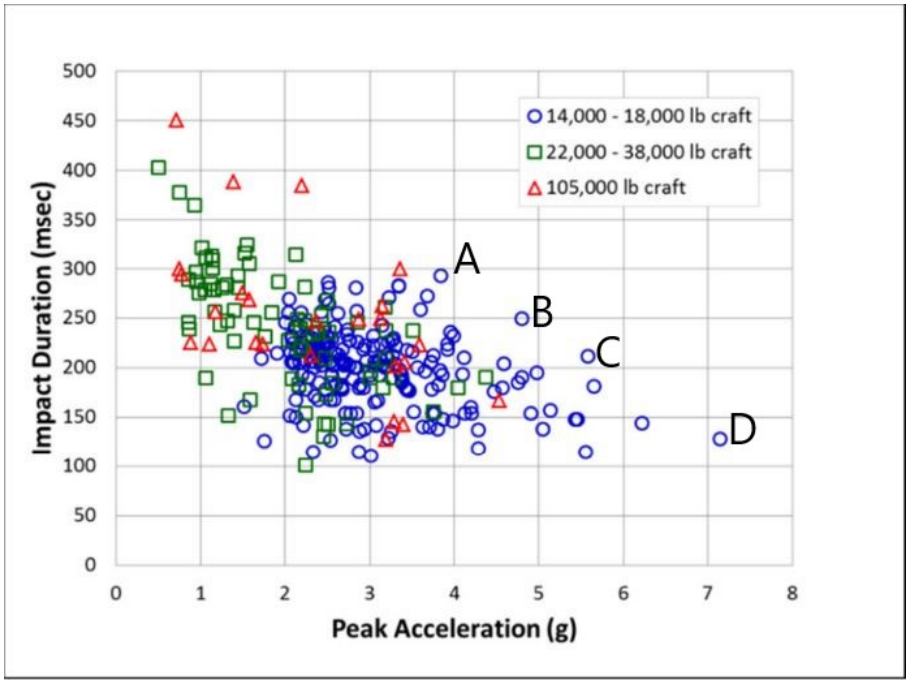

Figure 1.7: Full-Scale Data Impact Duration versus Peak Acceleration [2]

The shape of the these pulses is described by a half sine wave in agreement with the research presented earlier and in redesigning the jockey seat these are the load cases one should design for. The load cases will all be used as an input for the dynamic model based on a mass-spring-damper system. This will be discussed next.

Load case study with MatLab

To study the response to the earlier presented load cases a simple but effective mass-spring-damper model has been constructed. The model is based on Newton's equations of motion with base excitation, which agrees with the behaviour one can expect for a craft slamming on the water. It's behaviour has been validated through comparison with earlier mentioned literature and is in agreement. The numerical integration in the MatLab environment is performed according to the Midpoint method. It is a second order method for numerical integration. All relevant information can be found in appendix B.

These equations of motion and numerical integration will be used in the remainder of this thesis to analyse the response of our designs. When needed the calculation model will be expanded, for example to include pretension of the resilient mounting or to cope with non-linear spring characteristics. Next the effects of the four identified worst case scenarios and the effect of changing the variables for a reprensetative jockey seat will be demonstrated.

First the model's response for the four load cases mentioned previously will be presented. The stiffness is set at 40.000 N and the damping coefficient at 1000 kg/s. A mass of 100 kg is used. When compared to existing designs, this approximates the behaviour of the currently used PCS jockey seat and therefore is a reasonable first estimate to demonstrate the validity of the dynamic model and the effects of worst case scenarios. A graphical representation for load cases C and D can be seen in figures 1.8 and 1.9. The results for load cases A and B are included in appendix B.

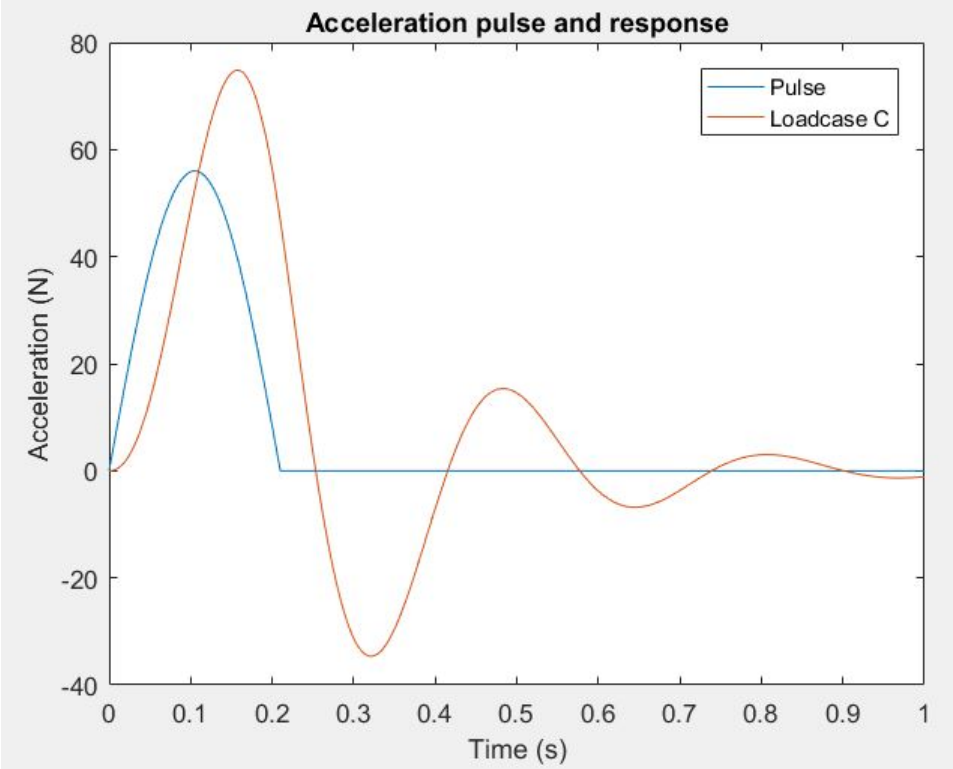

Figure 1.8: Response for loadcase C

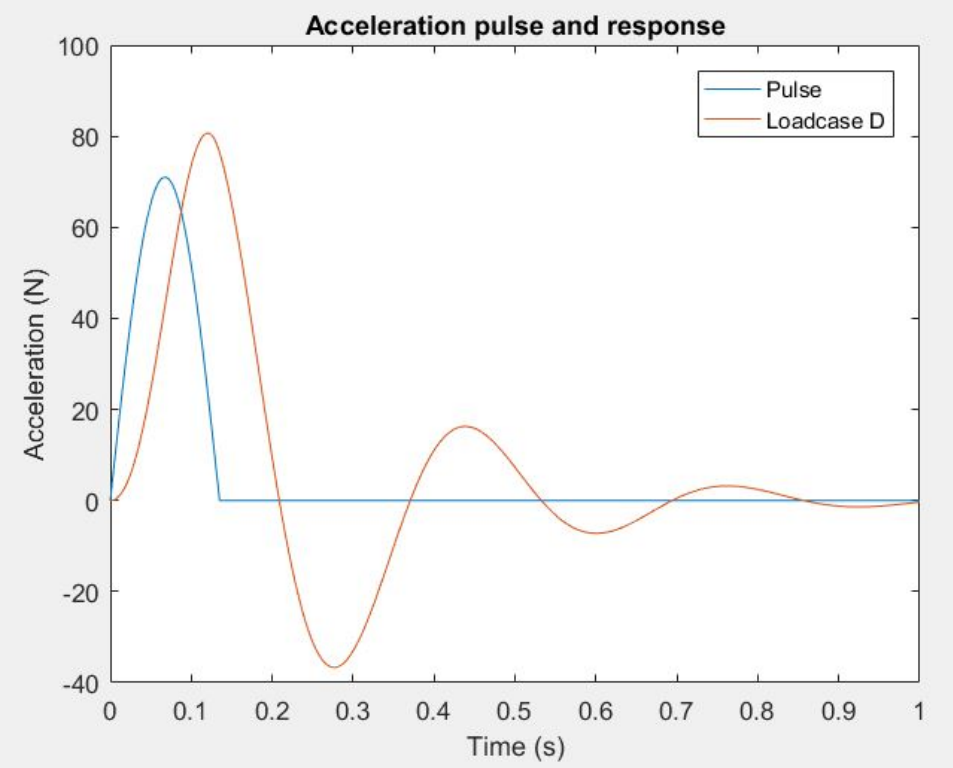

Figure 1.9: Response for loadcase D

As can be clearly seen, the resulting acceleration experienced is higher than the excitation pulse in all load cases. In other words, the excitation pulse is actually amplified by the suspension increasing the load on the occupants. In reality, the results are even worse, because of the bottoming that occurs for this type of seat. The bottoming phenomenon has been discussed in the preceding section. The effects of bottoming have been incorporated into the model for loadcase C and the results are shown in figure 1.10. The almost instantaneous increase in acceleration to 230 m/s^2 is clearly visible.

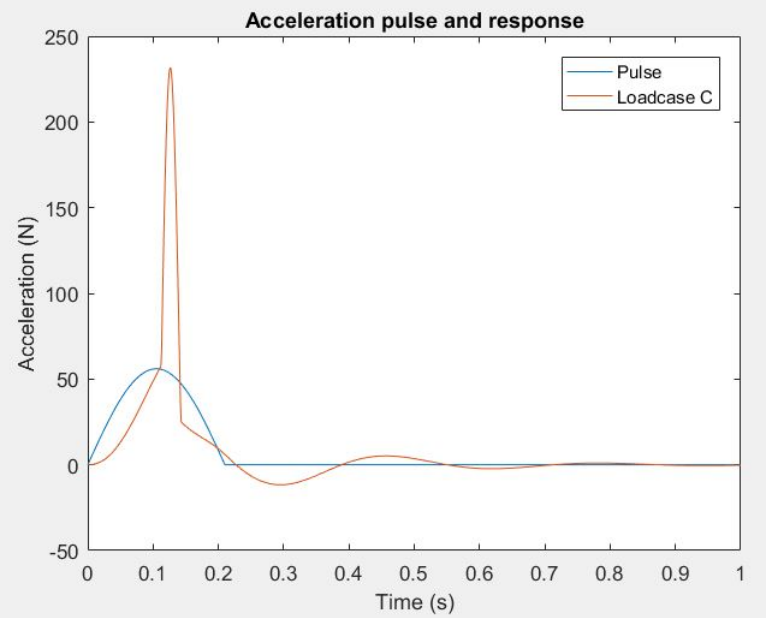

Figure 1.10: Response to load case C including bottoming

Bottoming can be prevented by designing a suspension with an improved maximum compression. Equally important is the question how to assure the design does not amplify the excitation experienced. To elaborate on this topic we introduce the amplification factor. The amplification factor is expressed as follows:

$$A.F. = \frac{A_{seat}}{A_{pulse}} \tag{1.1}$$

In equation 1.1 A_{seat} is the maximum acceleration of the seat and A_{pulse} the maximum acceleration of the pulse. A value above 1 indicates amplification, while a value below 1 means the resilient mounting is isolating the shocks it experiences. For example, the amplification factor for the system undergoing load case A as featured in figure B.2 has an amplification factor of 1.36.

Next, we define the relationship between the eigenfrequency of a mass-damper system and its stiffness and mass. We also introduce the ratio of the excitation pulse duration and the period belonging to the eigenfrequency of the system. In mathematical notation:

$$\omega = \sqrt{\frac{k}{m}}, \text{thus:} \qquad k_{eigen} = (2 \cdot \pi \cdot f_{eigen})^2 \cdot m \tag{1.2}$$

$$r = \frac{t_n}{T_D} \tag{1.3}$$

Now the amplification factor is shown as result of changing the stiffness of the system. When changing the stiffness, the frequency of the system is also changed. In figure 1.11 and 1.12 the ratio between the excitation pulse duration (t_n) and the period of the Eigenfrequency (T_D) is shown as a function of the amplification factor. This is done for a system without damping and for a variation of damping coefficients expressed as a percentage of critical damping. A mass of 50 kg is used. Results are in agreement with Chopra [15]

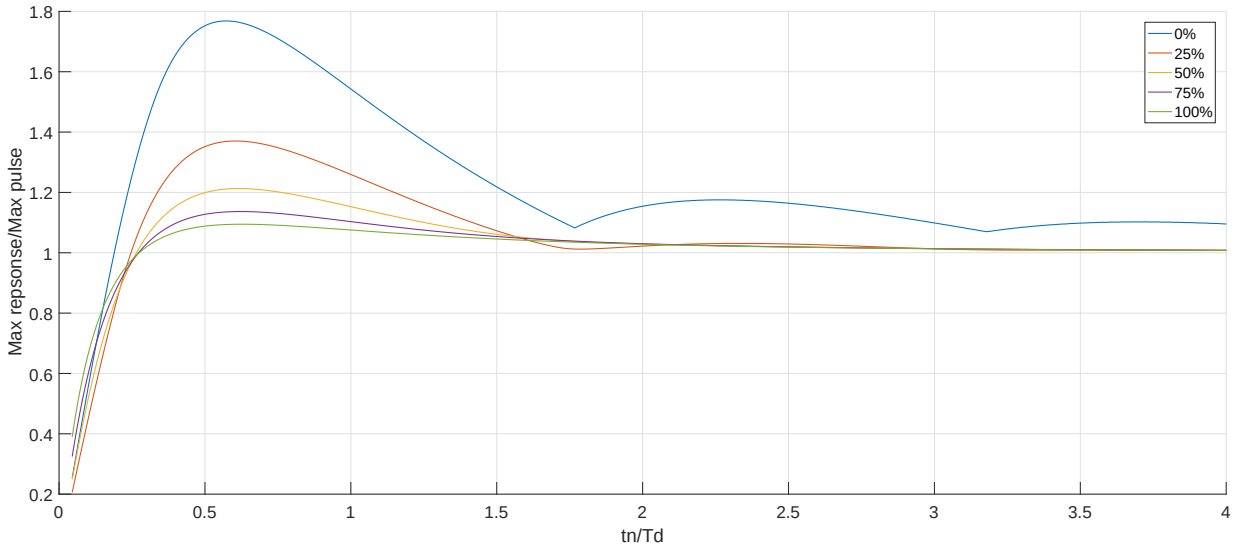

Figure 1.11: Amplification factor up to r=4

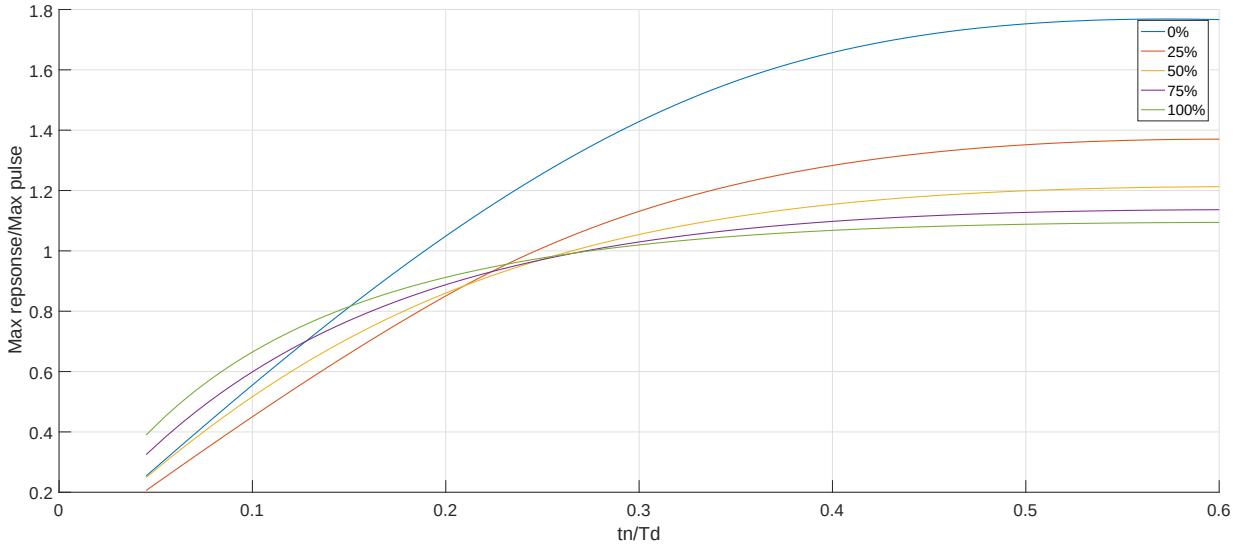

Figure 1.12: Amplification factor up to r=0.6

Only the area in which the shock is isolated is of interest. Therefore t_n/T_d is shown for a value up to 0.6 in figure 1.12. A damping ratio of 25% with regard to critical damping gives the best results for a value of t_n/T_d up to 0.2 which corresponds to a stiffness of 1974N for a pulse duration of 200 ms and a weight of 50 kg:

$$k_{eigen} = (2 \cdot \pi \cdot \frac{r}{t_n})^2 \cdot m = (2 \cdot \pi \cdot \frac{0.2}{0.2})^2 \cdot 50 = 1974N \tag{1.4}$$

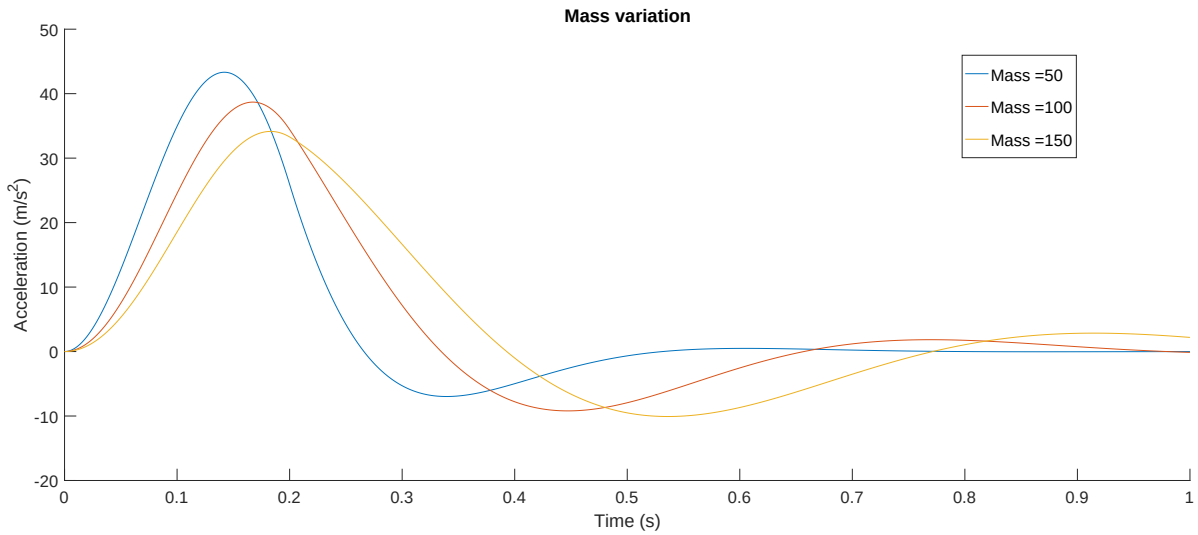

Figure 1.13: Mass variation

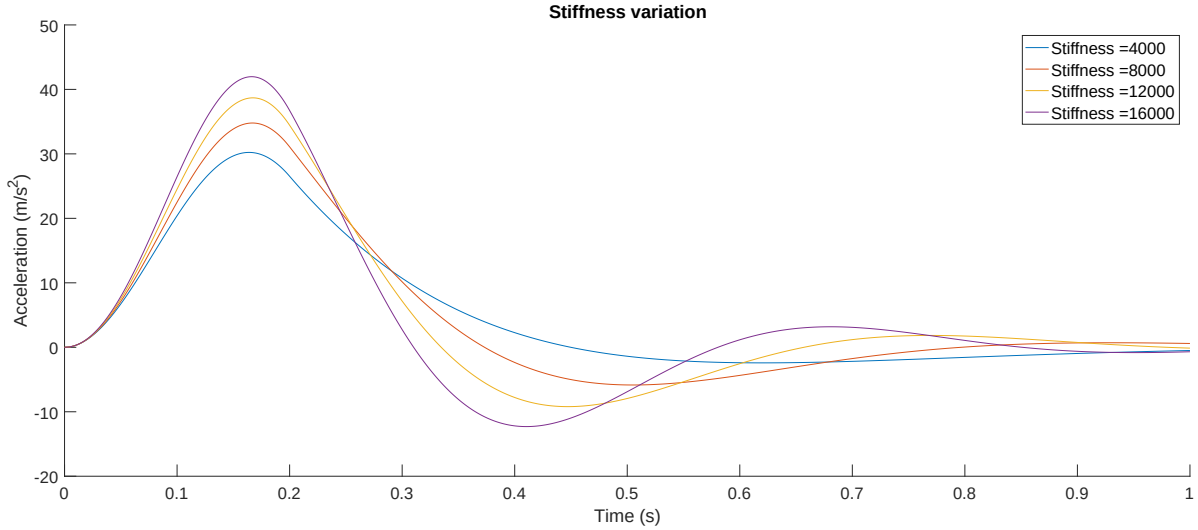

Figure 1.14: Stiffness variation

Next, the effect of changing the variables mass, stiffness and damping (m, k, c) for a fixed input pulse will be demonstrated. This is the logical next step to get a deeper understanding of the way the system behaves.

In figures 1.13 and 1.14 the mass and stiffness are varied over a range under the influence of an arbitrary input pulse to study their effects on the seat response. In figure 1.13 the mass was changed keeping all other variables constant. A value of 12 kN has been used for the stiffness. Clearly, increasing the mass has a beneficial effect on the response of the seat in terms of acceleration. Lowering the stiffness has the same effect as can be seen in figure 1.14. Here the mass was kept constant at $100kg$. This is in accordance with the equations of motion, which state that a higher mass lowers the Eigenfrequency.

Figure 1.15 shows the seat response for a variation of damping coefficients. The damping variation seems to have less influence on the isolating behaviour of the resilient mounting. A higher damping coefficient forces the seat to follow the motion of the base of the boat thus transfering all shocks to its occupants.

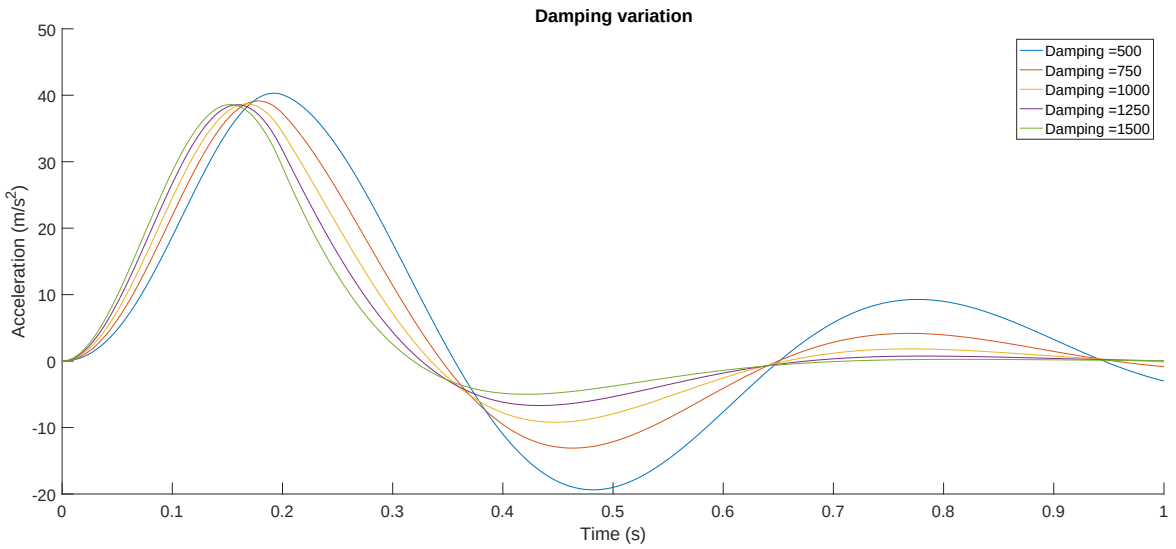

Figure 1.15: Damping variation

One has to keep in mind though that in practice it might proof very difficult to change some of the variables discussed or that variables are not independent of each other. Variables that are unchangable in reality include the pulse duration and the maximum compression of the resilient mounting once produced.

Up untill now, the maximum compression has not been discussed elaborately. It was already mentioned that "bottoming" of the resilient mounting is a persistent problem and the foregoing consideration about the Eigenfrequency, pulse duration and other involved variables have led to the conclusion that slack suspensions have the potential to outperform their stiffer counterparts. Though, lowering the stiffness too much will also lead to an undesirable increase in compression of the spring.

To further illustrate this several tables have been created to show the influence of the discussed variables on the isolation factor and maximum compression. An input pulse with a duration of 200 ms was used. This requires a stiffness of the resilient mounting of 12.337 kN/m or less for shock isolation.

The first table shows the amplification factor. All values larger than 1 have been marked red and all values lower than 1 have been marked green because non-isolating behaviour is unacceptable. The optimal damping ratio is located around 25 %, as was also shown in figure 1.12. However, using such low spring constants and damping ratios will have an enormous effect on the maximum compression. As will be shown next.

The second table shows the maximum compression for differing spring constants and damping ratios. All values for the maximum compression lower than 0,2 m have been marked green and all values exceeding 0,2 m have been marked red. This is in agreement with the maximum compression of jockey seats models currently in use. In contrary to the first table, in this case a high spring stiffness is beneficial. To comply with the maximum compression requirement a spring stiffness of at least 16 kN is needed.

It is clear that there is no overlap in these tables for the selected boundary values. Therefore, it is theoretically not possible to design an isolating suspension complying with the boundary condition observed in existing design. This conclusion is of major importance. Not only for this research project but also for other research projects focussing on acquiring new commercial jockey seats.

Force-displacement behaviour

An effective way to isolate shocks is by designing a suspension with a constant force-displacement behaviour. Similar behaviour can be observed in composite crash elements used in aerospace industry. However, these elements can be used only once. Such characteristics might be realized through the use of preloaded, buckling structures or introducing a preload such that the suspension becomes less stiff with increasing deformation. For a jockey seat behaving this way, the suspension will have to be very stiff the first couple of centimetres after which the spring constant jumps to a much lower value. This limits the maximum compression and maximizes the energy absorbed by the spring. It is referred to as a dual degressive spring rate.

This behaviour and its effects will be further illustrated with an example. In figure 1.16 the force-displacement graph can be seen for an imaginary spring. This spring has a spring constant of 75000 kN/m for the first 1.5 cm. After overcoming this first displacement the spring constant jumps to only 100 kN/m.

When regarding the acceleration-time diagram in figure 1.17 it becomes very clear this spring isolates well. It lowers the acceleration by 80% when compared to the input pulse. However, since no damping has been introduced into the system the motion of the spring is perpetual.

The previous discussion made clear why the suspension does not perform as desired. In this section the mass-spring-damper model was used to describe the ideal characteristics the suspension should ideally have. While this does not state whether these characteristics are also practically achievable, it does give a better impression how to design a new suspension.

It is already stated that a low spring constant is needed for shock isolation. Furthermore, it was stated that for a very low linear spring constant the maximum compression will greatly exceed the limits. This can be explained by the fact that a lot of compression is needed to fully store the energy in the spring.

Thus, the main objectives in redesigning the resilient mount will be to significantly increase the maximum allowable compression and to produce a resilient mounting with a non-linear characteristic which offers a gradually decreasing stiffness.

Damping ratio (%) \ Spring constant (kN/m)	2	4	6	8	10	12	14	16	18	20	22	24	26	28	30
0	0.558	0.774	0.930	1.054	1.156	1.243	1.316	1.381	1.437	1.485	1.527	1.563	1.594	1.622	1.646
5	0.521	0.724	0.871	0.988	1.084	1.166	1.236	1.296	1.349	1.395	1.434	1.467	1.498	1.521	1.543
10	0.494	0.688	0.828	0.939	1.032	1.110	1.178	1.235	1.286	1.326	1.364	1.394	1.421	1.446	1.465
15	0.475	0.662	0.798	0.906	0.995	1.071	1.138	1.189	1.237	1.275	1.308	1.338	1.362	1.381	1.403
20	0.464	0.647	0.781	0.888	0.976	1.049	1.108	1.158	1.198	1.236	1.266	1.290	1.315	1.335	1.350
25	0.460	0.642	0.776	0.882	0.964	1.033	1.086	1.133	1.172	1.201	1.232	1.257	1.276	1.293	1.311
30	0.463	0.648	0.782	0.880	0.959	1.019	1.072	1.113	1.149	1.180	1.204	1.225	1.246	1.263	1.277
35	0.475	0.663	0.789	0.883	0.955	1.013	1.058	1.099	1.132	1.157	1.183	1.204	1.221	1.234	1.247
40	0.495	0.677	0.798	0.886	0.954	1.007	1.052	1.087	1.117	1.144	1.165	1.182	1.198	1.213	1.226
45	0.515	0.693	0.807	0.891	0.954	1.005	1.044	1.078	1.107	1.130	1.148	1.167	1.182	1.195	1.205
50	0.534	0.706	0.818	0.896	0.957	1.002	1.041	1.072	1.097	1.118	1.138	1.154	1.167	1.176	1.186
55	0.553	0.722	0.826	0.902	0.957	1.002	1.038	1.065	1.089	1.111	1.128	1.141	1.151	1.163	1.173
60	0.570	0.735	0.837	0.907	0.961	1.003	1.034	1.061	1.085	1.103	1.117	1.129	1.142	1.153	1.161
65	0.587	0.747	0.846	0.913	0.964	1.001	1.033	1.059	1.079	1.094	1.109	1.122	1.133	1.142	1.148
70	0.604	0.761	0.853	0.920	0.966	1.002	1.033	1.055	1.072	1.089	1.104	1.115	1.124	1.131	1.136
75	0.619	0.773	0.863	0.925	0.968	1.004	1.031	1.051	1.070	1.085	1.098	1.108	1.115	1.121	1.129
80	0.634	0.784	0.872	0.929	0.973	1.005	1.029	1.050	1.067	1.081	1.092	1.100	1.107	1.115	1.122
85	0.648	0.794	0.879	0.934	0.976	1.005	1.028	1.049	1.065	1.076	1.085	1.094	1.102	1.109	1.115
90	0.662	0.805	0.885	0.940	0.978	1.005	1.029	1.048	1.061	1.071	1.081	1.090	1.098	1.104	1.108
95	0.675	0.815	0.892	0.945	0.979	1.007	1.029	1.046	1.058	1.068	1.078	1.086	1.093	1.098	1.101
100	0.688	0.824	0.899	0.949	0.982	1.009	1.029	1.043	1.054	1.066	1.075	1.082	1.088	1.092	1.095

Table 1.1: Isolation factor for varying spring constants and damping ratios

Damping ratio (%) \ Spring constant (kN/m)	12	14	16	18	20	22	24	26	28	30	32	34	36	38	40	42	44	46	48	50
0	0.631	0.574	0.527	0.486	0.453	0.423	0.397	0.374	0.353	0.335	0.318	0.301	0.288	0.275	0.262	0.251	0.242	0.232	0.223	0.214
5	0.587	0.533	0.489	0.451	0.420	0.393	0.369	0.347	0.328	0.311	0.294	0.280	0.267	0.255	0.243	0.234	0.224	0.216	0.207	0.199
10	0.547	0.496	0.456	0.421	0.392	0.366	0.344	0.323	0.306	0.289	0.274	0.262	0.249	0.238	0.227	0.218	0.209	0.201	0.193	0.186
15	0.512	0.465	0.426	0.395	0.366	0.343	0.321	0.303	0.286	0.271	0.257	0.245	0.233	0.222	0.213	0.204	0.196	0.188	0.181	0.175
20	0.481	0.437	0.400	0.370	0.344	0.322	0.301	0.285	0.269	0.254	0.242	0.230	0.219	0.209	0.200	0.192	0.185	0.177	0.170	0.164
25	0.453	0.411	0.377	0.349	0.325	0.303	0.284	0.268	0.253	0.239	0.228	0.217	0.207	0.197	0.189	0.181	0.174	0.167	0.161	0.155
30	0.427	0.388	0.357	0.329	0.307	0.286	0.269	0.253	0.239	0.226	0.215	0.205	0.195	0.187	0.179	0.172	0.165	0.158	0.152	0.147
35	0.405	0.367	0.338	0.312	0.290	0.271	0.255	0.240	0.226	0.215	0.204	0.194	0.185	0.177	0.170	0.163	0.156	0.150	0.145	0.140
40	0.385	0.349	0.320	0.296	0.276	0.257	0.242	0.228	0.215	0.204	0.194	0.185	0.176	0.169	0.162	0.155	0.149	0.143	0.138	0.133
45	0.366	0.332	0.305	0.282	0.262	0.245	0.230	0.217	0.205	0.194	0.185	0.176	0.168	0.161	0.154	0.148	0.142	0.137	0.132	0.127
50	0.349	0.317	0.290	0.269	0.250	0.234	0.220	0.207	0.195	0.186	0.177	0.168	0.160	0.154	0.147	0.142	0.136	0.131	0.126	0.122
55	0.333	0.303	0.278	0.257	0.239	0.223	0.210	0.198	0.187	0.178	0.169	0.161	0.153	0.147	0.141	0.136	0.130	0.125	0.121	0.117
60	0.318	0.290	0.266	0.246	0.228	0.214	0.201	0.189	0.179	0.170	0.162	0.154	0.147	0.141	0.136	0.130	0.125	0.121	0.116	0.112
65	0.305	0.278	0.255	0.236	0.219	0.205	0.193	0.182	0.172	0.163	0.155	0.148	0.141	0.136	0.130	0.125	0.121	0.116	0.112	0.108
70	0.293	0.266	0.245	0.226	0.210	0.197	0.185	0.174	0.165	0.157	0.150	0.143	0.136	0.131	0.126	0.121	0.116	0.112	0.108	0.104
75	0.282	0.256	0.235	0.217	0.202	0.190	0.178	0.168	0.159	0.151	0.144	0.137	0.131	0.126	0.121	0.117	0.112	0.108	0.104	0.101
80	0.271	0.246	0.227	0.209	0.195	0.183	0.172	0.162	0.154	0.146	0.139	0.133	0.127	0.122	0.117	0.113	0.108	0.105	0.101	0.098
85	0.262	0.238	0.218	0.202	0.188	0.176	0.166	0.156	0.148	0.141	0.134	0.128	0.123	0.118	0.113	0.109	0.105	0.101	0.098	0.095
90	0.252	0.229	0.211	0.195	0.182	0.170	0.160	0.151	0.143	0.136	0.130	0.124	0.119	0.114	0.110	0.106	0.102	0.098	0.095	0.092
95	0.244	0.222	0.204	0.188	0.176	0.165	0.155	0.146	0.139	0.132	0.126	0.120	0.115	0.110	0.106	0.102	0.099	0.095	0.092	0.089
100	0.236	0.214	0.197	0.182	0.170	0.159	0.150	0.141	0.134	0.128	0.122	0.117	0.112	0.107	0.103	0.099	0.096	0.093	0.090	0.087

Table 1.2: Maximum compression for varying spring constants and damping ratios

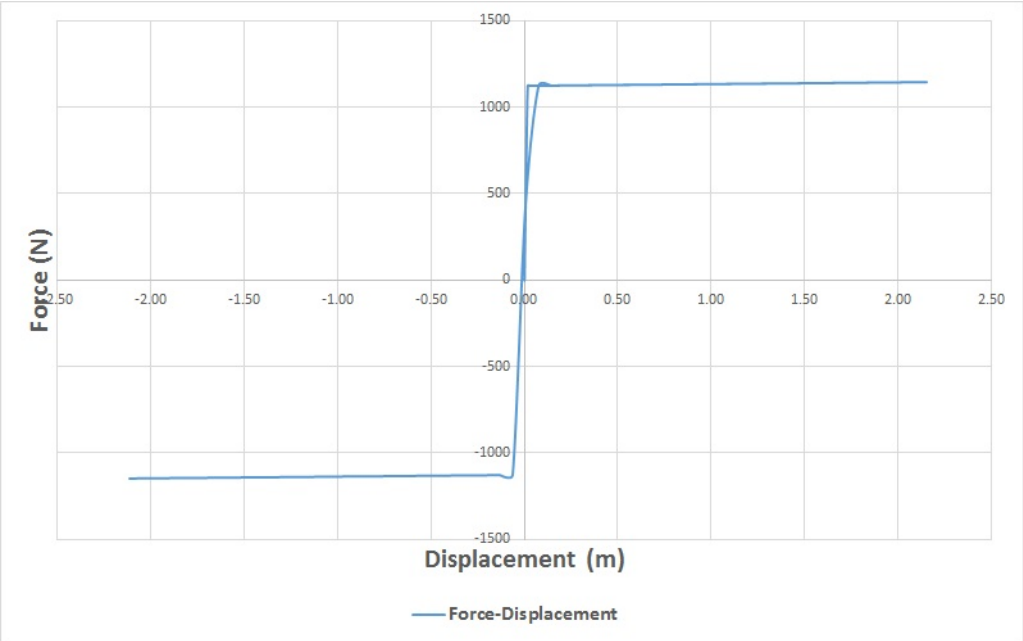

Figure 1.16: Force-displacement diagram for imaginary spring

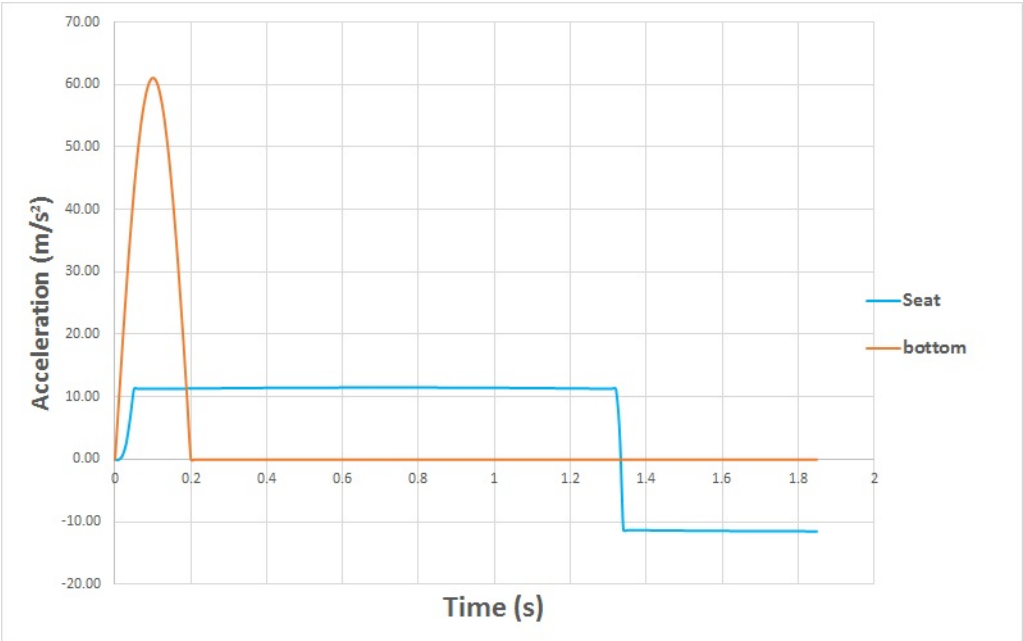

Figure 1.17: Accelaration-time diagram for input pulse and imaginary spring

Chapter 2

Currently used suspension designs

2.1 Introduction

Prior research into this subject mainly concerns the automotive industry. In the automotive industry, suspension exists in all kinds of forms and shapes. Traditionally the springs for these suspensions have been made from steel. More recently composites have been introduced in this area of engineering, opening up new design possibilities. Leaf springs, elliptical or semi-elliptical and coil springs are the most used designs. After the introduction of composites, the mono-leaf spring and wave spring are also more and more used.

Many designs are possible for seat suspension. In this chapter several spring designs will be presented. These designs are either found in literature or suggested by TNO. After presenting the designs, their advantages and disadvantages will be explained. Factors that influence the choice of design are cost, production, experience, geometry, materials, characteristics and Technology Readiness Level (TRL). Following this trade-off a first geometry design of the selected options will be discussed. In the next chapter this geometry will be further analysed and improved.

2.2 Leaf spring design

The leaf spring is one of the oldest spring designs available. It dates back to the Middle Ages. The first reference in academic context stems from 1938 in the form of a conference paper by M. Aitken [16]. An example of a steel leaf spring as used in the automotive industry can be seen in figure 2.1 [3].

Traditional leaf springs, like the one featured in figure 2.1, can have a linear spring rate or a progressive spring rate depending on the setup. Its working principle is based on bending. A progressive spring rate is realised through the use of several leaves stacked on top of each other in several layers, with progressively shorter leaves. In the process of deformation one by one the leaves make contact thus increasing the spring rate. An example of three typical load displacement characteristics can be seen in figure 2.2 [4]. The degressive spring rate is not applicable for leaf springs.

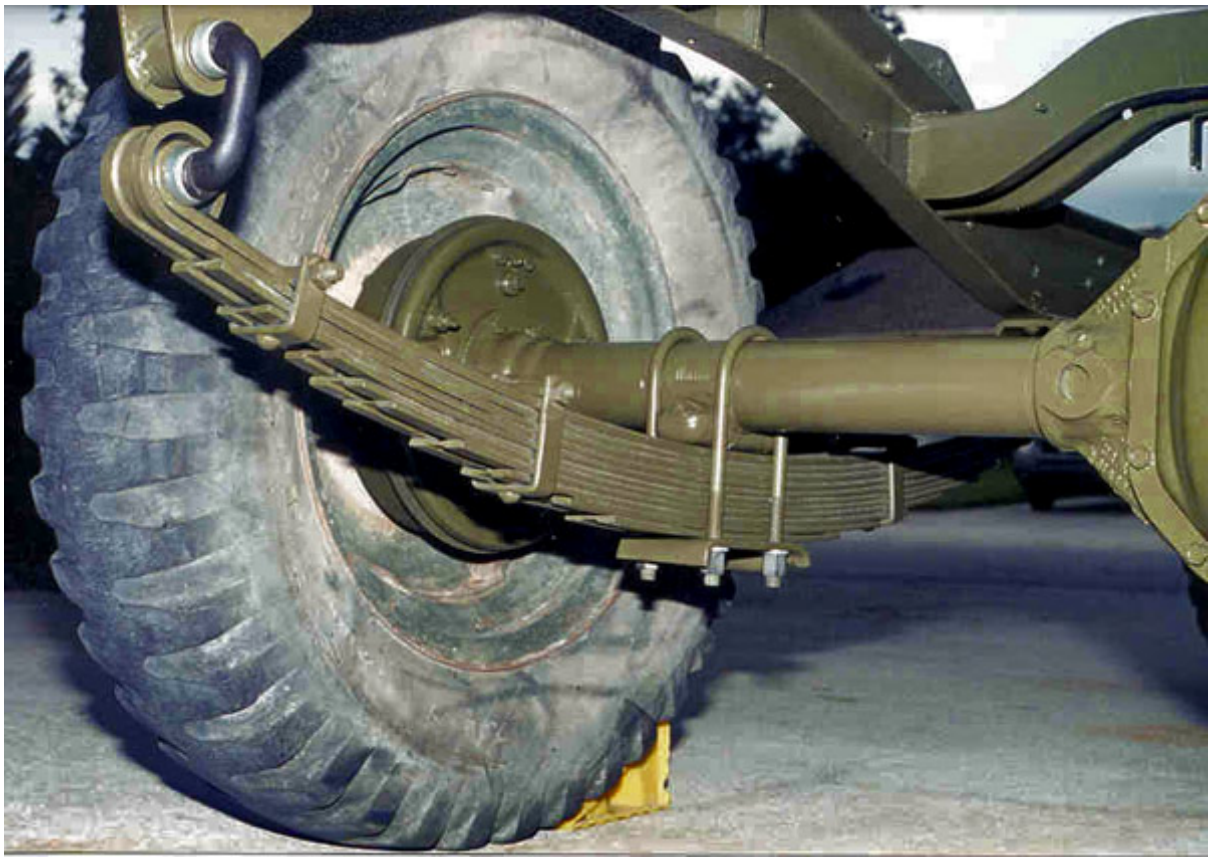

Figure 2.1: An example of a steel leaf spring [3]

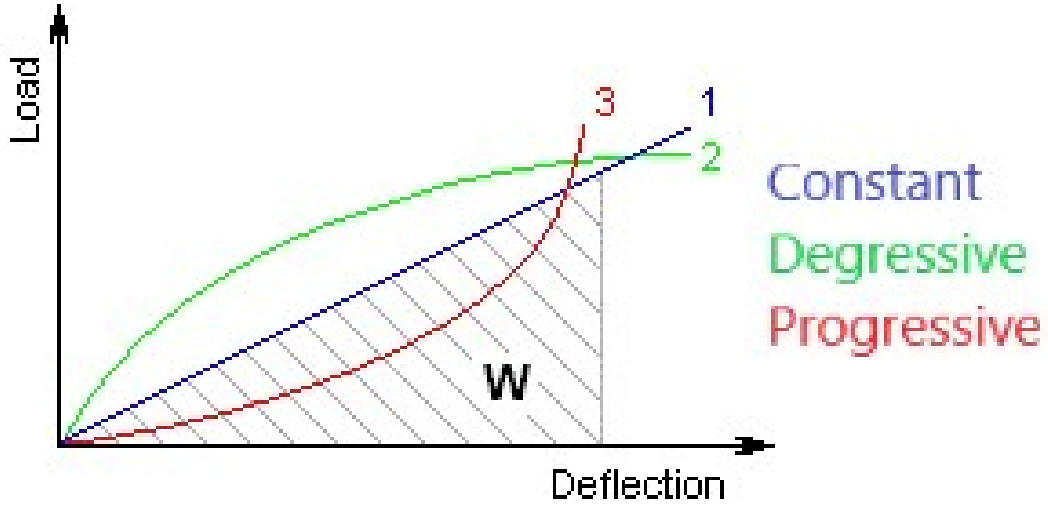

Figure 2.2: Several load-displacement characteristics [4]

Figure 2.3: Commercial CLS jockey seat [5]

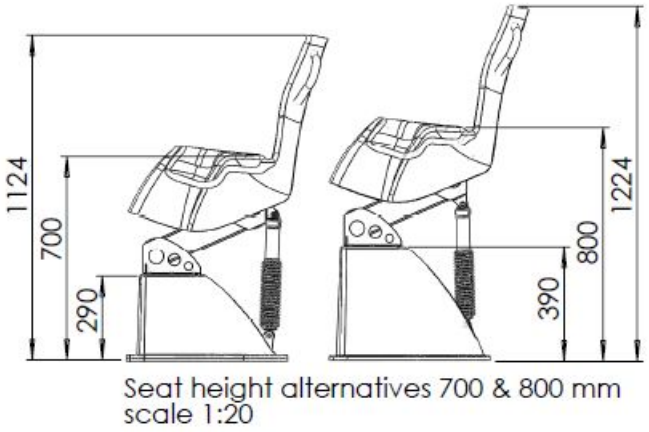

Figure 2.4: Detailed sketch of CLS seat - part 1

Research into the properties of composite leaf springs started after 1980 and is still ongoing. Worth mentioning for this project is for example the research of dynamic behaviour of CFRP (carbon fibre reinforced polymer) leaf springs by Krall and Zemann in 2014 and the research of Shokrieh and Rezaei into geometry optimization of composite leaf springs [17, 18].

Other research projects on composite leaf springs have been done by Rajesh et al. in 2015 for example. In that project conventional steel leaf springs were replaced by composite leaf springs. These were also tested for dynamic behaviour and low frequency impact loading [19]. Loganathan investigated the flexural response and cylic loading parameters for CFRP composites [20, 21].

Not only the performance of the leaf springs but also other boundary conditions, like joint strength have been researched. Among these are the influence of reinforced fibre length and their fatigue behaviour for low and high cycle loading and the performance of bearing surface with different bolt sizes [22, 23].

The idea of leaf spring design in the form of multiple bending elements is also used as a suspension in several commercially available jockey seats. An example of a seat design which incorporates this working principle can be seen in figure 2.3 which will be referred to as Composite Leaf Spring (CLS) jockey seat [5]. The CLS seat uses two resilient panels, clamped on both ends. Unlike automotive leaf spring designs these panels are not stacked on top of each other and damping is not depending on friction between the panels. The panels are separated and damping is achieved by a separate damper. This is a standard piston damping device.

A clear advantage of this design is the simple geometry. The resilient panels, made from composite, can be produced relatively easy compared to other designs. The dampers are being used in numerous applications, like the automotive and motor industry, and therefore readily available commercially in many sizes and designs. A more detailed sketch of this jockey seat can be seen in figures 2.4 and 2.5.

Designs based on leaf spring technology benefit from existing experience and availability in everyday life of this technology. Together with a straight-forward geometry and material this leads to relativly low costs and a high TRL. A detailed definition of the TRL levels can be found in the appendix in table B.1.

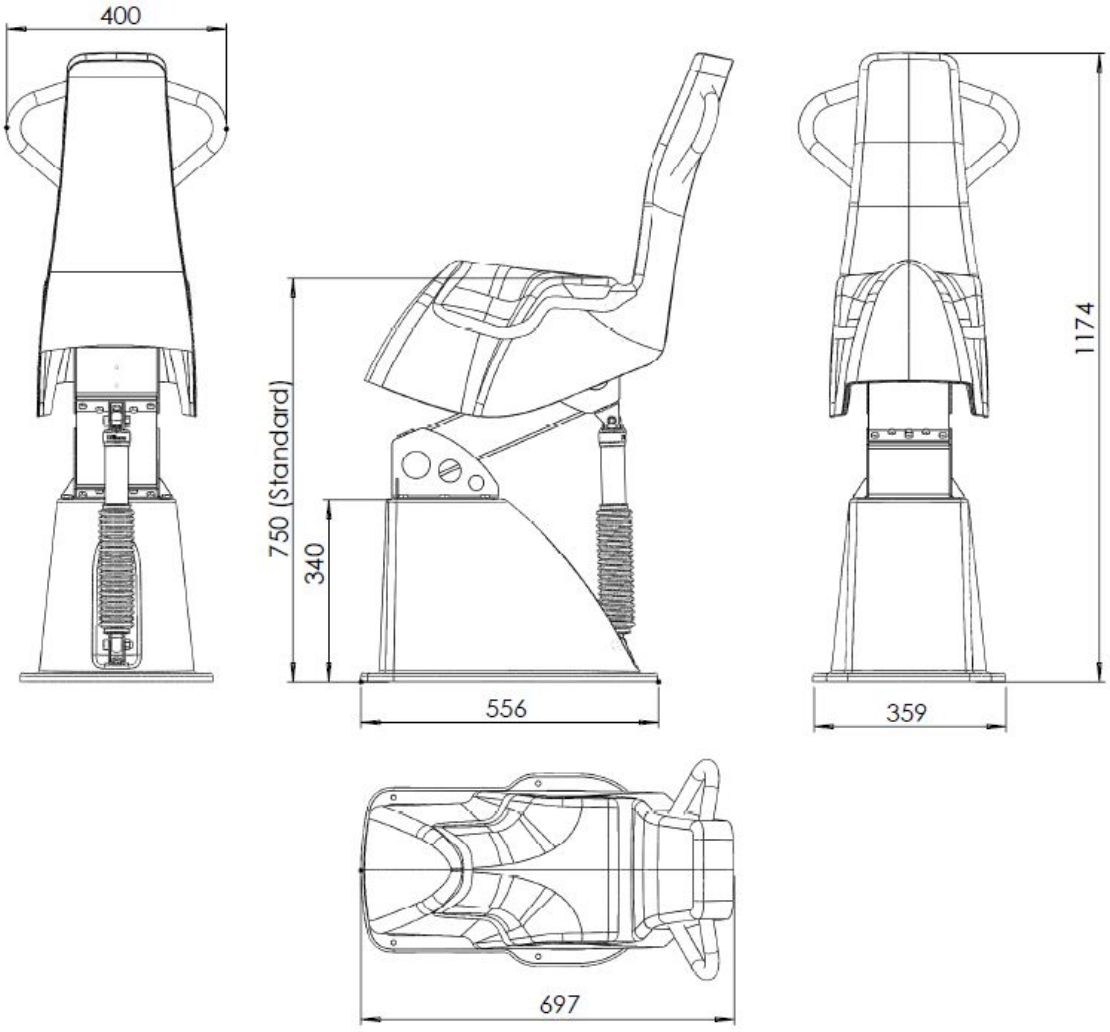

Figure 2.5: Detailed sketch of CLS jockey seat - part 2

Figure 2.6: Example of a coil and wave spring [6]

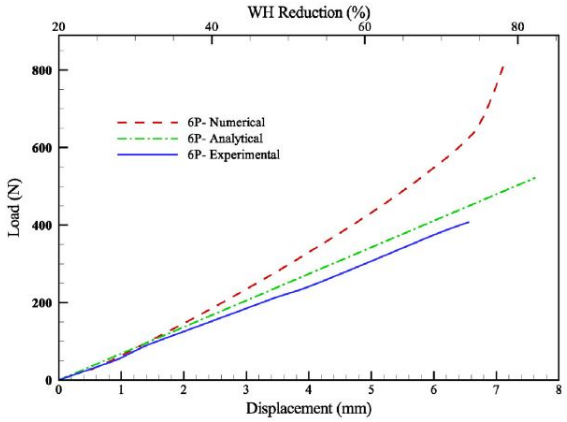

Figure 2.7: Load versus deflection curves for a 6 ply composite wave spring [6]

2.3 Wave spring design

The composite wave spring design is based on the steel coil spring design. With the same resiliency, the wave spring weighs less and occupies less space. This makes the wave spring very suitable for integration in small systems where space is limited. An example of both springs can be found in figure 2.6 [6].

Design and analysis of the failure modes for the classic steel coil spring has been performed by Prawoto et al [24]. Design, modelling and structural analysis of composite wave springs have been researched by Pavani et al. In his research paper it is stated that wave springs can reduce the size of an assembly up to 50%, reducing raw weight and material cost. A three dimensional finite element model was used for structural analysis. By changing the material used in the model Pavani tries to compare results and advise in the process of material selection [25].

In 2016, Erfanian-Naziftoosi et al. also researched the theory and design of wave springs. Like Prawato they also mention a 50% space saving compared to conventional alternatives. Besides this, they studied the mechanical behaviour and fatigue response reporting with numerical models and physical experiments reporting excellent properties compared to the steel alternatives [26]. An example of the load-displacement behaviour for these springs can be seen in figure 2.7 [6].

Despite the interesting characteristics mentioned earlier these springs are probably not suitable for the large displacements needed by the FRISC seats. These springs only provide for small displacements and when fully compressed still take up about 50% of their original size.

2.4 Elliptic shaped spring design

The working principle of the elliptic spring design is similar to that of the leaf spring. Both are based on bending. However, in elliptic springs the panels are curved to save space, for example. Three research papers on this topic in the automotive industry have been found [27–29]. More interesting is the fact that this design has already been used by TNO for other applications. An example of this design can be seen in figure 2.8.

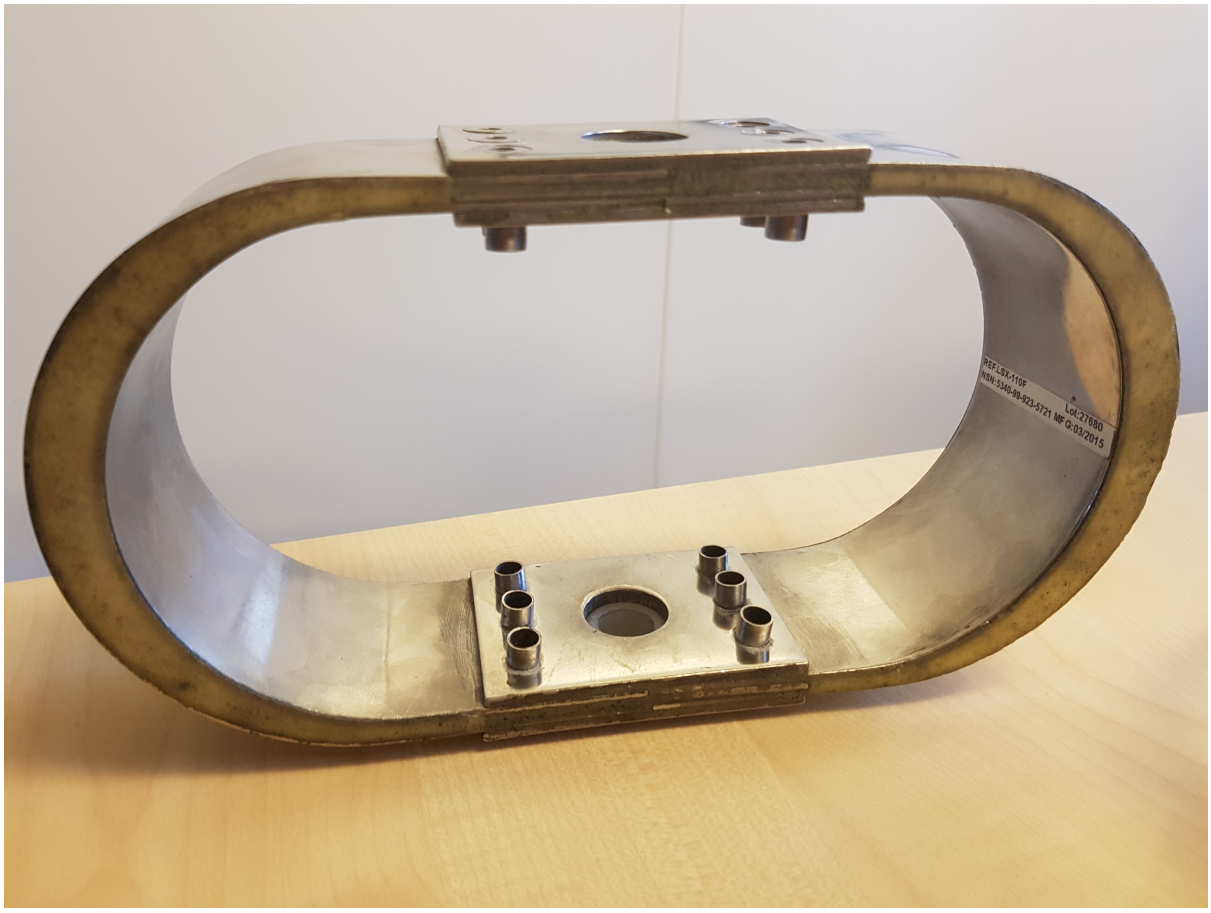

Figure 2.8: Example of a steel/polymer elliptic spring design

This design, made of steel with a polymer in between, has been produced by TNO and is used for shock absorbing applications in the maritime sector. Although this is a high frequency application, it is interesting to at least consider the geometry of this design. Previously obtained knowledge about this design could be useful in designing a composite elliptic spring. Furthermore, the geometry offers relatively much space for spring travel.

2.5 Negative Stiffness Honeycombs

In chapter 1, a force displacement graph for a imaginary spring has been presented in figure 1.16. A spring with these characteristics displays the best behaviour. Remains the question whether such a spring can be designed and manufactured. An example of an unconventional design with just these characteristics has been designed by the university of Texas [7]. However, this specimen only serves as a proof of concept and implementation in commercial applications has not yet been observed. Thus, this technology has a low TRL and a lot of research and funds are still needed before large scale production can be realised. Their ability to deform is also limited to about 50% of the original size, much like the wave spring desing presented before. An example of a negative stiffness honeycomb can be seen in figure 2.9.

The spring has a relatively large stiffness with its initial displacement. After which certain parts of the construction undergo controlled snap-through which in turn cause a negative stiffness. An example of the load-displacement curve for this design can be seen in figure 2.10.

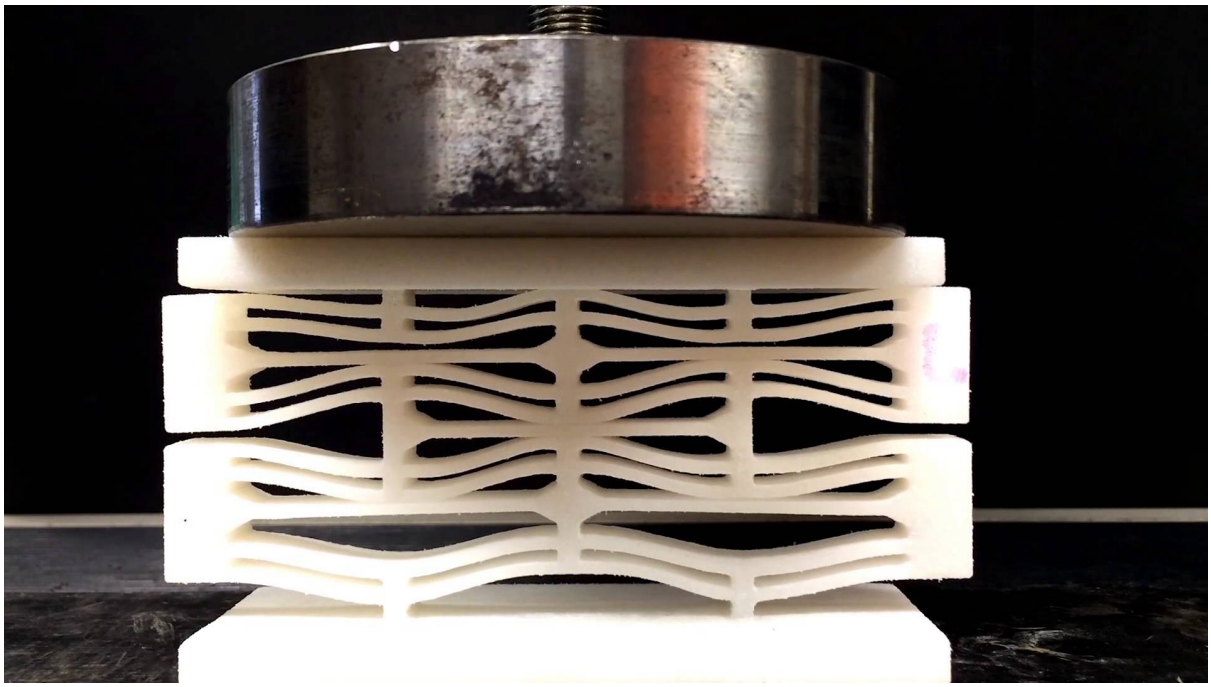

Figure 2.9: Negative stiffness honeycomb design by University of Texas [7]

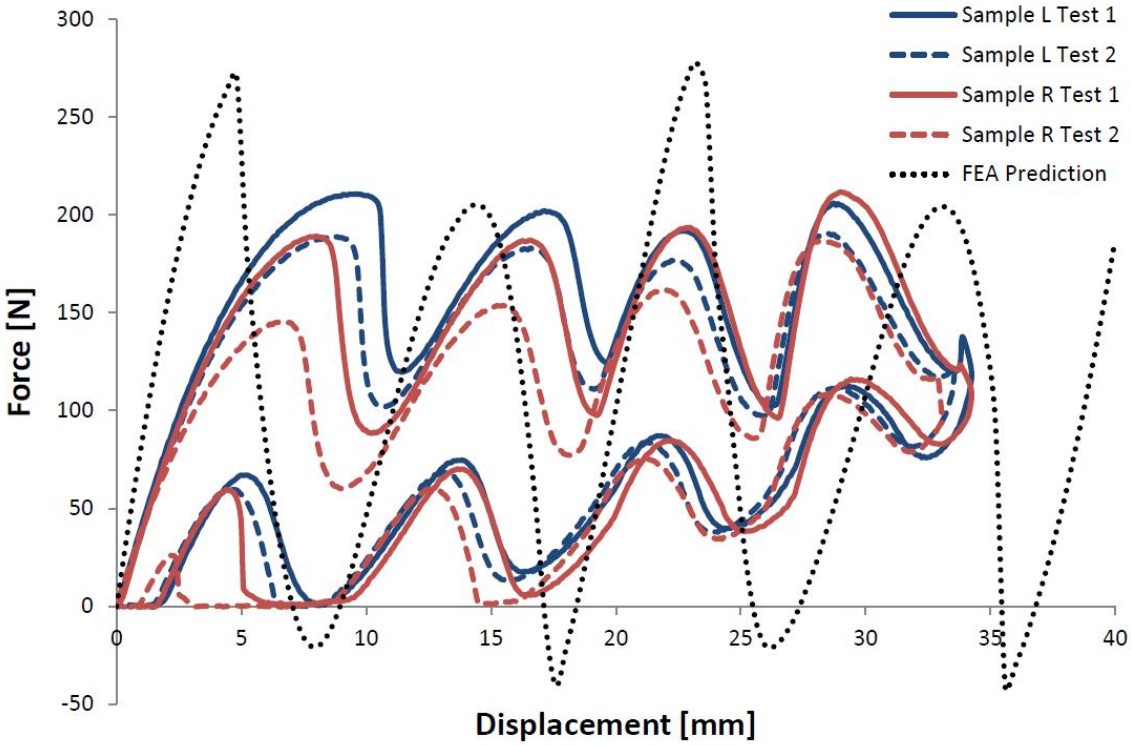

Figure 2.10: Force-displacement characteristic for honeycomb design [7]

2.6 Damping device for spring designs

In addition to the several spring designs presented earlier, the design of a simple damper is elaborated on in this section. In theory, anything that dissipates the energy in the resilient mounting can be called a damping device or damper. However, in practice almost all dampers are simple pistons converting energy into heat. In this section these dampers will therefore be further explained. In a basic oil damper design the following basic elements are present:

- The damper body, which holds the other components and fluid.
- The oil, which acts as the damping medium and dissipates the heat generated by friction.
- Piston, which contains oil flow ports and moves through the oil.
- Seal head, which closes the damper and keeps the oil inside the damper.
- Damper shaft, which is used to couple the system to the damper body.

These elements can also be seen in figure 2.11

Figure 2.11: Example of a standard fluid damper

2.7 Integration of damping properties

While most systems use independent damping solutions, effort is being made to optimise composites for damping characteristics. Several research project have focused on material selection for damping in composites. Examples being Lakes, Chung and Asworth et al. [30–32]. Ashworth focusses on special jute-carbon RTM (Resin Transfer Moulding) composites and Chung uses a viscoelastic layer to increase damping properties [33].

Although a sandwich panel theoretically is also an option, the literature found was not extensive. One research project was found about optimization of sandwich panels with a viscoelastic core for weight, material cost and modal damping [34]. A sandwich panel will deform more compared to a single composite panel with the same bending stiffness because of shearing of the core. However the viscoelastic core might be able to replace the damper.

	Cost	Production	Experience	Geometry	Materials	Characteristic	TRL
Leafspring	++	++	++	+	+	-	9
Coilspring	+	+	++	-	0	-	9
Wave spring	-	- -	-	o	+	-	7
Elliptic spring	+	+	+	+	+	+	8
Honeycomb	- -	0	–	-	0	++	4

Table 2.1: Trade-off existing spring designs

2.8 Spring design trade-off

Several directions of design, all with their pros and cons, have been presented so far. In this section a trade-off will be made helping to choose a feasible direction of design to pursue. Many factors can be considered when comparing the designs. They can be found in table 2.1. Six design options have been compared. The factors taken into account are cost, production, experience, geometry, materials, design characteristics and Technology Readiness Level (TRL).

Cost & Production

Leaf springs and coils springs are not expensive compared to the other three alternatives. Mass-produced models for the automotive industry can be found online for less than €100. Customized models will obviously cost more. Elliptic shaped springs are expected to be in the same order of magnitude. This spring has a lot in common with the leaf spring even though the geometry differs. The wave spring and honeycomb designs are the most expensive to produce. This is due to their more complicated geometry, low TRL and production process. 3D printing is used to produce the honeycomb design. This technique is gaining popularity quickly but still relatively new [35]. Cost and production are strongly linked; a long and complicated production process results in an expensive part. Only for the honeycomb design a large difference in cost and production is noted. The costs of this technique are still high, but the process of printing itself is rather straightforward and the printer only has to be as large as the part one wants to produce.

Experience

It was already stated that a lot of springs designs have already been used extensively in the automotive industry. This is further supported if one checks the amount of scientific papers published. For example, "coil spring" gives over 200.000 publications, while only 7.000 publications are found for "wave spring" on *http://scholar.google.com*. Increased experience with a certain design not only lowers costs for production, but also in maintenance. Continued development generally leads to designs that are less prone to failure and extensive knowledge on technology upkeep.

Geometry

When it comes to geometry it is important to select a design direction that allows for large displacements. Coil springs, wave springs and the honeycomb design can generally not compress to less than 50% of their original length. Clever designed wave and elliptic shaped springs could

allow for larger displacements. Secondly, the complexity of the geometry has been compared. The novel designs tend to lose this comparison. For example, the design mentioned in figure 2.9 shows a great amount of complexity. An other factor of importance is the ability to apply pre-tension to the design. To apply pre-tension to a design one has to impose a deflection under zero-load. The spring will only start to compress after this pre-tension has been overcome. This might be beneficial for the spring characteristic and will be researched in more detail later.

Materials

Most designs allow for steel or composite to be used depending on the application. Special filaments are needed for 3D printing. These usually consist of thermoplastics like polylactide, acrylonitril-butadieen-styreen (ABS) or polyethyleentereftalaatglycol (PETG).

Characteristic

In 1 the ideal deflection-load curve was described for a shock isolating spring. This characteristic is difficult to achieve with traditional spring which often have a linear or progressive spring rate. A well chosen geometry and application of pre-tension could result in a more degressive characteristic. The honeycomb design incorporates this through controlled buckling of local elements.

Technology Readiness Level

The TRL indicates the level of maturity of the technology described. Its use promotes consistent and uniform discussion when comparing different types of technology. An explanation of the Technology Readiness Levels can be found in table B.1.

2.9 Concluding remarks

There is clearly a strong link between all described factors. For example, the costs will greatly depend on the production techniques that are needed, the design geometry and the material used for the designs. Design with a more complicated geometry, take longer to accurately produce. This also shows that the total costs consists of more than raw material costs only. One would rather perform such a trade-off with independent variables. Even though that is not possible here the trade-off with these factor makes sense, because these are the most important factors in selecting a design directions identified together with TNO.

All in all, it seems that in order to produce a working prototype fulfilling all requirements, while staying within a reasonable budget and time schedule, results in a design that is either based on a leaf spring or elliptic spring design. This should be combined with a degressive spring rate and/or the application of a pre-tension. The coil spring technology is already used in the PCS jockey seat in which it does not perform as desired. The novel wave spring and negative stiffness honeycomb design, although looking promising, are not realistic design directions for this thesis due to time constraints

In the foregoing chapter the problem has been analysed and several existing designs have been presented, followed by a trade-off. Based on the this information, the available time and resources two design directions have been identified, which will be researched by analysing several variations.

First, these designs will be statically analysed with an analytical approach and FE-models. An important objective is to improve the force-displacement characteristics. To achieve this the maximum deflection of the design should be significantly larger than the existing designs discussed earlier.

Dynamic analysis will be performed with the use of MatLab. Using this program, a suitable model can be produced which accurately describes the dynamic behaviour and which allows comparison with the currently used design. Lastly, a testing environment is needed to test the prototype. Facilities of TNO were used to provide in this need.

Chapter 3

Static analysis of two designs

In this chapter static analysis for two selected designs is presented. In the first sections an improvement of the composite leaf spring design and a double leaf spring design are analysed analytically. The first design is similar to the commercial model presented earlier. However, with this analytical model it is possible to investigate variations of the design. The results were promising but its performance was not sufficient.

Following this analytical linear approach several FE-models will be presented. In these models the non-linear behaviour of the two designs is investigated to get a deeper understanding of the two design directions. Non-linear effects can be caused by geometrical non-linearity, material non-linearity and contact. These effects result in a stiffness matrix which is not constant during the load application. This is opposed to the linear static analysis, where the stiffness matrix remained constant. In this analysis the non-linearity is caused by large deflections (geometrical non-linearity). This geometric nonlinearity is due to large displacements of the structure.

3.1 Analytical analysis of composite leaf spring design

First an analytical approach will be derived to determine the displacement of the jockey seat with a composite leaf spring design. For this purpose the resilient parts are modelled as beams. An overview can be seen in figure 3.1:

At points A and B the construction is clamped and the beam BC is treated as an undeformable body. Furthermore, the model features a number of variables which are mentioned in table 3.1:

The constants E_b and E_m depend on the materials used and will be selected later. The load is applied at point L and the structure has six reactions at point A and D. As featured in figure 3.2:

Thus the equilibrium equations for the horizontal and vertical forces and moments are given by:

$$\begin{aligned} \Sigma \rightarrow \quad & -H_D - H_L - H_A = 0 \\ \Sigma \uparrow \quad & -V_D - V_L - V_A = 0 \\ \Sigma M \quad & -H_D \cdot h - M_D + H_L(a \cdot \sin(\alpha) - \frac{1}{2}h) - V_L \cdot a \cdot \cos(\alpha) - M_L - M_A = 0 \end{aligned} \tag{3.1}$$

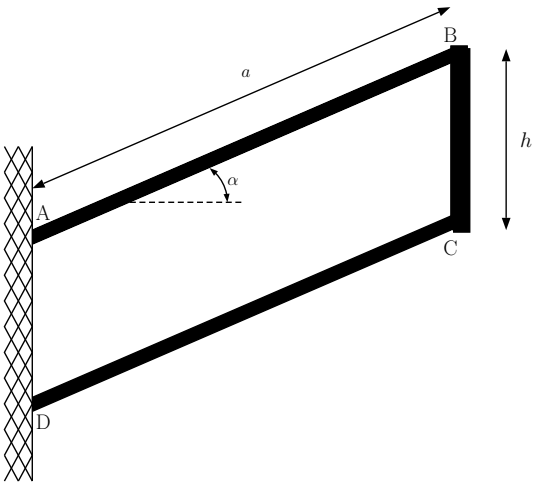

Figure 3.1: Representation used for analytical approach

Variable	Description
α	Angle with horizontal plane
h	Distance between resilient plates
a	Length of resilient plates
w	Width of resilient plates
t	Thickness of resilient plates
I	Moment of inertia
E_b	Young's modulus in bending
E_m	"in compression/tension

Table 3.1: Variables used in analytical approach

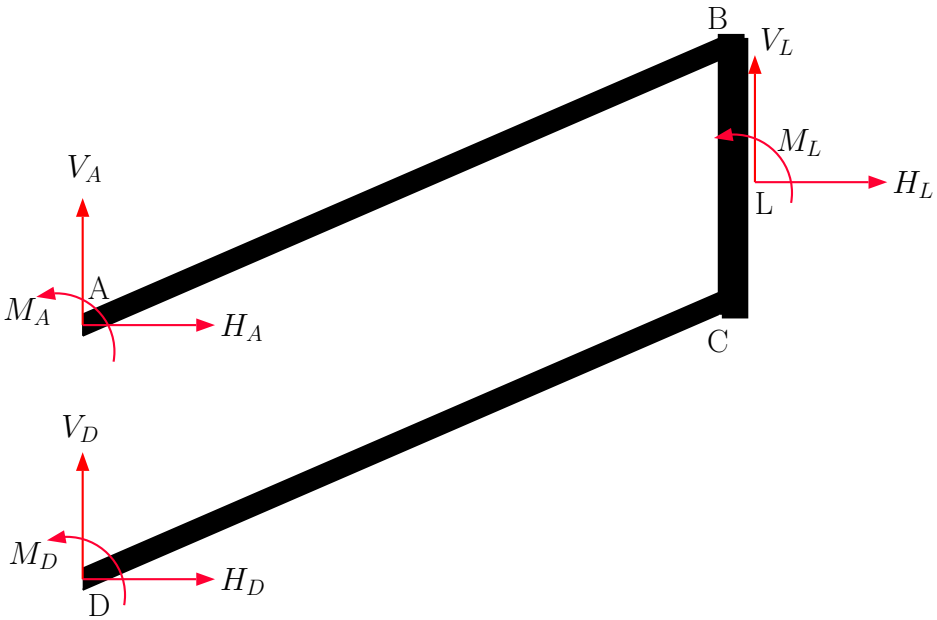

Figure 3.2: Free Body Diagram I

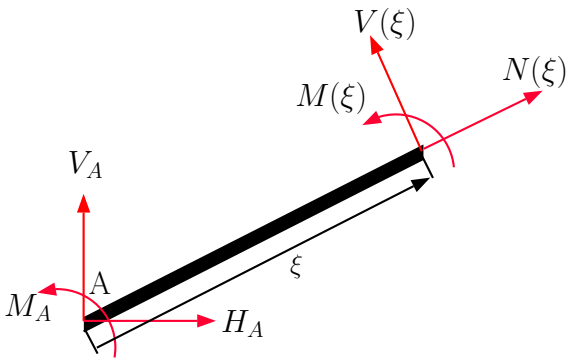

Figure 3.3: Free Body Diagram II

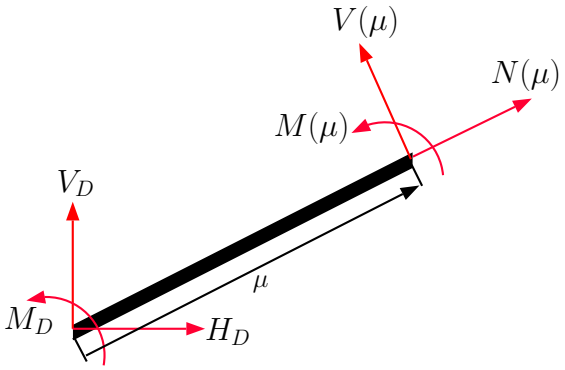

Figure 3.4: Free Body Diagram III

We have six unknown reactions and only three equilibrium equations. Therefore, this construction is statically indeterminate to the third degree. Point D is therefore substituted by forces H_D, V_D and moment M_D according to the Virtual Work method [36]. We continue with the equations for the first Free Body Diagram, which is shown in figure 3.3.

$$\begin{aligned} N(\xi) &= -H_A \cos(\alpha) - V_A \sin(\alpha) \\ V(\xi) &= H_A \sin(\alpha) - V_A \cdot \cos(\alpha) \\ M(\xi) &= -M_A + (V_A \cdot \cos(\alpha) - H_A \cdot \sin(\alpha)) \cdot \xi \end{aligned} \tag{3.2}$$

After substitution of H_A, V_A and M_A:

$$\begin{aligned} N(\xi) &= (H_D + H_L) \cdot \cos(\alpha) + (V_D + V_L) \cdot \sin(\alpha) \\ V(\xi) &= (-H_D - H_L) \sin(\alpha) - (-V_D - V_L) \cdot \cos(\alpha) \\ M(\xi) &= M_D + M_L + H_D \cdot h - H_L(a \cdot \sin(\alpha) - \frac{1}{2}h) + V_L \cdot a \cos(\alpha) \\ &\quad + ((-V_D - V_L) \cos(\alpha) - (-H_D - H_L) \sin(\alpha))\xi \end{aligned} \tag{3.3}$$

The second Free Body Diagram is shown in figure 3.4. Followed by the equations for the second free body diagram:

$$\begin{aligned} N(\mu) &= -H_D \cdot cos(\alpha) - V_D \cdot \sin(\alpha) \\ V(\mu) &= H_D \cdot \sin(\alpha) + V_D \cdot cos(\alpha) \\ M(\mu) &= -M_D + (V_D \cdot cos(\alpha) - H_D \cdot \sin(\alpha)) \cdot \mu \end{aligned} \tag{3.4}$$

Next, the displacements u_D, v_D and rotation ϕ_D are determined, after which these will be subjected to their boundary conditions.

First, we start with determining several derivatives which are needed:

$$\begin{aligned}
\overline{N}(\xi) &= \frac{\partial}{\partial H_D} N(\xi) && = cos(\alpha) \\
\overline{M}(\xi) &= \frac{\partial}{\partial H_D} M(\xi) && = h + \xi \cdot \sin(\alpha) \\
\overline{N}(\mu) &= \frac{\partial}{\partial H_D} N(\mu) && = -cos(\alpha) \\
\overline{M}(\mu) &= \frac{\partial}{\partial H_D} N(\mu) && = -\mu \cdot \sin(\alpha)
\end{aligned} \tag{3.5}$$

The displacement u_D is now given by:

$$u_D = \int_0^a \left(\frac{N(\xi)\overline{N}(\xi)}{E_m A} + \frac{M(\xi)\overline{M}(\xi)}{E_b I} \right) d\xi + \int_0^a \left(\frac{N(\mu)\overline{N}(\mu)}{E_m A} + \frac{M(\mu)\overline{M}(\mu)}{E_b I} \right) d\mu \tag{3.6}$$

Substituting and rearranging:

$$\begin{aligned}
u_D = & \underbrace{\left(\frac{\frac{2}{3}a^3 \sin^2(\alpha) + h \cdot a^2 \sin(\alpha) + h^2 \cdot a}{E_b I} + \frac{2acos^2(\alpha)}{E_m A} \right)}_{\mathbf{A11}} H_D \\
& + \underbrace{\left(\frac{-\frac{2}{3}a^3 cos(\alpha)\sin(\alpha) - \frac{1}{2}ha^2 cos(\alpha)}{E_b I} + \frac{2a\cos(\alpha)\sin(\alpha)}{E_m A} \right)}_{\text{A12}} V_D \\
& + \underbrace{\left(\frac{a^2 \sin(\alpha) + a \cdot h}{E_b I} \right)}_{\text{A13}} M_D \\
& + \underbrace{\left(\frac{-\frac{1}{6}a^3 \sin^2(\alpha) - \frac{1}{4}ha^2 \sin(\alpha) + \frac{1}{2}h^2 a}{E_b I} + \frac{acos^2(\alpha)}{E_m A} \right)}_{\text{B11}} H_L \\
& + \underbrace{\left(\frac{\frac{1}{6}a^3 \cos(\alpha)\sin(\alpha) + \frac{1}{2}ha^2 cos(\alpha)}{E_b I} + \frac{a\cos(\alpha)\sin(\alpha)}{E_m A} \right)}_{\text{B12}} V_L \\
& + \underbrace{\left(\frac{\frac{1}{2}a^2 \sin(\alpha) + ha}{E_b I} \right)}_{\text{B13}} M_L
\end{aligned} \tag{3.7}$$

The expressions for the horizontal displacement u_D can now be rewritten as:

$$u_D = A_{11}H_D + A_{12}V_D + A_{13}M_D + B_{11}H_L + B_{12}V_L + B_{13}M_L \tag{3.8}$$

The same procedure is used for the vertical displacement v_D.

Again we start with several derivatives, this time with respect to V_D:

$$\begin{aligned}
\overline{N}(\xi) &= \frac{\partial}{\partial V_D} N(\xi) &&= \cos(\alpha) \\
\overline{M}(\xi) &= \frac{\partial}{\partial V_D} M(\xi) &&= -\xi \cdot cos(\alpha) \\
\overline{N}(\mu) &= \frac{\partial}{\partial V_D} N(\mu) &&= -\cos(\alpha) \\
\overline{M}(\mu) &= \frac{\partial}{\partial V_D} N(\mu) &&= \mu \cdot cos(\alpha)
\end{aligned} \tag{3.9}$$

The displacement v_D is now given by:

$$v_D = \int_0^a \left(\frac{N(\xi)\overline{N}(\xi)}{E_m A} + \frac{M(\xi)\overline{M}(\xi)}{E_b I} \right) d\xi + \int_0^a \left(\frac{N(\mu)\overline{N}(\mu)}{E_m A} + \frac{M(\mu)\overline{M}(\mu)}{E_b I} \right) d\mu \tag{3.10}$$

Substituting and rearranging:

$$\begin{aligned}
v_D = & \underbrace{\left(\frac{-\frac{2}{3}a^3 cos(\alpha)\cos(\alpha) - \frac{1}{2}ha^2 cos(\alpha)}{E_b I} + \frac{2a cos(\alpha)\cos(\alpha)}{E_m A} \right)}_{\text{A21}} H_D \\
& + \underbrace{\left(\frac{\frac{2}{3}a^3 cos^2(\alpha)}{E_b I} + \frac{2a\cos^2(\alpha)}{E_m A} \right)}_{\text{A22}} V_D \\
& - \underbrace{\left(\frac{a^2 cos(\alpha)}{E_b I} \right)}_{\text{A23}} M_D \\
& + \underbrace{\left(\frac{\frac{1}{6}a^3 cos(\alpha)\cos(\alpha) - \frac{1}{4}ha^2 cos(\alpha)}{E_b I} + \frac{a cos(\alpha)\cos(\alpha)}{E_m A} \right)}_{\text{B21}} H_L \\
& + \underbrace{\left(\frac{-\frac{1}{6}a^3 cos^2(\alpha)}{E_b I} + \frac{a\cos^2(\alpha)}{E_m A} \right)}_{\text{B22}} V_L \\
& - \underbrace{\left(\frac{\frac{1}{2}a^2 cos(\alpha)}{E_b I} \right)}_{\text{B23}} M_L
\end{aligned} \tag{3.11}$$

The expressions for the vertical displacement v_D can now be written as:

$$v_D = A_{21}H_D + A_{22}V_D + A_{23}M_D + B_{21}H_L + B_{22}V_L + B_{23}M_L \tag{3.12}$$

Now ϕ_D is determined. For this we redetermine the derivatives with respect to M_D:

$$\begin{aligned}
\overline{N}(\xi) &= \frac{\partial}{\partial M_D} N(\xi) \quad &= 0 \\
\overline{M}(\xi) &= \frac{\partial}{\partial M_D} M(\xi) \quad &= 1 \\
\overline{N}(\mu) &= \frac{\partial}{\partial M_D} N(\mu) \quad &= 0 \\
\overline{M}(\mu) &= \frac{\partial}{\partial M_D} N(\mu) \quad &= -1
\end{aligned} \tag{3.13}$$

The rotation ϕ_D is now given by:

$$\phi_D = \int_0^a \left(\frac{N(\xi)\overline{N}(\xi)}{E_m A} + \frac{M(\xi)\overline{M}(\xi)}{E_b I} \right) d\xi + \int_0^a \left(\frac{N(\mu)\overline{N}(\mu)}{E_m A} + \frac{M(\mu)\overline{M}(\mu)}{E_b I} \right) d\mu \tag{3.14}$$

Substituting and rearranging:

$$\begin{aligned}
\phi_D = & \underbrace{\left(\frac{a^2 \cos(\alpha) + ha}{E_b I} \right)}_{\text{A31}} H_D \\
& + \underbrace{\left(\frac{a^2 cos(\alpha)}{E_b I} \right)}_{\text{A32}} V_D \\
& + \underbrace{\left(\frac{2a}{E_b I} \right)}_{\text{A33}} M_D \\
& + \underbrace{\left(\frac{-\frac{1}{2}a^2 \sin(\alpha) + \frac{1}{2}ah}{E_b I} \right)}_{\text{B31}} H_L \\
& + \underbrace{\left(\frac{\frac{1}{2}a^2 cos(\alpha)}{E_b I} \right)}_{\text{B32}} V_L \\
& + \underbrace{\left(\frac{a}{E_b I} \right)}_{\text{B33}} M_L
\end{aligned} \tag{3.15}$$

ϕ_D can now be rewritten as:

$$\phi_D = A_{31} H_D + A_{32} V_D + A_{33} M_D + B_{31} H_L + B_{32} V_L + B_{33} M_L \tag{3.16}$$

Now the boundary conditions are imposed resulting in:

$$\begin{bmatrix} A_{11} & A_{12} & A_{13} \\ A_{21} & A_{22} & A_{23} \\ A_{31} & A_{32} & A_{33} \end{bmatrix} \begin{pmatrix} H_D \\ V_D \\ M_D \end{pmatrix} + \begin{bmatrix} B_{11} & B_{12} & B_{13} \\ B_{21} & B_{22} & B_{23} \\ B_{31} & B_{32} & B_{33} \end{bmatrix} \begin{pmatrix} H_L \\ V_L \\ M_L \end{pmatrix} = \begin{pmatrix} u_D \\ v_D \\ \phi_D \end{pmatrix} = \begin{pmatrix} 0 \\ 0 \\ 0 \end{pmatrix} \tag{3.17}$$

Rearranging and introducing a substitution gives:

$$\begin{aligned}\begin{pmatrix} H_D \\ V_D \\ M_D \end{pmatrix} &= -\begin{bmatrix} A_{11} & A_{12} & A_{13} \\ A_{21} & A_{22} & A_{23} \\ A_{31} & A_{32} & A_{33} \end{bmatrix}^{-1} \begin{bmatrix} B_{11} & B_{12} & B_{13} \\ B_{21} & B_{22} & B_{23} \\ B_{31} & B_{32} & B_{33} \end{bmatrix} \begin{pmatrix} H_L \\ V_L \\ M_L \end{pmatrix} \\ &= \begin{bmatrix} C_{11} & C_{12} & C_{13} \\ C_{21} & C_{22} & C_{23} \\ C_{31} & C_{32} & C_{33} \end{bmatrix} \begin{pmatrix} H_L \\ V_L \\ M_L \end{pmatrix}\end{aligned} \tag{3.18}$$

Now the displacement and rotation of point D is fully described by constants and the applied load at point L. The C matrix can be used to describe the normal-forces N_ξ and N_μ and the moments M_ξ and M_μ as functions of H_L, V_L and M_L:

$$\begin{aligned} N(\xi) &= (C_{11}H_L + C_{12}V_L + C_{13}M_L)cos(\alpha) + (C_{21}H_L + C_{22}V_L + C_{23}M_L)\cos(\alpha) \\ &\quad + H_L cos(\alpha) + V_L \cos(\alpha) \\ M(\xi) &= (\xi\cos(\alpha) + h)(C_{11}H_L + C_{12}V_L + C_{13}M_L) \\ &\quad - \xi cos(\alpha)(C_{21}H_L + C_{22}V_L + C_{23}M_L) + (C_{31}H_L + C_{32}V_L + C_{33}M_L) \\ &\quad + (\xi\cos(\alpha) + \frac{1}{2}h - a\cos(\alpha))H_L + (acos(\alpha) - \xi cos(\alpha))V_L + M_L \\ N(\mu) &= -(C_{11}H_L + C_{12}V_L + C_{13}M_L)cos(\alpha) - (C_{21}H_L + C_{22}V_L + C_{23}M_L)\cos(\alpha) \\ M(\mu) &= -\mu\cos(\alpha)(C_{11}H_L + C_{12}V_L + C_{13}M_L) + \mu cos(\alpha)(C_{21}H_L + C_{22}V_L + C_{23}M_L) \\ &\quad - (C_{31}H_L + C_{32}V_L + C_{33}M_L) \end{aligned} \tag{3.19}$$

Finally, the vertical displacement, horizontal displacement and rotation of point L can be determined. For the vertical displacement several derivatives with respect to V_L are needed:

$$\begin{aligned} \overline{N}(\xi) &= \frac{\partial}{\partial V_L}N(\xi) = C_{12}cos(\alpha) + C_{22}\cos(\alpha) + \cos(\alpha) \\ \overline{M}(\xi) &= \frac{\partial}{\partial V_L}M(\xi) = C_{12}(\xi\cos(\alpha) + h) - C_{22}\xi cos(\alpha) + C_{32} + acos(\alpha) - \xi cos(\alpha) \\ \overline{N}(\mu) &= \frac{\partial}{\partial V_L}N(\mu) = -C_{12}cos(\alpha) - C_{22}\cos(\alpha) \\ \overline{M}(\mu) &= \frac{\partial}{\partial V_L}N(\mu) = -\mu C_{12}\cos(\alpha) + \mu C_{22}cos(\alpha) - C_{32} \end{aligned} \tag{3.20}$$

The displacement v_L is now described by:

$$v_L = \int_0^a \left(\frac{N(\xi)\overline{N}(\xi)}{E_m A} + \frac{M(\xi)\overline{M}(\xi)}{E_b I}\right)d\xi + \int_0^a \left(\frac{N(\mu)\overline{N}(\mu)}{E_m A} + \frac{M(\mu)\overline{M}(\mu)}{E_b I}\right)d\mu \tag{3.21}$$

In the same way the horizontal displacement u_L and rotation ϕ_L are derived:

$$\begin{aligned}
\overline{\overline{N}}(\xi) &= \frac{\partial}{\partial H_L} N(\xi) = C_{11} cos(\alpha) + C_{21} \cos(\alpha) + \cos(\alpha) \\
\overline{\overline{M}}(\xi) &= \frac{\partial}{\partial H_L} M(\xi) = C_{11}(\xi \cos(\alpha) + h) - C_{21} \xi cos(\alpha) + C_{31} \\
&\qquad - a cos(\alpha) + \xi cos(\alpha) + \frac{1}{2} h \\
\overline{\overline{N}}(\mu) &= \frac{\partial}{\partial H_L} N(\mu) = -C_{11} cos(\alpha) - C_{21} \cos(\alpha) \\
\overline{\overline{M}}(\mu) &= \frac{\partial}{\partial H_L} N(\mu) = -\mu C_{11} \cos(\alpha) + \mu C_{21} cos(\alpha) - C_{31}
\end{aligned} \tag{3.22}$$

$$\begin{aligned}
\overline{\overline{\overline{N}}}(\xi) &= \frac{\partial}{\partial M_L} N(\xi) = C_{13} cos(\alpha) + C_{23} \cos(\alpha) \\
\overline{\overline{\overline{M}}}(\xi) &= \frac{\partial}{\partial M_L} M(\xi) = C_{13}(\xi \cos(\alpha) + h) - C_{23} \xi cos(\alpha) + C_{33} + 1 \\
\overline{\overline{\overline{N}}}(\mu) &= \frac{\partial}{\partial M_L} N(\mu) = -C_{13} cos(\alpha) - C_{23} \cos(\alpha) \\
\overline{\overline{\overline{M}}}(\mu) &= \frac{\partial}{\partial M_L} N(\mu) = -\mu C_{13} \cos(\alpha) + \mu C_{23} cos(\alpha) - C_{33}
\end{aligned} \tag{3.23}$$

The horizontal displacement u_L and rotation ϕ_L are now described by:

$$u_L = \int_0^a \left(\frac{N(\xi)\overline{\overline{N}}(\xi)}{E_m A} + \frac{M(\xi)\overline{\overline{M}}(\xi)}{E_b I} \right) d\xi + \int_0^a \left(\frac{N(\mu)\overline{\overline{N}}(\mu)}{E_m A} + \frac{M(\mu)\overline{\overline{M}}(\mu)}{E_b I} \right) d\mu \tag{3.24}$$

$$\phi_L = \int_0^a \left(\frac{N(\xi)\overline{\overline{\overline{N}}}(\xi)}{E_m A} + \frac{M(\xi)\overline{\overline{\overline{M}}}(\xi)}{E_b I} \right) d\xi + \int_0^a \left(\frac{N(\mu)\overline{\overline{\overline{N}}}(\mu)}{E_m A} + \frac{M(\mu)\overline{\overline{\overline{M}}}(\mu)}{E_b I} \right) d\mu \tag{3.25}$$

This describes the displacement and rotation of point L and thus the displacement of the jockey seat. These equations can later be used to compare with the results of the FE-models as a validation.

3.2 Analytical analysis of c-shaped composite Leaf Spring Design

The second design that is analysed analytically is the design featured in figure 3.5. The construction previously discussed is doubled forming a c-shape. This increases the maximum compression for the construction significantly.

This time four resilient parts are used, which are designated as beams AB,CD,EF and GH in figure 3.5. The connecting parts AH and BC are modelled as rigid bodies and the construction is clamped at F and G. To determine the displacement the system is split up in three subsystems. Through superposition of these systems the final expression for the displacement of point L is obtained.

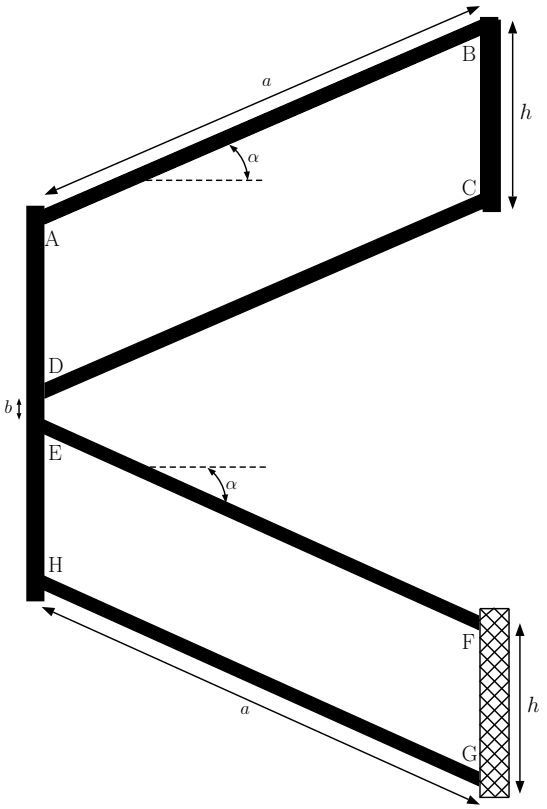

Figure 3.5: Representation used for analytical analysis

The full analytical derivation is given in detail in Appendix C, since the methods used in deriving the expressions for this design are quite similar compared to the previous one. In a similar way a system of equations is set up and solved. This gives an expression for the strain energy of the structure:

$$\begin{aligned} U = &\int_0^a \left(\frac{N(\xi)^2}{E_m A} + \frac{M(\xi)^2}{E_b I} \right) d\xi + \int_0^a \left(\frac{N(\mu)^2}{E_m A} + \frac{M(\mu)^2}{E_b I} \right) d\mu \\ &+ \int_0^a \left(\frac{N(\phi)^2}{E_m A} + \frac{M(\phi)^2}{E_b I} \right) d\phi + \int_0^a \left(\frac{N(\chi)^2}{E_m A} + \frac{M(\chi)^2}{E_b I} \right) d\chi \end{aligned} \tag{3.26}$$

Now the displacement and rotation of point L under influence of the loads H_L,V_L and M_L is given by:

$$\begin{aligned} u_L &= \frac{\partial U}{H_L} \\ v_L &= \frac{\partial U}{V_L} \\ \phi_L &= \frac{\partial U}{M_L} \end{aligned} \tag{3.27}$$

With these analytical expressions and the ones of section 3.1 the results of the linear and non-linear Finite Element models can be compared with the results of the expressions derived above. Furtermore, TNO can use them to quickly analyse a large amount of variations of this design. The FE models are described in the next sections.

Type		M10E/3783	
Density	ρ	1.90	g/cm^3
Longitudinal modulus	E_1	24.5	GPa
Transverse in-plane modulus	E_2	23.8	GPa
Transverse out-of-plane modulus	E_3	11.6	GPa
In-plane shear modulus	G_{12}	4.7	GPa
Out-of-plane shear modulus	G_{23}	3.6	GPa
Out-of-plane shear modulus	G_{13}	2.6	GPa
Major in-plane Poisson's ratio	v_{12}	0.11	-
Out-of-plane Poission's ratio	v_{23}	0.20	-
Out-of-plane Poission's ratio	v_{13}	0.15	-
Longitudinal tensile strength	F_{1t}	433	GPa
Transverse tensile strength	F_{2t}	386	GPa
In-plane shear strength	F_6	84	GPa
Longitudinal comp. strength	F_{1c}	377	GPa
Transverse comp. strength	F_{2c}	335	GPa

Table 3.2: Material constants for Epoxy/Glass fiber (E-glass) fabric

Ply number	Angle
1	(0/90)
2	(90/0)
3	(45/-45)
4	(-45/45)
5	(-45/45)
6	(45/-45)
7	(90/0)
8	(0/90)

Table 3.3: Lay-up FE-model

3.3 Finite Element analysis of composite leaf spring design

Materials

The starting point for the FE-models is the selection of the materials used. Considering the large deformations and relatively low spring stiffness that is required, a composite made of glass fibres and epoxy seems suitable as an initial choice of material. Should the material turn out to be insufficiënt in a later design phase, changes will be made accordingly and mentioned explicitly. The material properties of the composite that has been used in the analysis can be found in table 3.2. Values shown are applicable for a fibre volume ratio of 50%. Furthermore, the glass fibre is made into a fabric. The constants used have been extracted from *Engineering Mechanics of Composite Materials* by Daniel and Ishai [37].

At this point it is not known yet which materials will be available for the production of the prototype. If a different material is used the FE simulations will be repeated in agreement with the materials used.

Description of models

The leaf spring design of the chair as mentioned in figure 2.3 is used as an initial starting design for a FE-models. The model is made up of 2D conventional shell elements, S4R in Abaqus, suitable for large deformations, in our case up to 30 cm. In the shell model the composite layup is not represented by eight independent layers. Instead, an equivalent layer is calculated using the classical laminate theory simplifying further calculations and reducing calculation time. Furthermore, failure criteria, like Tsai-Hill and Tsai-Wu, can be implemented directly for each layer.

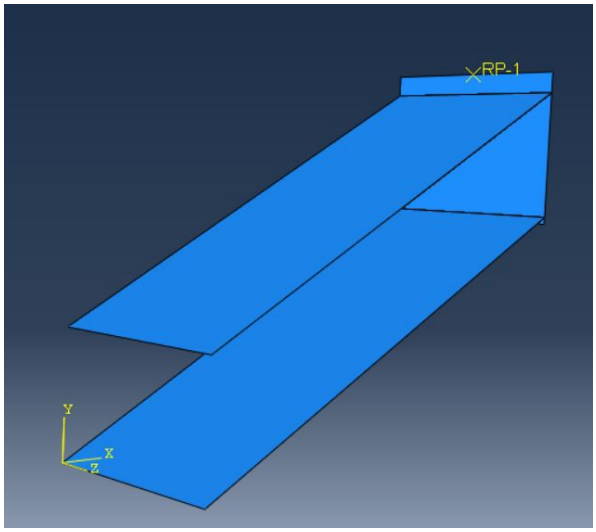

Figure 3.6: Ullman chair shell model

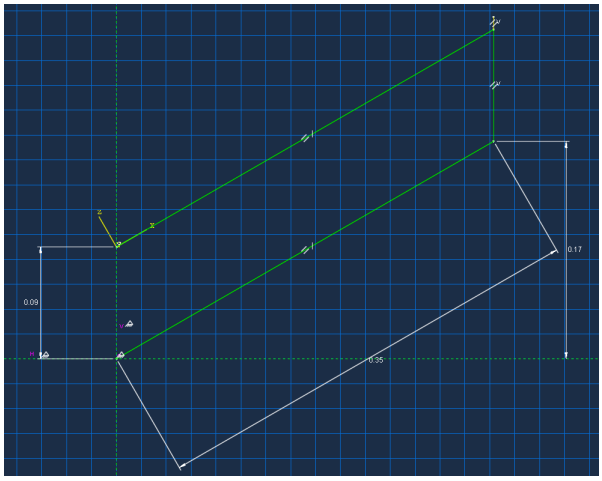

Figure 3.7: Dimensions Ullman chair

Alternatively, solid elements can be used in Abaqus. These are 3D brick shaped elements that represent the physical geometry exactly. Each composite ply is represented by an element, resulting in the use of eight elements through the thickness. Because all plies of the laminate are modelled, accurate results can be obtained. However, these elements are less suitable for large deflections and high aspect ratios. They should only be used when transverse shear effects are predominant, normal stresses cannot be ignored or when accurate inter-laminar stresses, such as near localized regions of complex loading or geometry, are required. Furthermore, calculation time needed for these elements is much larger than with conventional shell elements. For the models described below this would results in a processing time of minutes instead of seconds, which is still acceptable. For complex FE-models a processing time of hours or even days are not unusual.

The simplified FE-model can be seen in figures 3.6. The model resembles the design used in the analytical approach and features two composite plates and a block to the right. This block resembles the seat and its connection to the resilient parts. The block is considered as a rigid part in the model which keeps the plates equidistant. This means that the block itself cannot deform and all stresses and forces are transferred to the resilient parts. The block is connected to the composite parts through the use of a so-called tie constraint. A tie constraint partially or fully eliminates degrees of freedom of a group of nodes and couples their motion. On the lower left end the parts have been restricted with an encastre constraint. This means the nodes on the lower left part have no degrees of freedom. Both translational and rotational movement is set to zero.

The exact dimensions of the initial model can be seen in figure 3.7. These dimensions are in agreement with the existing jockey seat and are therefore chosen as a starting point. By choosing the same dimensions and type of material the results of the FE-model can be compared to the results of tests with the original seat. The analytical approach is used as an extra means of verification. The initial lay-up that has been used for the composite parts can be found in table 3.3. This is a realistic quasi-isotropic layup designed to withstand loading in various directions without suffering from warping. The zero degree layers have been placed on the outside for improved bending stiffness.

Results

To determine the characteristics of the spring a vertical force has been applied to the seat connection. Through use of the Arc-Length method [38] force-displacement graphs are produced which can be seen in figure 3.8. Unlike the Newton method, the Arc-Length method is still able to converge to a solution after a limit point is reached. It is suitable for systems that show unstable behaviour with either load and displacement control. In our case non-linear effects and instability can be expected, hence the use of the Arc-Length method.

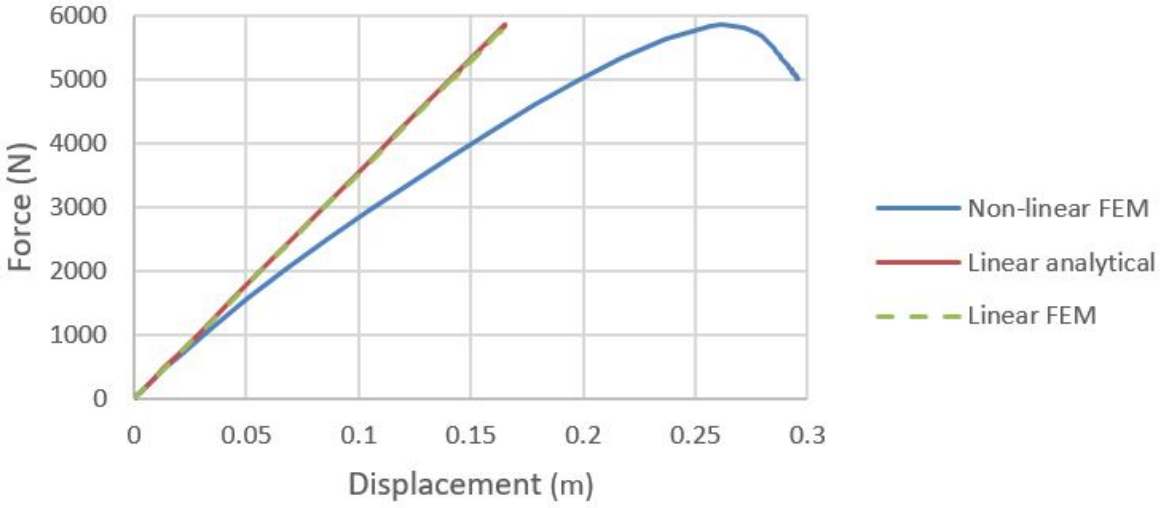

Figure 3.8: Force-displacement for M10E glass fibre fabric composite

A convergence check has been done to obtain the minimal amount of elements needed such that accurate results are obtained. In a convergence check the number of elements used in the FE-model is slowly increased to find an approximate number of elements at which the results more or less are in agreement with the previous step. The results can be seen in table 3.4 and figure 3.9. In this check the absolute vertical displacement has been used at a reference force of 5625 N. At 531 elements the results differ only 0.2% when compared to the displacement when 329 elements are used. The amount of elements was increased further to 769 with the same result. Processing time did not increase significantly and therefore 769 are used in this model and an increased proportional number will be used when the model size is increased in following FE-models.

# of elements	**Displacement**	**% difference**
9	0.2104	
25	0.1708	18.8
52	0.1743	2.0
199	0.1780	2.1
329	0.1773	0.4
531	0.1777	0.2
769	0.1780	0.2

Table 3.4: Convergence check results

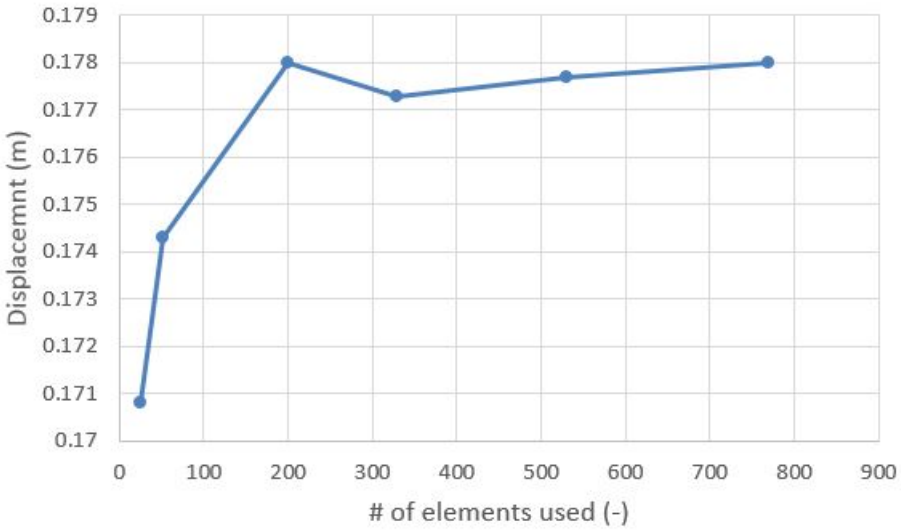

Figure 3.9: Convergence check at 5625N

The behaviour can be seen in figure 3.8. Through the use of the analytical linear approximation and the linear FE package the spring constants are 35.49 kN and 35.31 kN. Displacements are shown up to 30 cm. For a displacement of 15 cm the spring is near horizontal and the deformed shaped can be seen in figure 3.10. Displacements over 15 cm are deemed unrealistic for this design, because of bottoming of the damper.

Another point of interest are the stresses present in deformed state. Because the seat is loaded frequently, we need to make sure the load is well within the limits. If all plies have the same orientation the highest compressive and tensile stresses for bending are present in the first and last ply, because these are situated further from the centre. When plies are orientated differently relative to each other the first and last plies do not necessarily have to be the first ones to fail. The Tsai-Hill failure criterion provides a better insight into this behaviour. A graphical representation of the Tsai-Hill failure criterion for this GRP type is shown in figure 3.11 at a displacement of 10 cm. It should be noted that no correction for fatigue has been used in the evaluation of this criterion. It is advised to include fatigue testing of future prototypes.

As can be seen the stresses surpasses the material limits at displacements around 10 cm. This is not in agreement with experimental results for the CLS model described earlier. A few explanations are possible. As mentioned before the type of glass fibre used in the CLS seat is unknown. Therefore, it is possible that the stress limits for the CLS seat differ from those used in the model. An other explanation might be that the encastre constraint is too strict, for the real connection is bolted and some tolerance in the interface between clamp and composite plate can be expected. The need for real life testing of prototypes is endoresed by these results.

As mentioned before, several changes to the design can be made to increase the spring travel and change the spring stiffness. However, it seems implausible that these changes, e.g. increasing the length of the composite plates, will increase the spring travel to more than 30 cm without taking up to much space. Therefore, we will first review the elliptic design in the next section before experimenting with changes to this design.

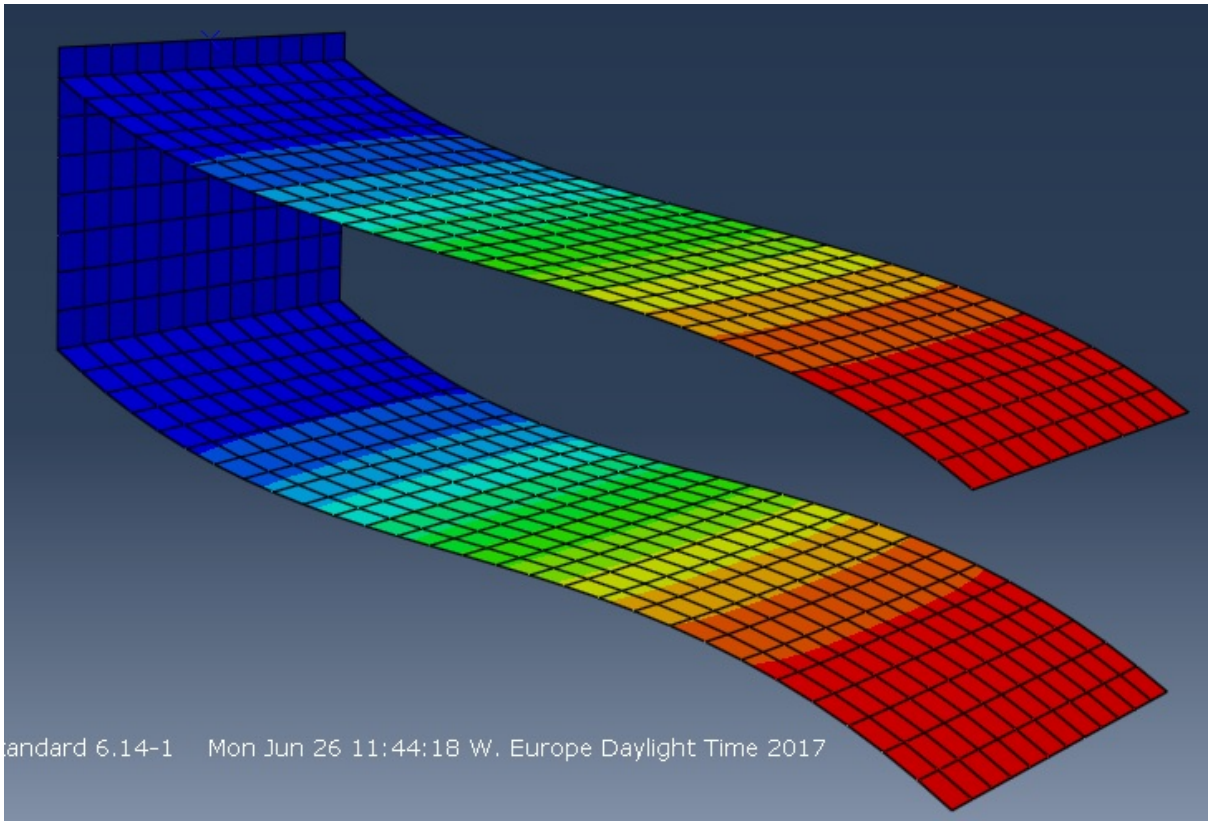

Figure 3.10: Example of deformed leaf spring design

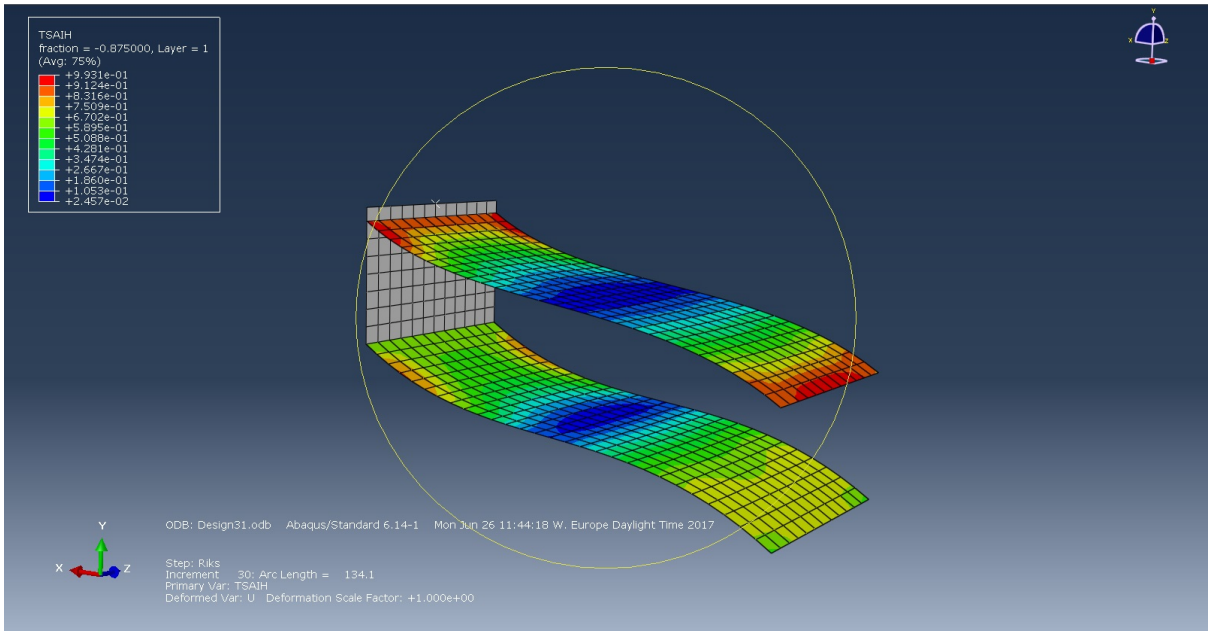

Figure 3.11: Tsai Hill criterion for u=10

3.4 Finite Element analysis of c-shaped composite leaf spring design

The second design shows a resilient c-shaped geometry. The first design is used as inspiration and the initial elliptic design is a doubled version of the first design. This results in a C-shape which allows more space for the spring to deform thus leading to an improved maximum compression. Expectations are this will lead to an increased maximum allowable compression between 20 and 25 cm, which should allow for a favourable force-displacement characteristic and thus better shock isolation as stated earlier.

Graphic impressions can be seen in figure 3.12 and 3.13, the design dimensions can be seen in figure 3.14. Furthermore, the composite lay-up has been changed to anticipate the drop in stiffness. The layup is mentioned in table 3.5. The force-displacement diagram for this design is shown in figure 3.15.

This design behaves different when compared to the first one. The stiffness decreased by about one third of the first design to 22.7 and 23.5 kN/m for the analytical and linear FE approach respectively and in the non-linear models a drop of about 25% is observed. The maximum allowable displacement according to Tsai-Hill criterion increased. A downside however, is the need for a connecting part that links the upper and lower resilient parts together. To lower the stress in the construction while keeping the displacement the same, it is important to further optimize the design. This will not only improve the results for the failure criterion, but also improve the shock mitigation behaviour. To do so we can change the lay-up of the material, the geometry of the design or do both. In the next chapter several of these options for optimizing this design will be inspected. This will again be done through adaptation of the FE-models.

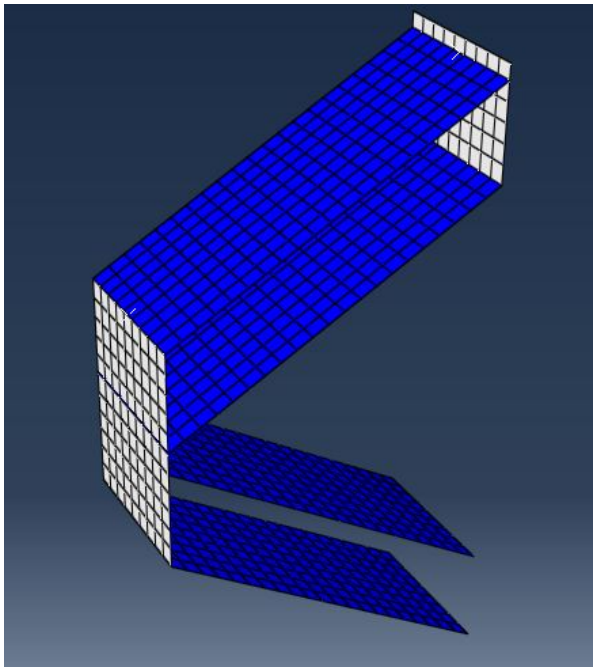

Figure 3.12: Example of elliptic shaped seat design

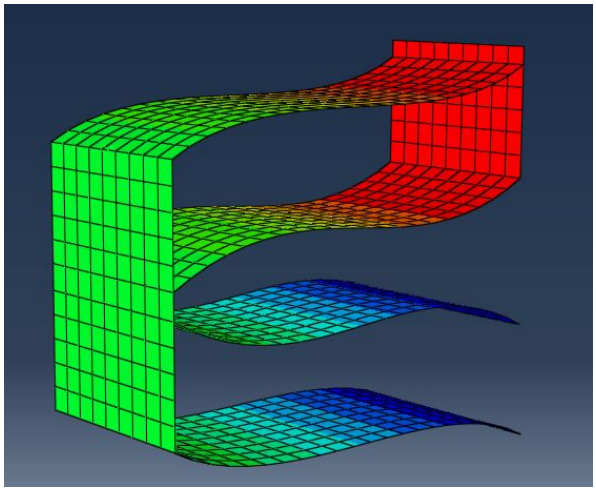

Figure 3.13: Example of deformed elliptic shaped seat design

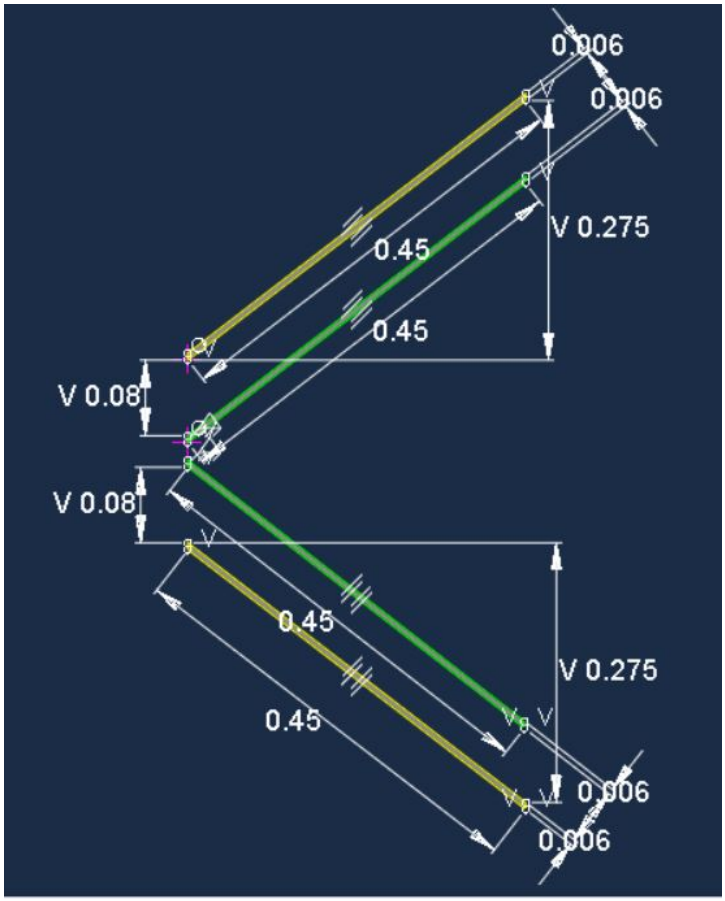

Figure 3.14: dimensions

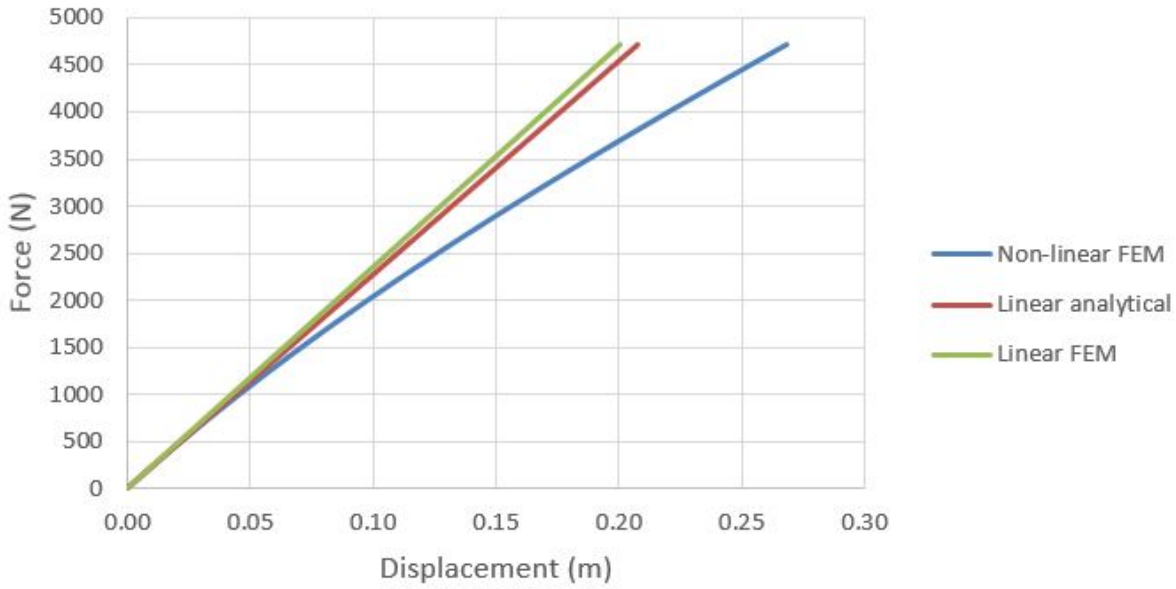

Figure 3.15: Force-displacement for M10E glass fibre fabric composite

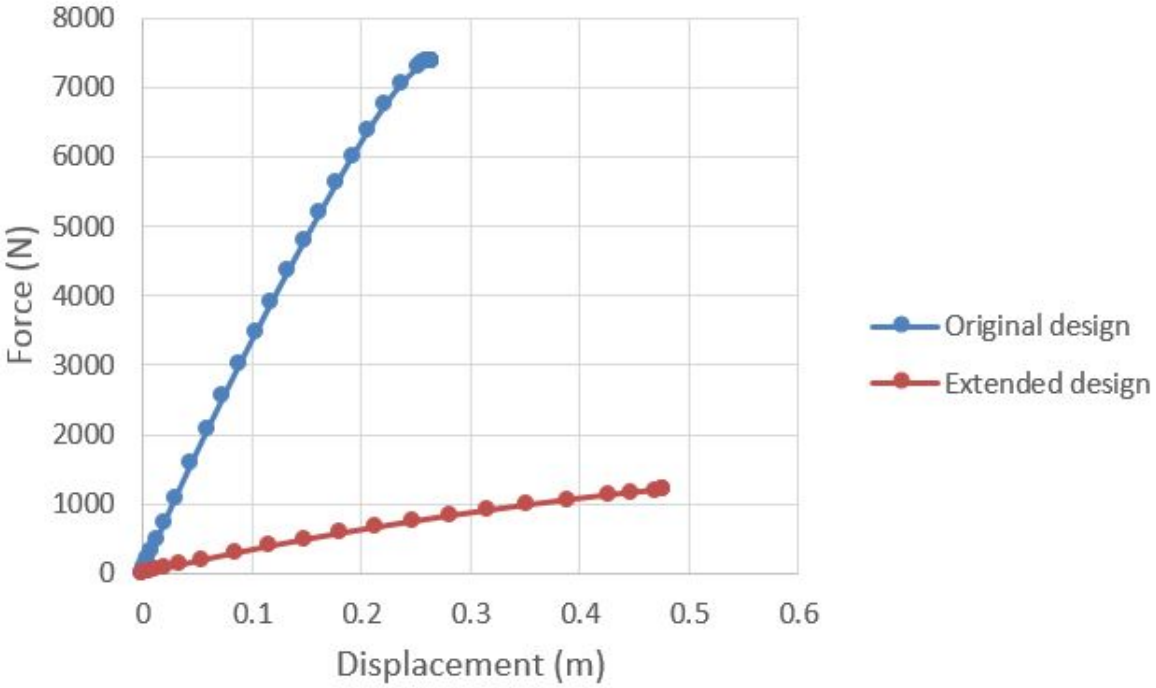

Figure 3.16: Force-displacement extended design

Ply number	Angle
1	(0/90)
2	(90/0)
3	(45/-45)
4	(-45/45)
5	(-45/45)
6	(45/-45)
7	(90/0)
8	(0/90)

Table 3.5: Lay-up used for elliptic design

3.5 Influence of variables on suspension performance

In this section we will shortly investigate the effect of changes on the initial design directions. For this purpose the FE-models are altered to accommodate the changes and the effects of the changes will be described.

Extending the design

In this variation the number of plies per plate remains the same but the length of each plate is increased. Measurements have been performed to determine the maximum space available on the FRISC. In the current design the seats are mounted on a pedestal. Without this pedestal more space is available and thus the maximum compression of the resilient mounting can be increased. Without the pedestal a horizontal space of 50 cm is available. Vertically, up to 100 cm is available, though attention is needed to realise a comfortable seat height for the occupants.

The effects of extending the design to its maximum are a huge drop in stiffness and an increase of the maximum displacement to well over 40 cm. This can be seen clearly in figure 3.16 where the force-displacment curves are shown for the original and extended design.

Variations of angle

It is also possible to influence the angle of the resilient mounting by changing the clamping and connection to the boat. These angle variations cause only small changes in the construction stiffness under vertical force. For example, to impose a displacement of $0.3m$ forces of respectively $869N$, $903N$ and $955N$ are needed for the plates with 31, 35 and 40 degrees inclination.These angles have been chosen such that differences can be observed without creating a design with unrealistic dimensions. Increasing the angle leads to an increase in stiffness. However, the changes tend to increase the compression force in the laminate thus making the construction more prone to buckling. This can also be seen in the FE results; the calculated displacement decreases as the angle increases because the simulation is stopped earlier due to instability of the construction. The results can be seen in figure 3.17

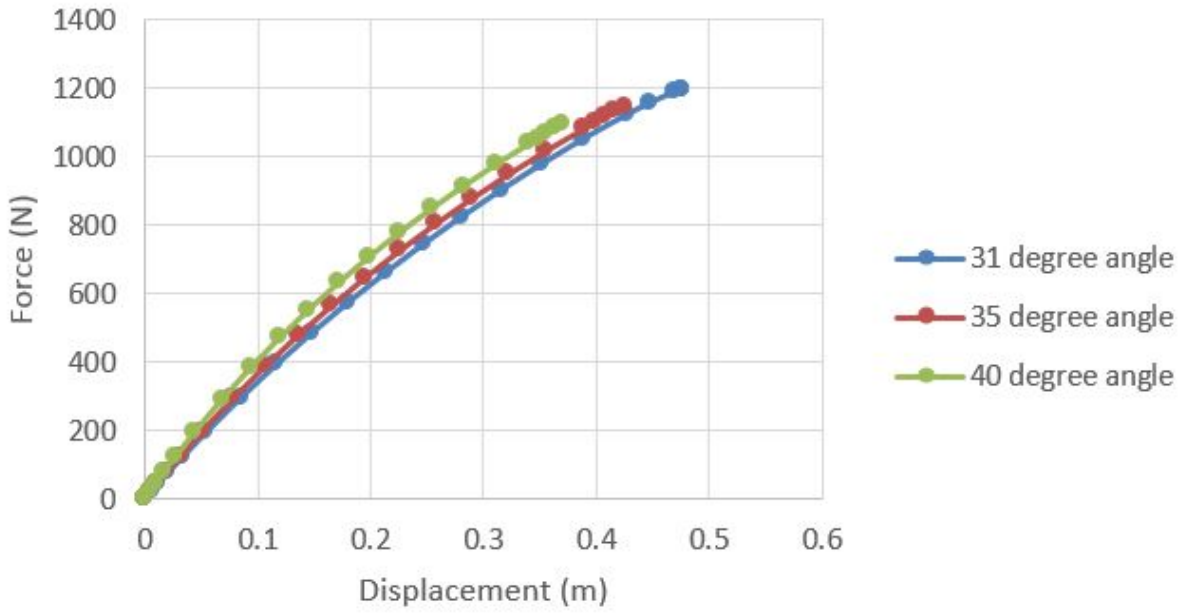

Figure 3.17: Force-displacement angle variation

Varying the distance between the plates

Another variable that can be influenced is the distance between the composite plates. Decreasing the distance between the plates has a large influence. It decreases the distance from neutral axis of the structure thus decreasing the bending stiffness. This in turn makes the structure buckle much earlier. It causes the design the destabilize at this point so that the FEM program has trouble converging. The FE-results can be seen in figure 3.18.

Varying the thickness, width and number of plates

Increasing the thickness of the resilient plates is achieved by increasing the amount of plies in the lay-up. As one can imagine, increasing the thickness will also increase the structural stiffness. This hypothesis is indeed confirmed by the FE-models. As can be seen in figure 3.19. In figure 3.19 the lay-up was increased from 8 to 16 plies. Varying the width of the plates will logically increase the stiffness of the construction. An overview of this effect can be seen in figure 3.20. Adding a third plate with the same lay-up and thus the same thickness also stiffens the design. As can be seen in figure 3.20 the effect of adding an extra plate in the middle has approximately the same effects as increasing the width of the two plates by 5 *cm*.

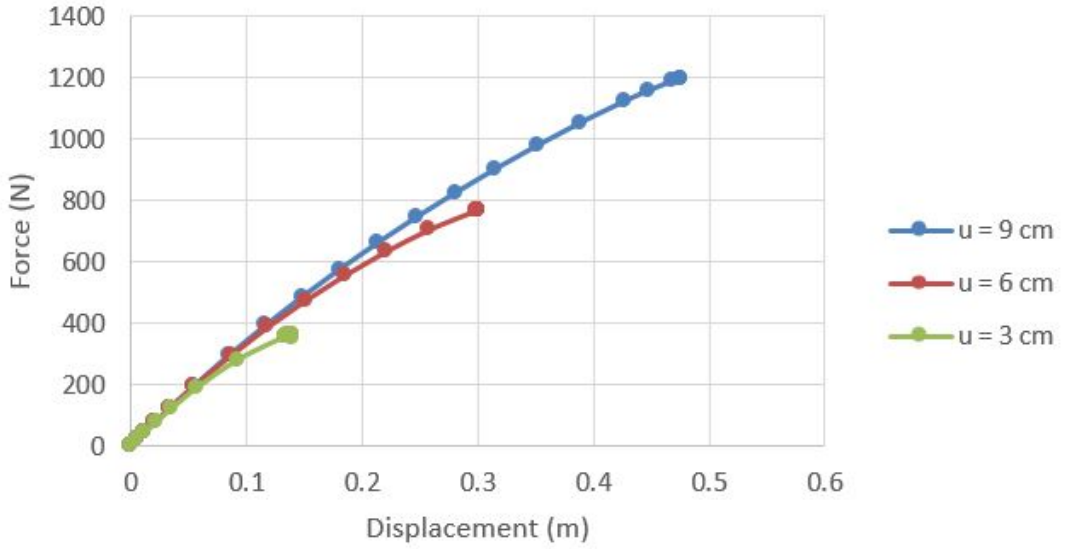

Figure 3.18: Force-displacement distance variation

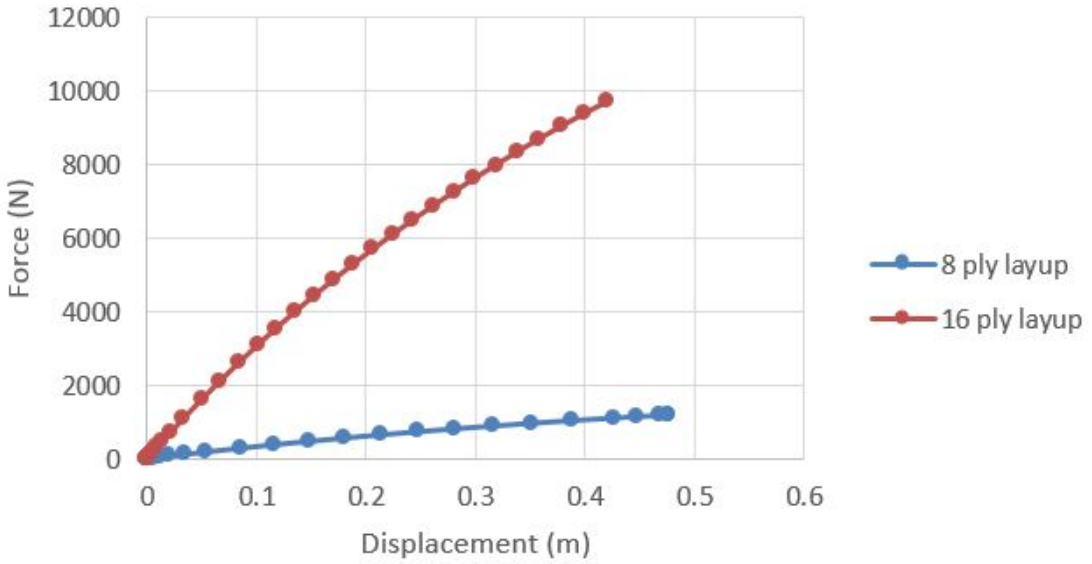

Figure 3.19: Force-displacement layup variations

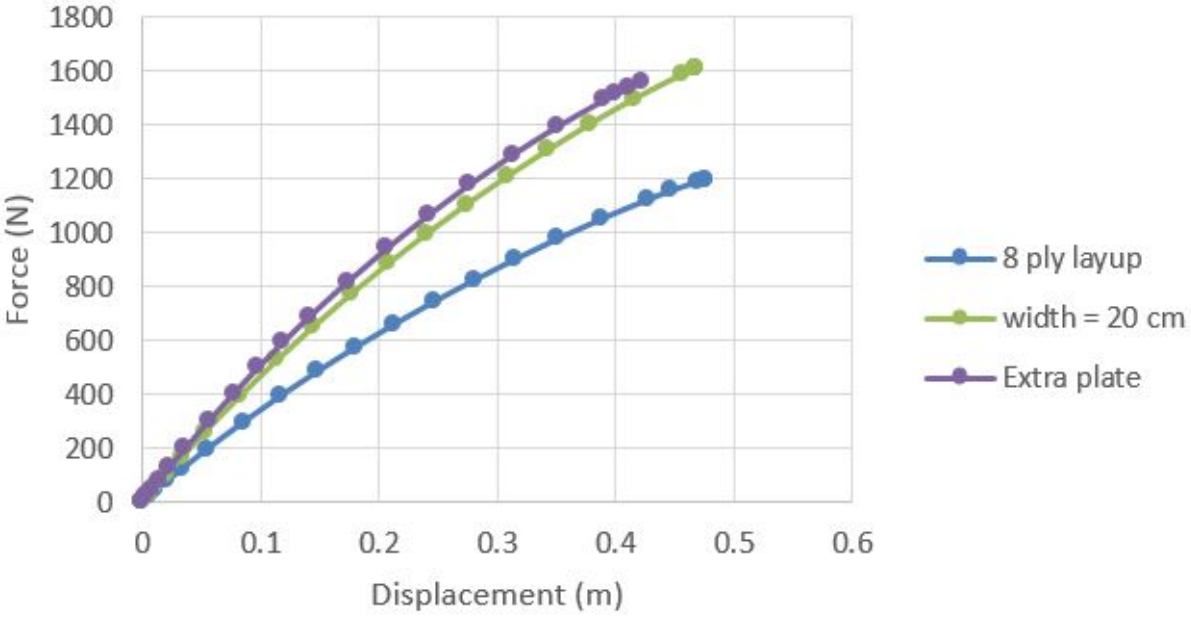

Figure 3.20: Force-displacement for design variations

Chapter 4

Prototype production

Previous chapters showed existing research, currently applied designs, innovations and the modelling and optimisation of the design. In this chapter the production of a first prototype will be discussed and presented. The main goal of this chapter is describe in detail the production of the prototype and its expected behaviour. For the prototype a thermoset composite will be produced. In total four plates will be fabricated which act as the resilient part of the seat. The seat itself and all other parts needed will be provided by TNO.

4.1 Material Characteristics

The plates are made of a thermoset composite. These composites contain polymers that crosslink together during curing thus forming an irreversible chemical bond. This makes the product less susceptible to the risk of remelting, thus making the composite more suitable for high-temperature applications. An other advantage is the production process which is quite fast and cost effective. Fabrication of the panel can be completed in half a day and after completion of the vacuum infusion the panels has to post-cure for a short duration in the oven.

It should be noted however that temperature needs to be kept below the Glass Transision Temperature (T_g) during in service use. At this temperature the epoxy undergoes a transformation from a relatively hard and brittle state to a more rubbery state. Even though the crosslinked epoxy will not melt, this transformation threatens the load-carrying capabilities of the construction as stiffness dramatically decreases. In our case temperatures may rise due to friction; multiple impacts during long transits will results in a lot of energy to dissipate.

The glassfibres used are supplied by Hexel and are named Hexforce 7581. The resin used in the infusion is from Hexion and goes by the name Epikote 04908. The material characteristics for the material are shown in table 4.1. These are the characteristics obtained after curing at room temperature and a post-cure in the oven. This post-cure further increases the T_g which is beneficial as explained above.

Type		Hexforce/Epikote	
Longitudinal modulus	E_1	24	GPa
Transverse in-plane modulus	E_2	23	GPa
In-plane shear modulus	G_{12}	3.52	GPa
Out-of-plane shear modulus	G_{23}	2.51	GPa
Out-of-plane shear modulus	G_{13}	2.24	GPa
Major in-plane Poisson's ratio	v_{12}	0.14	-
Thickness per ply	t	0.23	mm

Table 4.1: Material characteristics

4.2 Simulated static and dynamic behaviour

Before actually producing the design it is of great importance to first accurately describe its behaviour. This is achieved with a simulation model made in MatLab/Simulink, which has already been described and used in chapter 1. With this simulation model the design has been evaluated and adjusted where needed. After careful consideration and some trial and error a $[(0/90)_4(\pm 45)_2(0/90)_4(\pm 45)_2(0/90)_4]_S$ layup has been selected. The dimensions per plate will be 150 by approximately 600 mm with a thickness of ± 7.23 mm.

First we take a look at the static behaviour of the model as described by the analytical and static model. A graphic representation of the load-displacement behaviour is shown in figure 4.1.

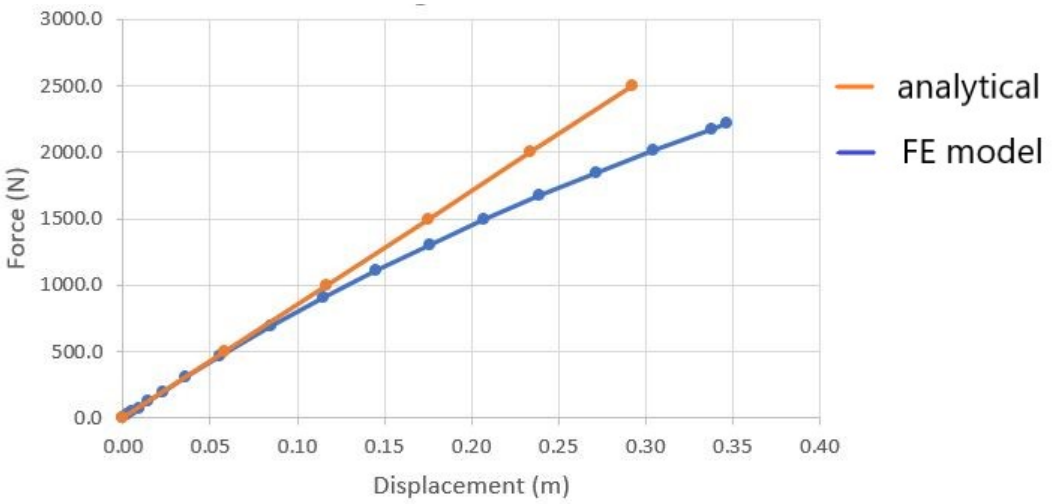

Figure 4.1: Comparison of results from analytical and FE-model

In figure 4.1 two characteristics are shown. One according to the linear model and another one based on a non-linear Finite Element Model (FEM). The FE-model is used as an input for simulation of the dynamic behaviour in chapter 5. The response to a standard input pulse, as defined in the first chapter, can be seen in figures 4.2 and 4.3.

As can be seen the seat, with a weight of 100 kg, accelerates with roughly 33.5 m/s^2, while the input pulse has a magnitude of 40 m/s^2, a difference of 16%. Furthermore, the maximum compression is less than 30 cm, the theoretical limit value for the compression of this prototype. As a result of the input pulse the theoretical response also shows a small negative deflection. In the negative part of the deflection the force-displacement curve has been extrapolated.

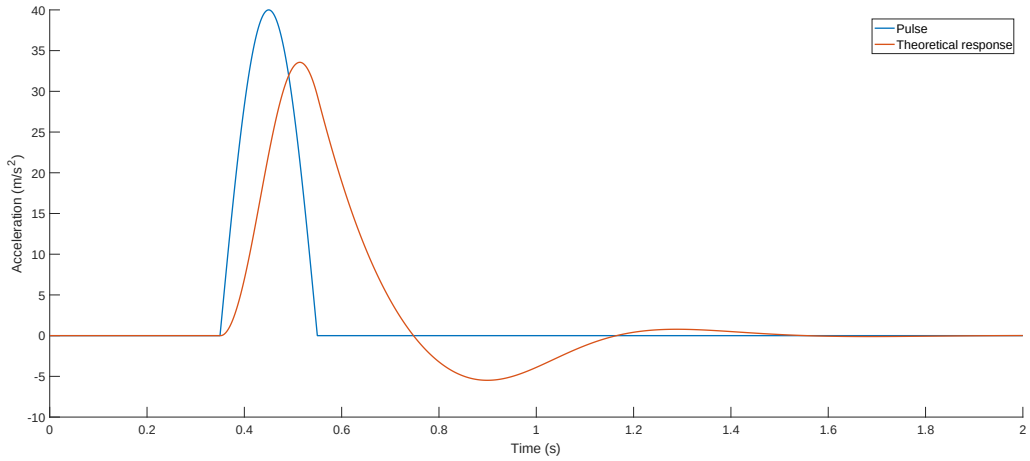

Figure 4.2: Example of theoretical prototype response for 40 m/s^2 pulse

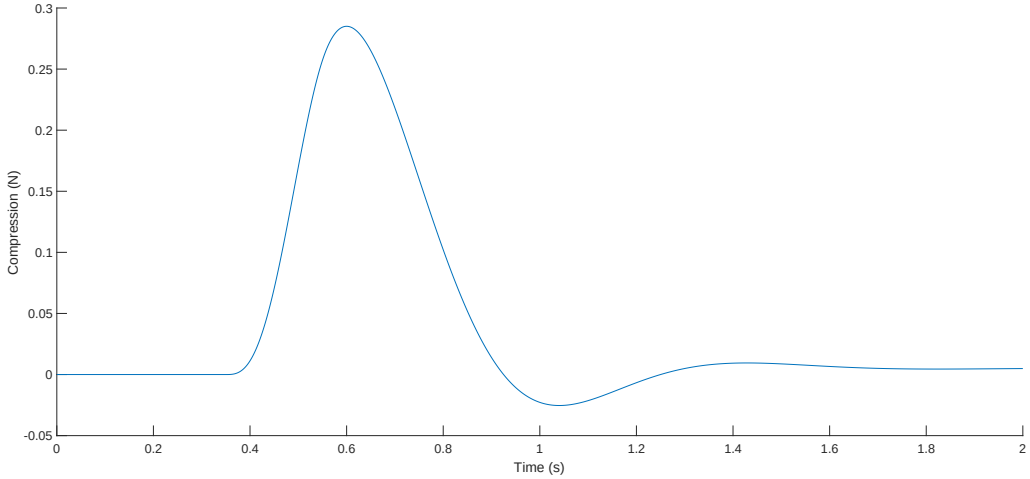

Figure 4.3: Theoretical compression in time for prototype

In figure 4.2 and 4.3 the mass and damping are fixed at 100 kg and 1000 kg/s. However, it is preferred that the damper can be adjusted to either increase or decrease the damping coefficient and occupants also have different weights. That is why the in figure 4.4 and 4.5 the mass and damping coefficient have been varied to investigate its effects.

It can be seen that increasing the mass is beneficial for the maximum amplitude up to 125 kg. Surpassing this limit causes the seat to bottom, which in turn produces a sharp spike in accelaration. In the model this has been simulated by enforcing a penalty on the stiffness. The graph which agrees with earlier presented research. The opposite holds for the damping coefficient; decreasing leads to improved performance when it comes to shock isolation. However, when falling below 750 kg/s the same bottoming effect is observed.

The prototypes behaviour will be further described in the next chapter. This will also feature comparisons with the currently used designs and evaluation of the seat performance after testing. The next section describes the production procedure of the composite plates in more detail. This enables other researchers to produce the exact same panels for future research on this topic.

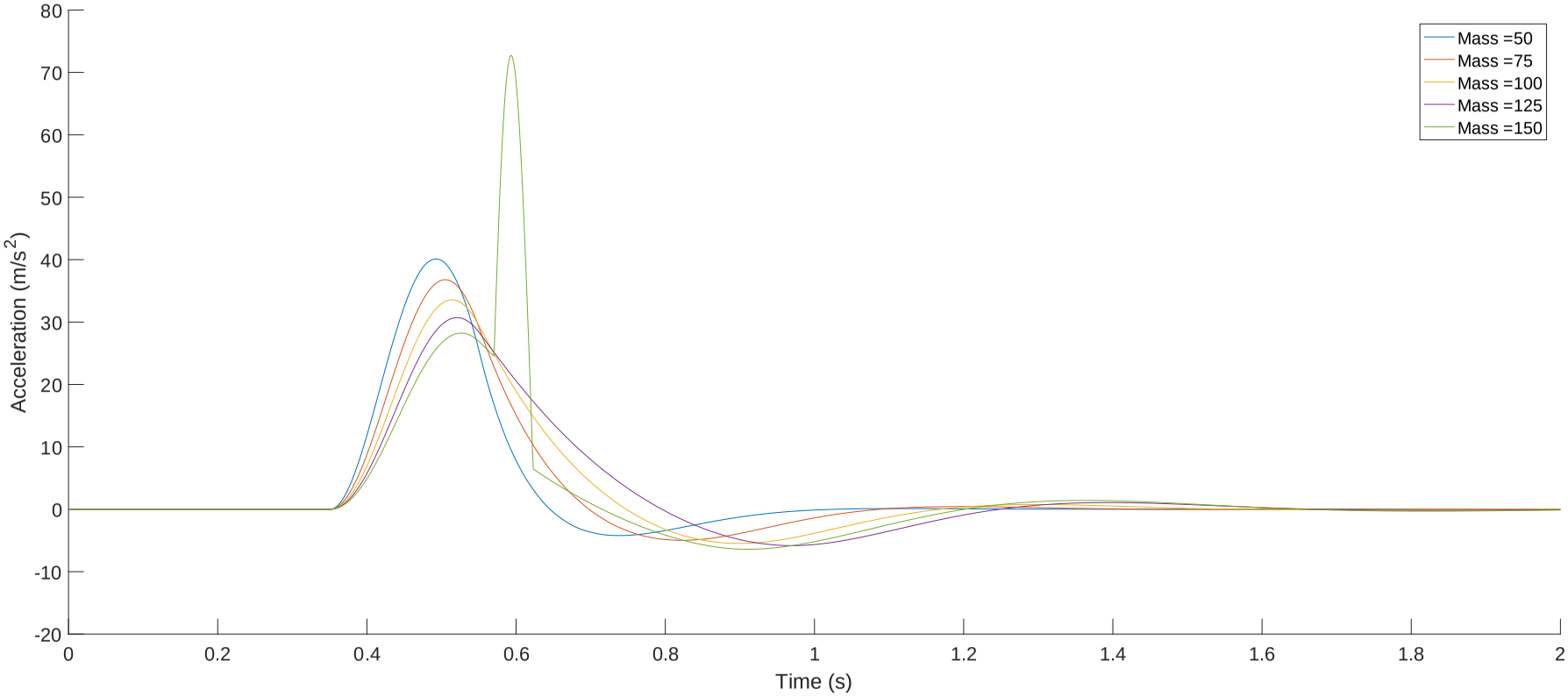

Figure 4.4: Example of seat response for 40 m/s^2 pulse

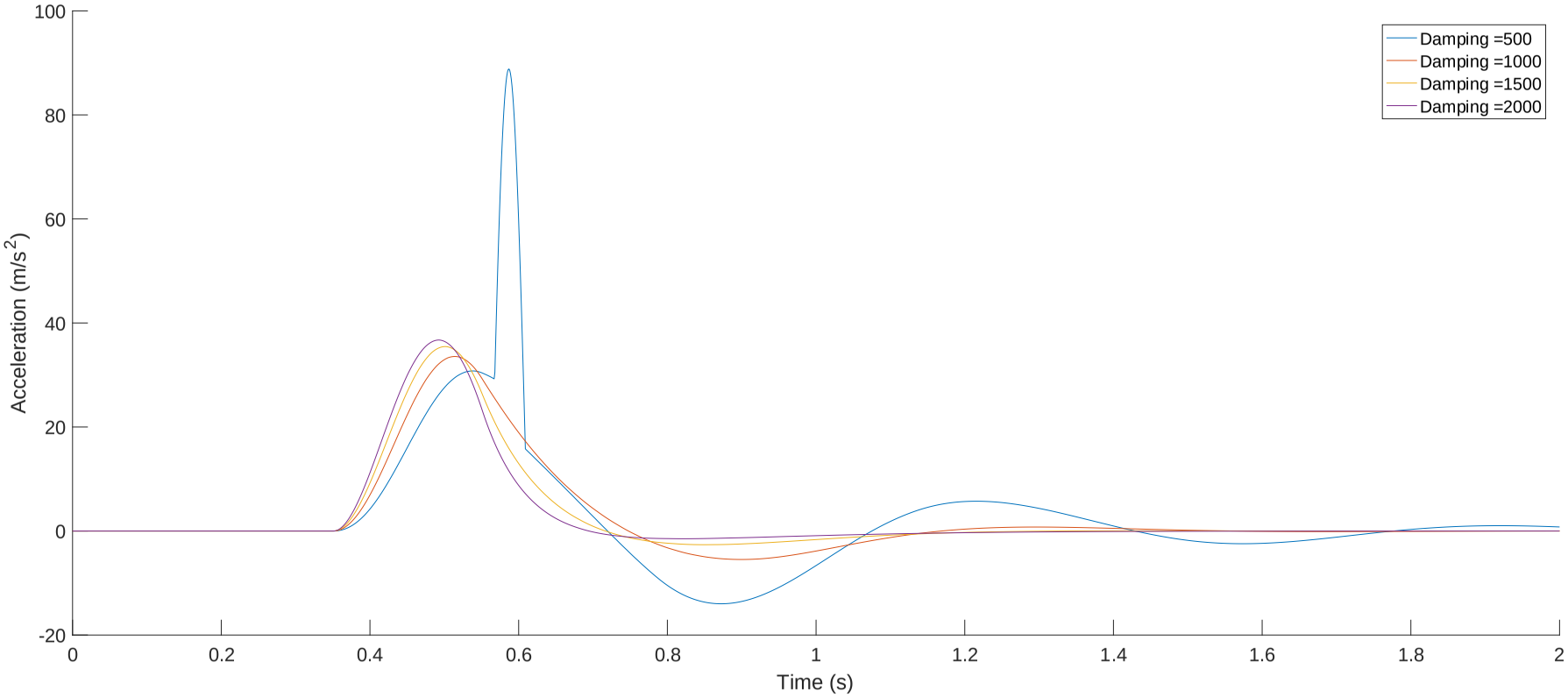

Figure 4.5: Example of seat response for 40 m/s^2 pulse

4.3 Production procedure

In this section the production procedure of the resilient parts for the prototype will be elucidated. As mentioned before these parts are made of Glass Fibre Reinforce Polymer (GFRP), which in turn is made from woven glass fibre layers infused with epoxy through a process called vacuum infusion. For the production of the composite plates a range of materials and equipment is needed. In order to offer a simple overview these have been listed on the next page and will be illustrated later.

The materials needed are:

- Aluminium plate
- Release agent
- Sized glass fibre fabrics
- Sandpaper
- Peel ply
- Breather
- Cytectape
- Office tape
- Plastic tube
- Epoxy
- Hardener

Beside materials we also need some equipment. The folowing equipment is needed:

- Working station
- Vacuum pump
- Fibre cutting working station
- Curing Oven

The first production step is the dimensioning of the glass fibre weaves, which is described next.

Dimensioning of the glass fibres

For the prototype four composite plates are needed. These plates will be produced per two. First, two large plates measuring 200mm by 1270mm are produced. Then these are both cut in half and trimmed afterwards to obtain four plates measuring 150mm by 600mm.

As mentioned before the selected layup for the plates is $[(0/90)_4(\pm45)_2(0/90)_4(\pm45)_2(0/90)_4]_S$. Thus every plate will have 32 plies which will be cut from woven glass fibre. The glass fibre is supplied on a large roll with a width of 1270mm and trimming of the unprocessed fibres is done with the Gerber machine, which can be seen in figure 4.6.

For the (0/90) plies strokes of 200mm by 1270mm will be cut off with the Gerber cutting machine. This leaves enough room to trim the plates after production. For the 2 large plates 48 of these layers are needed. This results in total of 9.6 m needed from the roll.

The ±45 layers are created by cutting the fabric under 45 degrees with the Gerber machine. For 2 plates, 16 of these layers are needed. This results in a total of 5.6m needed from the roll. Both cutting paterns can be seen in figure 4.7. So in total, roughly 15.2m of fabric is needed from the supplied roll. In practice, the Gerber machine calculates the most effective cutting patern by itself, which will probably reduce the amount of material needed.

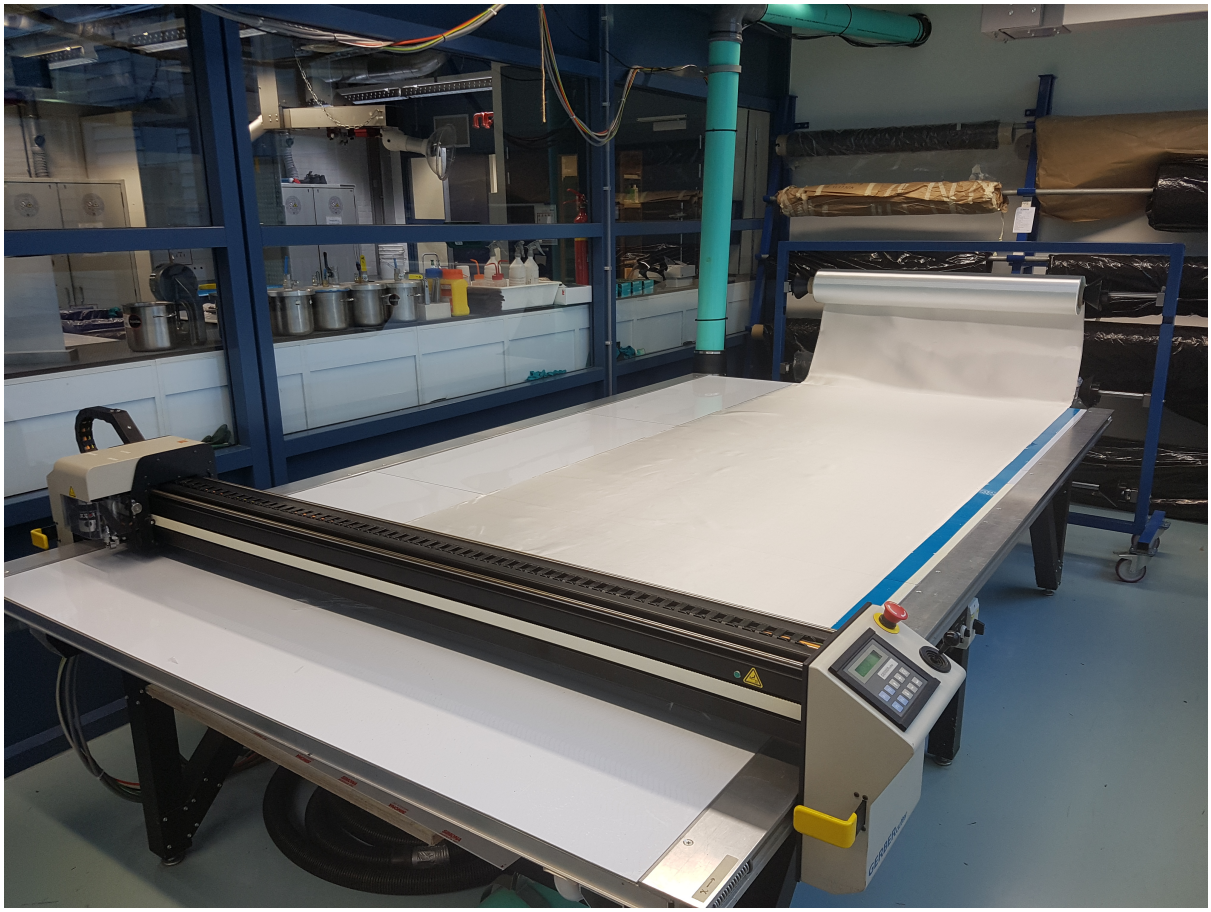

Figure 4.6: The Gerber cutting machine

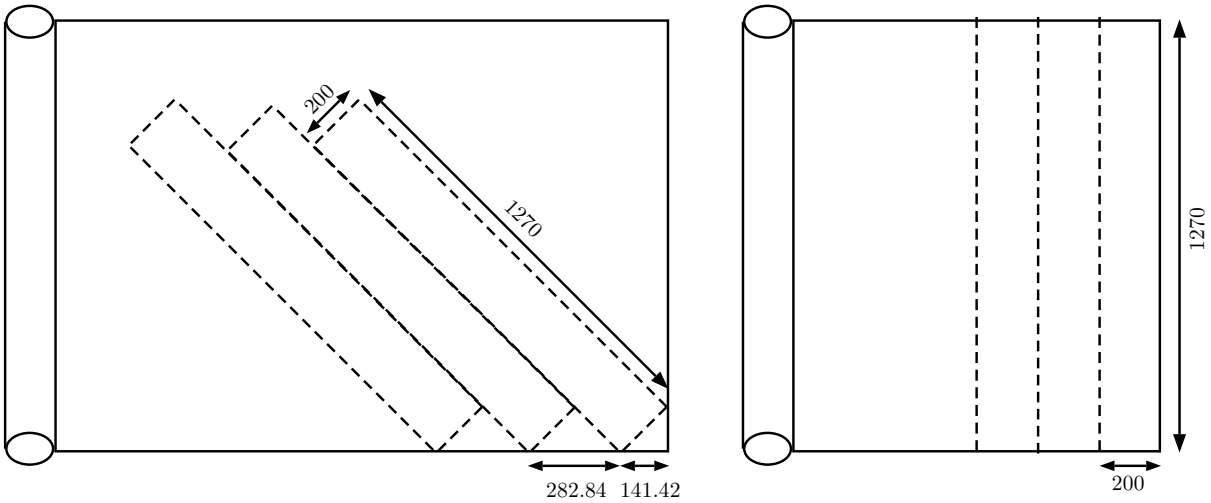

Figure 4.7: Cutting patern used for $(0/90)$ and ± 45 plies

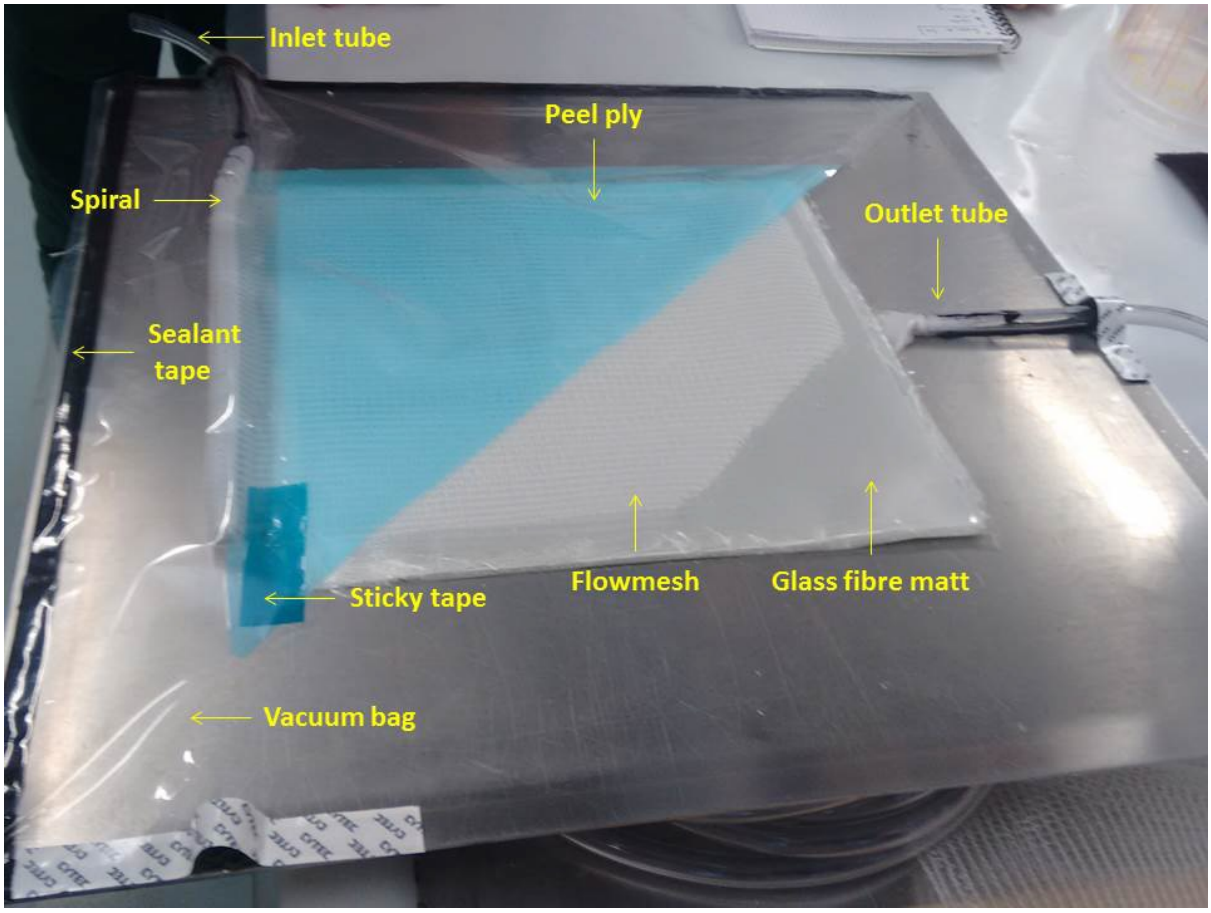

Figure 4.8: Overview of vacuum bag elements (courtesy of Salwan Al-Jaberi)

Vacuum infusion procedure

After cutting the plies and stacking them, they will be infused with resin. For this purpose a mold is used together with plastic foil to create a vacuum around the product. The so-called vacuum bag consists of several elements. These can be seen in figure 4.8 which shows the same setup for a square plate. Here the materials have been dimensioned to create a good view on the different parts.

The aluminium plate is used as a foundation to stack the sized fabric plies on. These fabrics have been sized to 0.20 by 1.27 m. The plate is thoroughly cleaned and the sides are scrubbed with sand paper and also cleaned. Office tape is applied to the scrubbed sides to protect them whilst applying the release agent to the rest of the aluminium plate. The sides are to remain rough so the Cytectape, which is applied later, will stick to the plate. The black dubbel sided Cytectape is used to attach the vacuum bag to the aluminium mold.

Next, two layers of the release agent, Marbocote 227, are applied. The first layer in horizontal and the second one in vertical direction to ensure the entire plate is covered with release agent. There has to be a minimum of 5 minutes between applying the first and second layer to make sure the release agent dries properly. These layers prevent the product from sticking to the aluminium plate.

After applying release agent the office tape on the sides is removed and the Cytectape is applied. Gloves are used to prevent the tape from getting contaminated with grease. Also, the top is still

covered with the protective film. The fibres are then stacked on to the plate according to the determined lay-up. A total of 32 layers is used in the layup $[(0/90)_4(\pm45)_2(0/90)_4(\pm45)_2(0/90)_4]_S$. The fabrics should be handled with care to avert fibre waviness from occurring. Loose fibres on the sides are removed to prevent leakages of the vacuum bag, which is applied later.

A peel ply is applied next over and under the fibres. After curing, removing the peel ply leaves a rough surface which is perfectly suited for further processing. This makes the time-consuming roughening of plate after production superfluous. This is followed by the flow mesh and blue perforated foil. The flow mesh is used to guide the flow of the resin. The resin flows through the low resisting mesh after which is seeps down into the product. Blue perforated foil is used to prevent the mesh from sticking to the product.

The inlet tube is attached with Cytectype and sharp edges are taped with office tape. A spiral tube is attached to the inlet tube to quickly establish a flow front over the full length of the plate. Breather fabric is place between the outlet tube and the stacked fibres to create an area of increased resistance. This increases available time for the resin flow front to reach all corners of the product. At the sides and outlet a 1 cm margin is used to prevent the resin from flowing around the fibres instead of through the fibres.

Finally, the vacuum bag is applied over the Cytectape after first removing the protective film. The construction is tested by switching on the pump, initiating a vacuum and checking whether the vacuum is conserved after switching of the pump. Then, the resin is sucked into the system with a vacuum of 50 $mbar$.

The resin consists of 100 weight units of epoxy and 30 weight units of hardener. To estimate the amount of resin needed the tube and plate dimensions are regarded. The in- and outlet tube have a combined length of approximately 2 meters and a diameter of 0.8 centimetre, the product is 20 cm wide, 127 cm long and 7.36 mm thick. The amount of resin needed is calculated as follows:

$$32 \cdot 0.00023 \cdot 0.2 \cdot 1.270 + 2 \cdot 0.008^2 \cdot \pi = 2.07L \tag{4.1}$$

As can be seen the dimensions of the plate are multiplied by the thickness to obtain the volume. We also account for 2 meter of tube used to transfer the resin to the plate. After applying some margin to account for the other fabrics used like flow mesh and bleeder, in total, including a safety margin, $2.5L$ of resin is needed per plate. For the whole process of infusing the plate including preparation 1 day of 8 hours was scheduled.

After completion of the infusion the inlet is closed and the product is cured for approximately 2 days at 500 $mbar$ resulting in a 50 percent resin content. After which the plate is post-cured in the oven for another 10 hours at 75 $°C$. This is followed by cutting the plate in half and trimming it to the desired dimensions.

This results in four trimmed composite plates which are used in the construction of the prototype. These can be seen in figures 4.9 and 4.10. The plates are combined with parts from other seats provided by TNO. The final result can be seen in figures 4.11 and 4.12. As can be seen in these pictures, the seats itself is not attached and the pedestal used has to be lowered if this resilient mounting is to be used in a final commercial product. This however has no real influence on the test results and thus the resilient mounting is tested in the presented configuration.

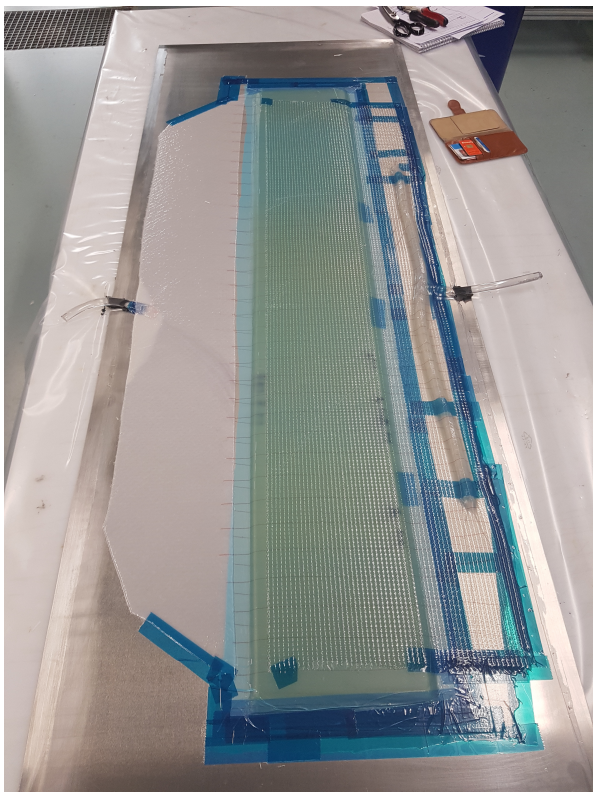

Figure 4.9: Product after vacuum infusion

Figure 4.10: Product after post-cure

Figure 4.11: Final prototype side view

Figure 4.12: Final prototype

Chapter 5

Prototype testing

In this chapter the testing of the prototype will be described. The prototype has first been subjected to static testing at the lab of TNO Netherlands. This was followed by dynamic drop tests at the Royal Netherlands Sea Rescue Institution (KNRM) in IJmuiden. For both tests the results will be presented together with expected results based on the models described earlier. This way we can validate the performance of resilient mounting.

5.1 Static testing at TNO

The prototype was first tested statically. In this test the seat is loaded incrementally with weights. Each time weight was added the deflection in the vertical plane was written down as well as the weight used to obtain this deflection. The test is stopped at a weight of 117.5 kg to not overload the prototype before the dynamic testing. In figures 5.1 and 5.2 the resilient mounting is featured with one and five weights respectively. In these pictures the typical s-shape that the construction assumes can be clearly seen. The results obtained at each load increment are shown in table 5.1. As expected the structural stiffness decreases as the deflection increases.

Weight (kg)	**Force** (N)	**Deflection** (m)	**F/u** (N/m)
23.5	230.535	0.028	8233
47	461.07	0.059	7815
70.5	691.605	0.087	7949
94	922.14	0.12	7685
117.5	1152.675	0.155	7437

Table 5.1: Results for static prototype testing

If table 5.1 is plotted figure 5.3 is obtained. Next, we can use the expressions from the analytical method and the FE-models featured in chapter 3 as a benchmark. This produces figure 5.3. It can be seen that the results closely agree with the theoretical calculations. As expected the behaviour is non-linear in nature and complies with the FE-model.

Figure 5.1: deformed resilient mounting with 23.5 kg

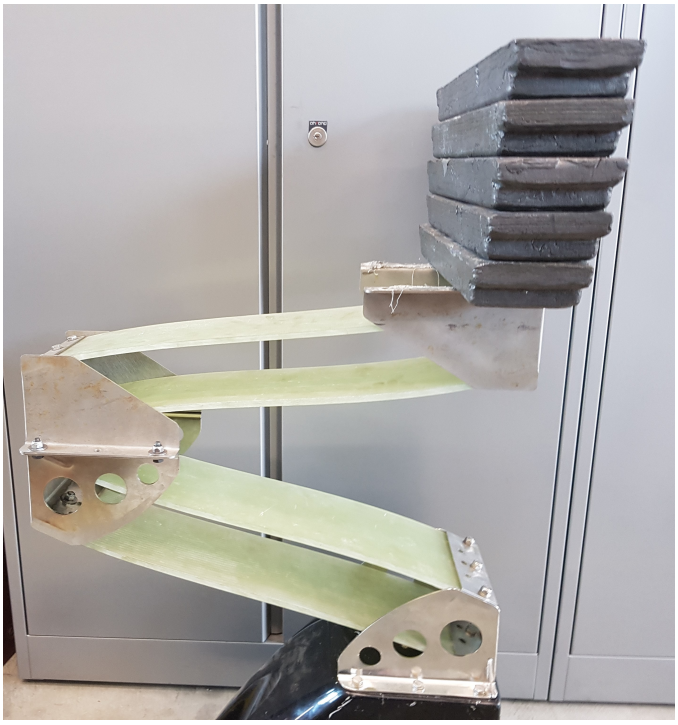

Figure 5.2: deformed resilient mounting with 117.5 kg

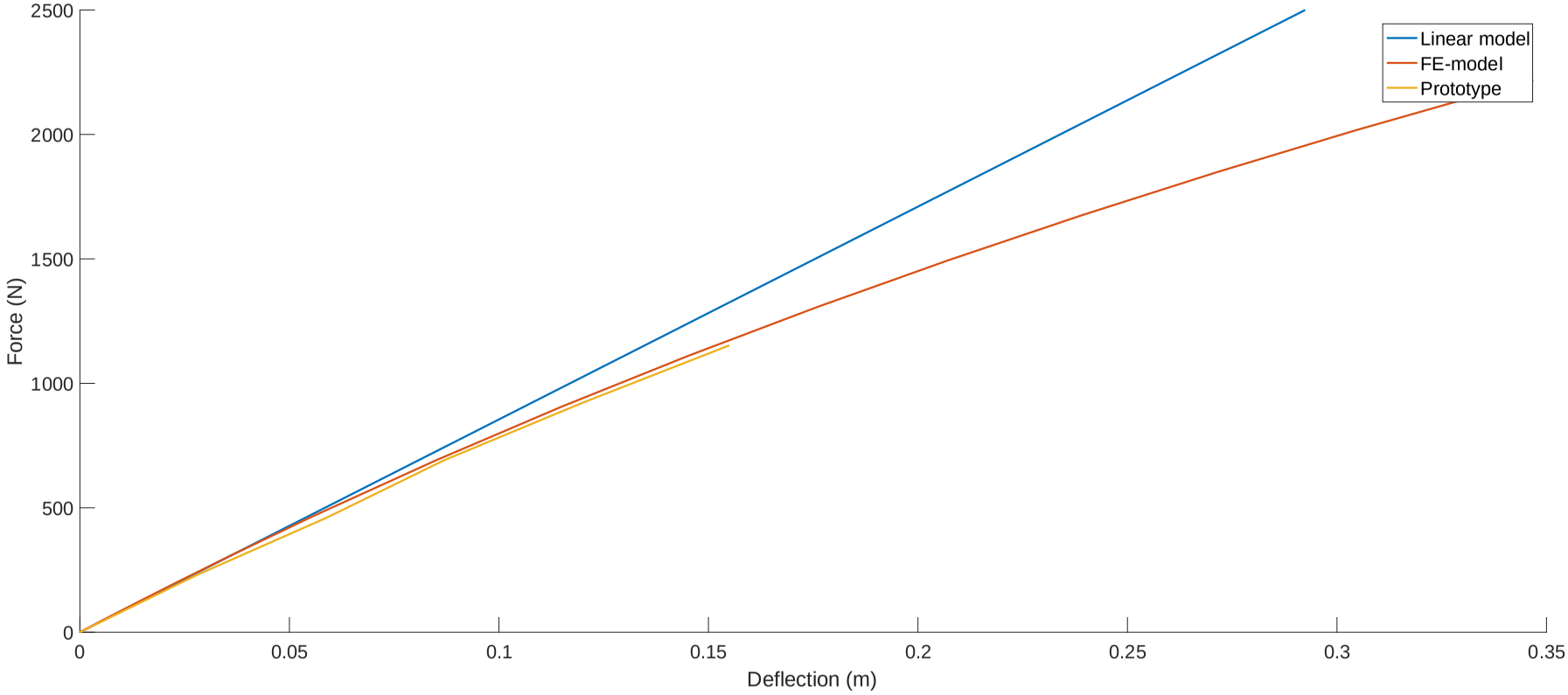

Figure 5.3: Benchmark comparison for static test of prototype

5.2 Dynamic drop tests at KNRM IJmuiden

Dynamic testing of the prototype would initially take place at the TNO laboratory. Their facilities include a 1000 kg drop tower, which is able to simulate an impact event of a fast planing craft. The prototype is mounted on the drop weight, which subsequently is dropped from a predetermined height. Instead of dropping on the floor, the weighted construction drops into a pile of foam blocks. By altering the amount of foam blocks one can influence the pulse time of the impact. This setup has been used before by the TNO resilient mounting task group and is featured in figure A.1.

Unfortunately, due to technical and methodological flaws the drop tower could not be used. One of these flaws include possible distortion of the results provoked by the drop weight bouncing back up after impact. This was discovered recently and after consulting with TNO and KNRM it was decided to make use of the KNRM test facilities instead. Their test setup has several advantages compared to the one used by TNO and will be described in the next section.

Test setup KNRM IJmuiden

The KNRM is located in the harbour of IJmuiden. They have multiple boats and cranes at their disposal, which gives them the unique opportunity to actually drop a boat from a predetermined height into the water. Hopefully, this results in even more realistic results compared to the setup used by TNO. For this test a small boat was used with a length similar to that of the FRISC 9.6m and a crane with a lifting capacity of 6000 kg. Both can be seen in figures 5.4 and 5.5.

The boat can be rigged up with two jockey seats. For our test two types of jockey seats are fitted to the boat. The first one is a commercial model currently available referred to as Composite Leaf Spring (CLS) jockey seat and the second one is the prototype with the newly designed resilient mounting. The prototype has been preloaded and a total weight of 50 kg is used as an occupant and a customized air piston has been used as a damper. This weight was chosen to ensure the prototype does not break and remains available for future research. Later in this chapter the results will be extrapolated for heavier occupants.

Three brands of accelerometers are used on the boat base and both seats. This serves multiple purposes. Firstly, due to time and planning constraints, it is only possible to perform this complete test on one day. Therefore, the extra recorders can be considered as a backup for the main recorder. Secondly, the main recorders record their data in a 16 bit binary format. At time of testing the KNRM was not confident they would be able to process the raw data of the so-called MAREC recorders.

They therefore also supplied recorders of the brand GCDC. These record their data in Comma Seperated Value (CSV) format, which can be processed quite easily with commercially available computer programs like Microsoft Excel and MatLab. However, both the MAREC and GCDC recorders are not able to provide "live" data. To ensure a smooth progress of the test live data is of great importance. For this purpose TNO supplied the LORD recorders. In total three drops were performed. The results of these drops are described next.

Figure 5.4: KNRM crane and boat used for drop test

Figure 5.5: KNRM boat used for drop test

Results of drop test

The boat was dropped three times and as stated before the data has been collected with three brands of accelerometers. In total 9 recorders were used and the data was processed with MatLab. The program written to process the data can be found in appendix F.

Figure 5.6 shows one of the recorded drops. The data in this figure was recorded with the GCDC recorder. It can be clearly seen that the resilient mounting isolates the shock partially, which is indicated by the black arrow. 76% of the shock is transferred from the base of the boat to the seat.

Another noticeable event is a large negative peak in acceleration. This is due to the resilient mounting touching its upper boundary which is introduced after application of a preload. Also, this might be due to the fabricated damper partially working as a spring because of the compressibility of the air inside or because the damper is not damping sufficiently. The applied preload is 461 N. In total, the impact event lasted less than 1.5 seconds. The recordings of the other drops are featured in appendix G.

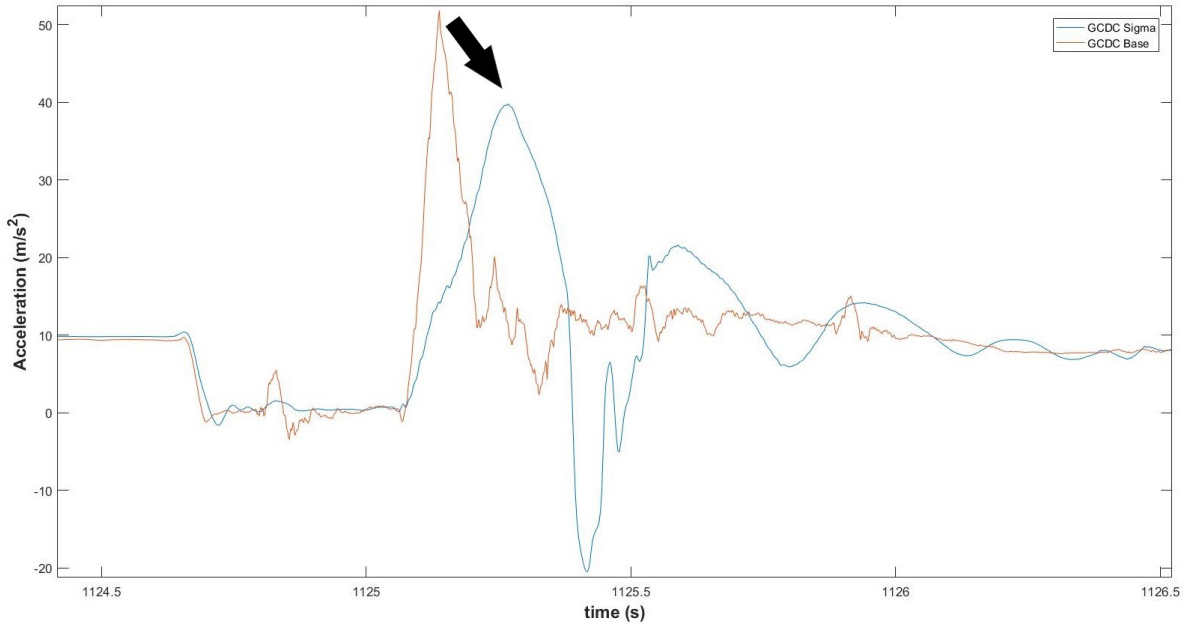

Figure 5.6: First drop with prototype during KNRM tests

These results shall be compared with the predictions of the dynamic model described earlier. First the measured base excitation pulse itself will be used as input. Then a sine pulse will be used which resembles the base excitation of the boat as several authors have suggested [9, 13]. Differences in response between the two can then be identified and the predicted seat response can be compared with the measured seat response. When the upper or lower support of the construction is touched in the model a penalty on the structural stiffness will be enforced. This will be clearly stated when applicable.

5.3 Comparison with dynamic MatLab model

Figure 5.7 shows the base excitation pulse as measured during the drop test. The predicted response of the prototype by the dynamical model is also shown together with the actually measured response.

Besides the damping coefficient and structural stiffness penalties for hitting the lower and upper supports, which has been estimated by trial and error, all other variables are known. In general, the results of the model are in agreement with the measured response; the shape and duration of both pulse is very similar. Differences between the two are also observed: the maximum amplitude of the measured response exceeds that of the predicted behaviour by 8.26% and the effect of hitting the top support of the resilient mounting differs.

In the prediction the top support is hit multiple times, while in reality this only happens once around $0.7s$. Hitting the top or bottom support (bottoming) causes almost instantaneous increases in acceleration and proves difficult to model accurately.

The base excitation pulse will now be replaced by a sine-shaped excitation pulse. This pulse was described and used earlier as an approximation of a repeated shock impact event to investigate and predict the behaviour of several types of resilient mountings. The first question to ask is which period should be used for the half sine approximation of the measured excitation pulse. This is a difficult question to answer and, therefore, a first disadvantage of the sine approximation method.

If the excitation pulse in figure 5.7 is regarded more closely, one can see that the total duration of the event is $359ms$. In the first part of the pulse however also resembles a half sine shape with a duration of roughly $150ms$. A half sine with an amplitude of 40 m/s^2 and a period of 200 ms is therefore used.

The results of using the sine approximation instead of the measured excitation are featured in figure 5.8. All variables are kept equal for both cases. The reduced resemblance with between the two responses is clearly visible as well as the difference in acceleration after the event; the sine pulse drops back to 0 m/s^2, while in reality an acceleration of 9.81 m/s^2 remains present. In the response calculated by the dynamic model the upper support is hit numerous times. It does, however, predict the maximum amplitude more accurately; the difference is reduced to 0.25%.

In figure 5.9 a sine-shaped pulse is again used, but this time it has been changed to remain at 9.81 m/s^2 after the drop. The change is significant; the shape of the measured response is approximated much better.

Based on the preceding, it seems like a logical choice to use the half sine approximation in the early stages of product development, as was done in this thesis. In this stage determining the maximum amplitude of the response and thus the isolating behaviour of the resilient mounting are of great importance.

After this stage it is worth the effort to accurately determine a representative impact event for the boat on which the resilient mounting is going to be used to get a better understanding of the global behaviour up to 2 seconds after impact. If this is not possible the sine-shaped pulse should at least be corrected in such a way that it starts at 0 m/s^2 and ends at 9.81 m/s^2.

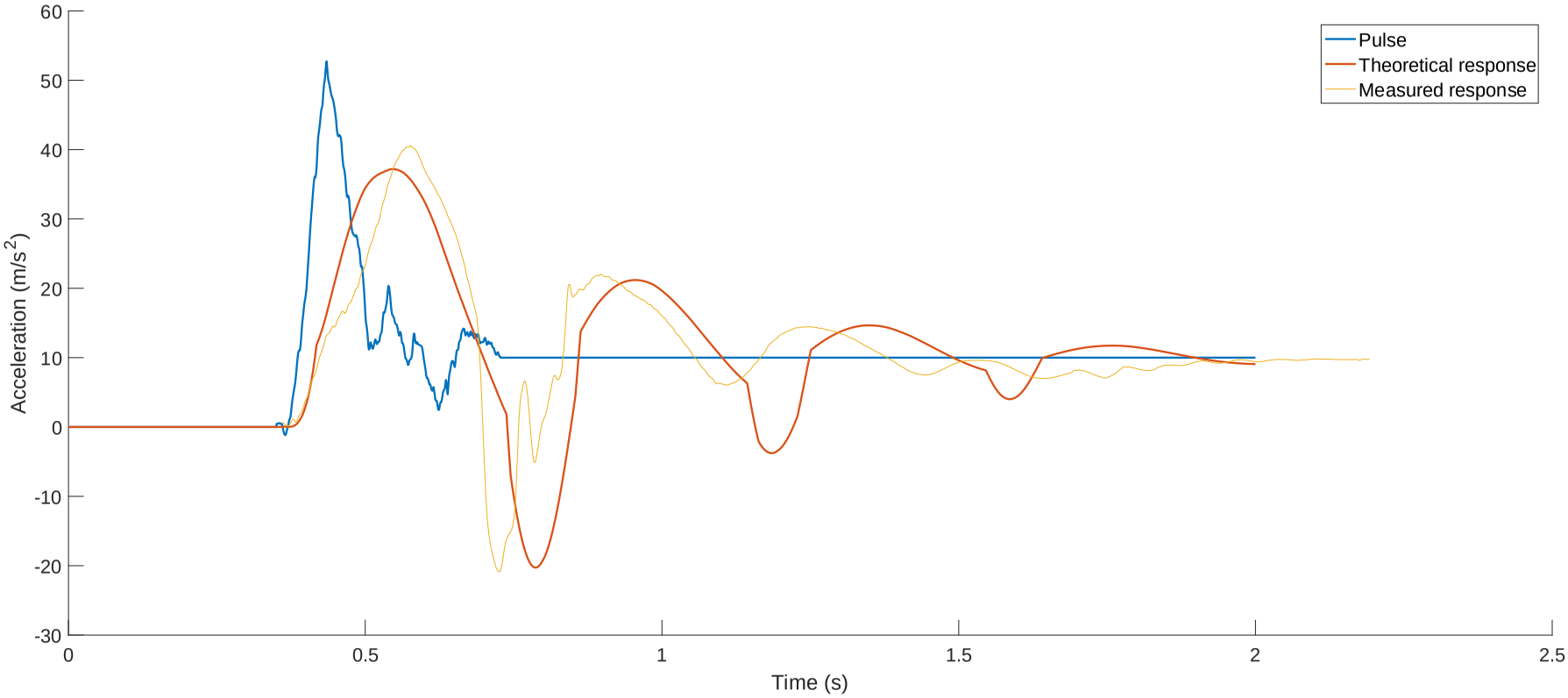

Figure 5.7: Measured and theoretical acceleration of prototype

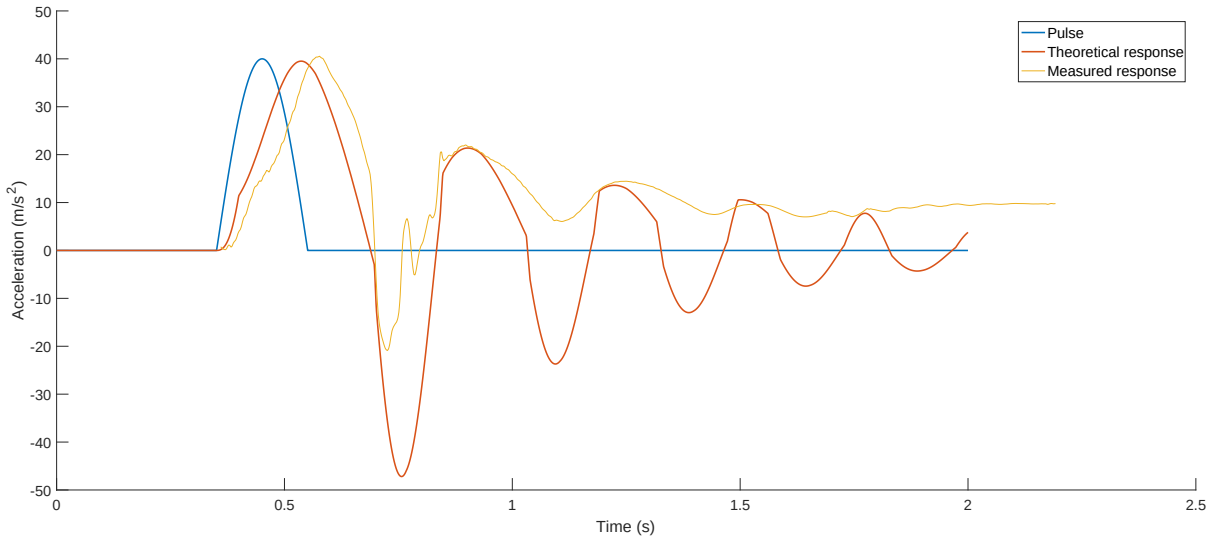

Figure 5.8: Measured and theoretical response of resilient mounting 3

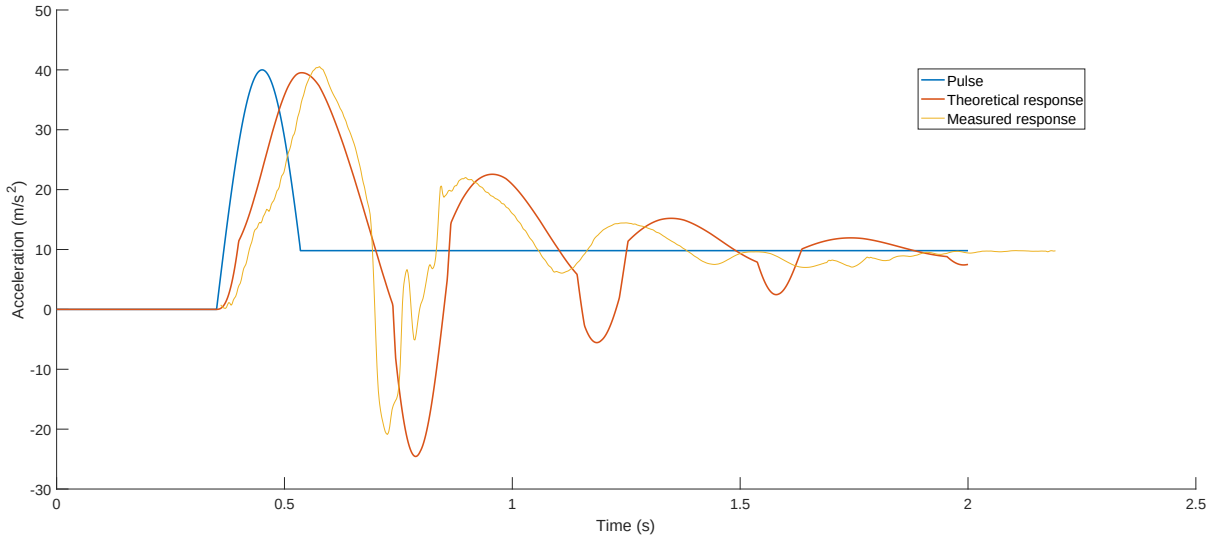

Figure 5.9: Measured and theoretical response of resilient mounting 2

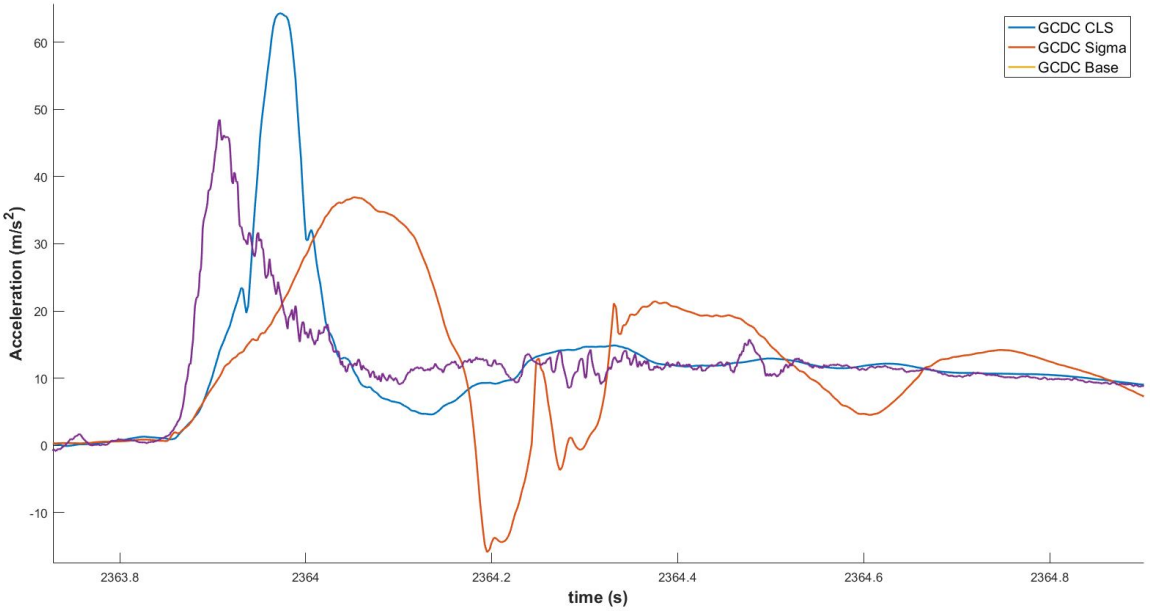

Figure 5.10: Measured and theoretical response of resilient mounting 4

5.4 Comparison with CLS Jockey Seat

As told before, the Sigma seat prototype was not the only seat tested during the drop tests in IJmuiden. The Sigma seat prototype was also tested simultaneously with the CLS jockey seat. This jockey seat features one spring element consisting of two composite plates and a maximum compression of 15 centimetres. The design has been described in more detail in chapter 2.

In figure 5.10 similar results are shown as in figure 5.6, only this time the response of the CLS jockey seat is included and this particular drop is the third drop of three in total. The difference in performance between the two seats is striking; the Sigma seat clearly isolates the shock partially as described before, whereas the CLS seat is forced against its lower support. This leads to a acceleration surpassing 60 m/s^2 which is higher than the initial impact experienced by the boat.

The seat currently used by the Royal Netherlands Navy is even more rigid and the maximum compression is much less. The CLS seat has a more or less linear stiffness of 24 kN and a maximum compression of 15 cm was determined, whereas the other seat features a stiffness of $42kN$ and a maximum compression of 8 cm. Simulations show that this would lead to accelerations far exceeding 100 m/s^2 and aircraft ejection seat standards. This will cause acute injury to occupants undergoing these accelerations [1].

5.5 Extrapolation of results for mass, damping coefficient and preload

During testing the seat was rigged with 50 kg and the damping was limited. In this section the preceding results will be used to extrapolate the behaviour of the Sigma seat prototype for the variables mass, damping coefficient and preload. This is followed by an optimization for these variables. For this purpose the dynamic model has been extended.

In figure 5.11 the response of Sigma seat has been extrapolated to higher occupant weights. The mass is varied from 50 kg up to 150 kg. The damping coefficient is kept constant at 200 kg/s in compression and 250 kg/s in extension. The preload is set at 461 N. The values of both the damping coeffcient and preload are the same as measured during testing of the Sigma seat.

The results are in agreement with the theory presented in chapter 1. A higher mass results in a better isolation of the repeated shocks. The difference is significant; for a mass of 50 kg the maximum acceleration is 29.5% less than that of the boat. When the mass is increased to 150 kg half (50.5%) of the shock is isolated by the Sigma seat.

The same has been done for the damping coefficient keeping mass and preload constant at respectively 50 kg and 461 N as can be seen in figure 5.12. It can be clearly seen that increasing the damping coefficient also increases the maximum amplitude of the response curves. The amplitude is increased from 37.23 m/s^2 for a damping of 500 kg/s to 44.09 m/s^2 for a damping of 2000 kg/s. While increasing the damping coefficient is not beneficial for the maximum amplitude it is beneficial for the maximum compression of the seat. In figure 5.12 this is indicated by the fact that nor the upper or lower support is hit for damping coefficients above 500 kg/s.

Lastly, the preload is changed keeping mass and damping constant. The results are visualized in figure 5.13. For a preload of 0 N the maximum amplitude is 38.79 m/s^2 and for 750 N it decreases to 36.43 m/s^2 after which it increases to 36.74 for a preload of 1000 N. This suggests that an optimum is located somewhere between these values. For given mass and damping coefficient the results in figure 5.13 are not satisfactory. Isolation is only improved marginally and the behaviour after the peak response worsens for higher preloads. This is due to the resilient mounting hitting its upper support which is penalized in the model.

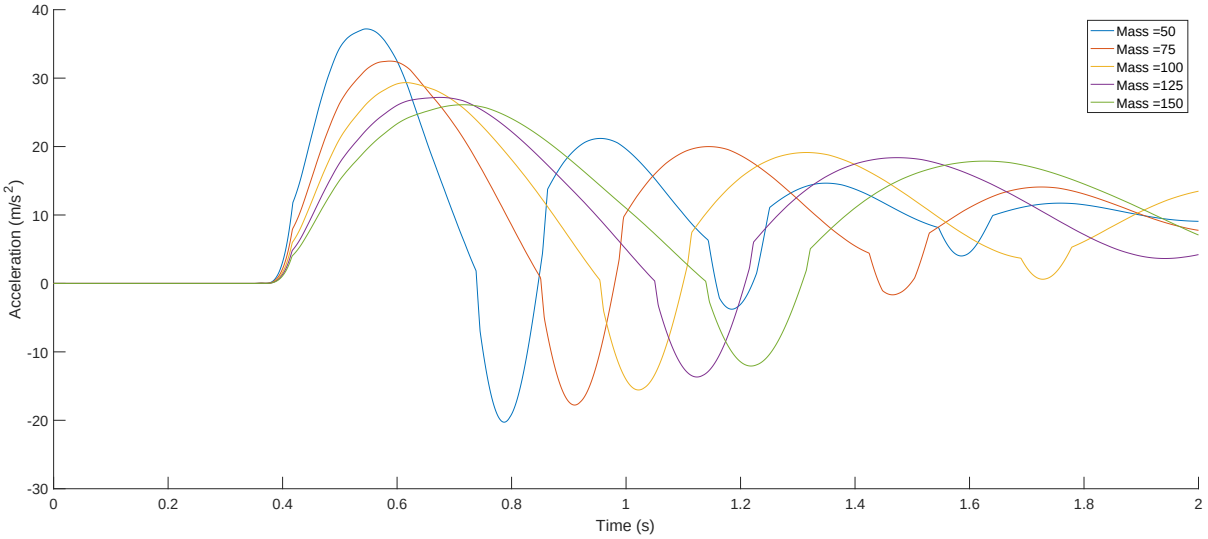

Figure 5.11: Prototype response for variation of mass

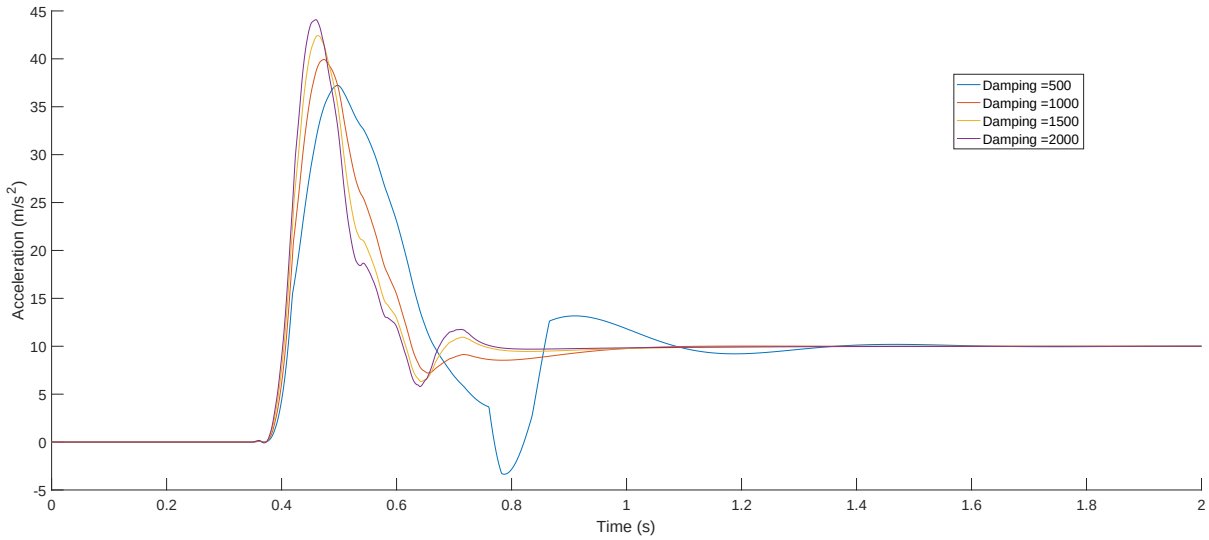

Figure 5.12: Prototype response for variation of damping coefficient

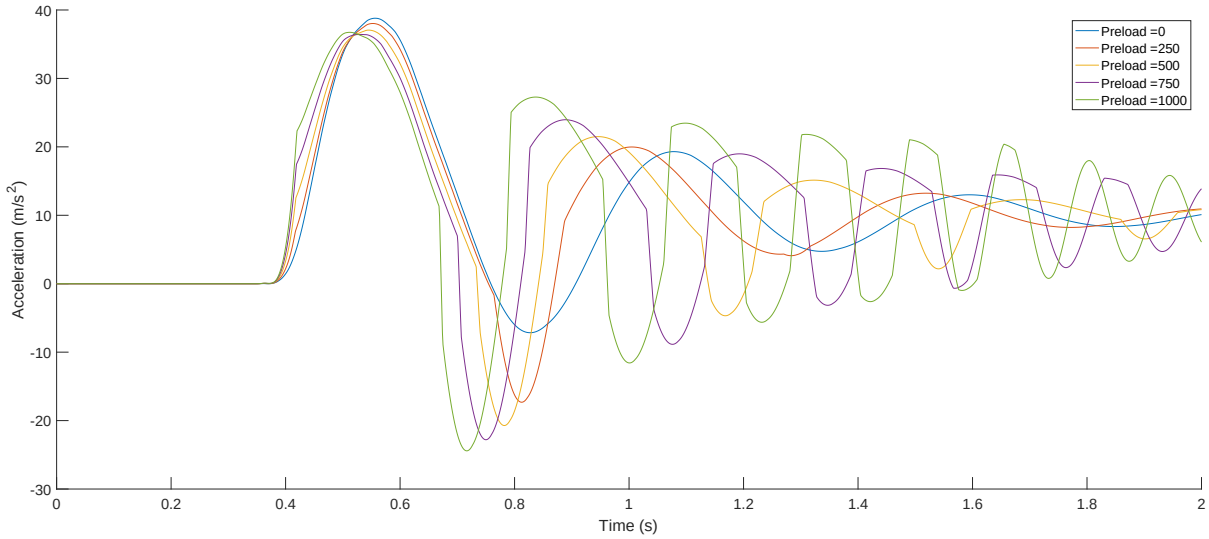

Figure 5.13: Prototype response for variation of preload

5.6 Brute force optimisation of mass, damping coefficient and preload

In the preceding section one by one the variables mass, damping coefficient and preload were altered to extrapolate the behaviour of the Simga seat. Results varied as, for example, increasing the mass proved to be beneficial for the shock response but contrary was true for the damping coefficient. Once again the dynamic MatLab model was extended. This time to include a brute force optimisation module. This module searches the best suiting damping coefficient and preload for a given weight increment. The combination of variables that results in the best isolation factor is regarded as best suited. This results in an overview over the best configuration for the prototype at each mass increment. This can be seen in table 5.2.

Mass (kg)	**Damping** (kg/s)	**Preload** (N)	**I.F.** $(-)$
50	300	500	0.6875
60	350	500	0.6413
70	400	700	0.6068
80	450	800	0.5788
90	550	700	0.5569
100	650	500	0.5390
110	800	200	0.5265
120	900	100	0.5156
130	1050	100	0.5159
140	1200	100	0.5166
150	1300	100	0.5162

Table 5.2: Optimised variables per mass increment for Sigma seat prototype

The responses for a mass of 60, 90 and 120 kg in combination with the constants from table 5.2 have been visualized in figures 5.14, 5.15 and 5.16. A significant amount of the shock is isolated by the seat and thus not transferred to the occupant. In all three figures a slight bump can be observed where the upper or lower support is hit. The optimisation algorithm does not mind these bumps and only selects the most beneficial response in terms of maximum amplitude. The maximum negative accelerations observed is about -10 m/s^2. This is an acceptable value for such a short duration of time.

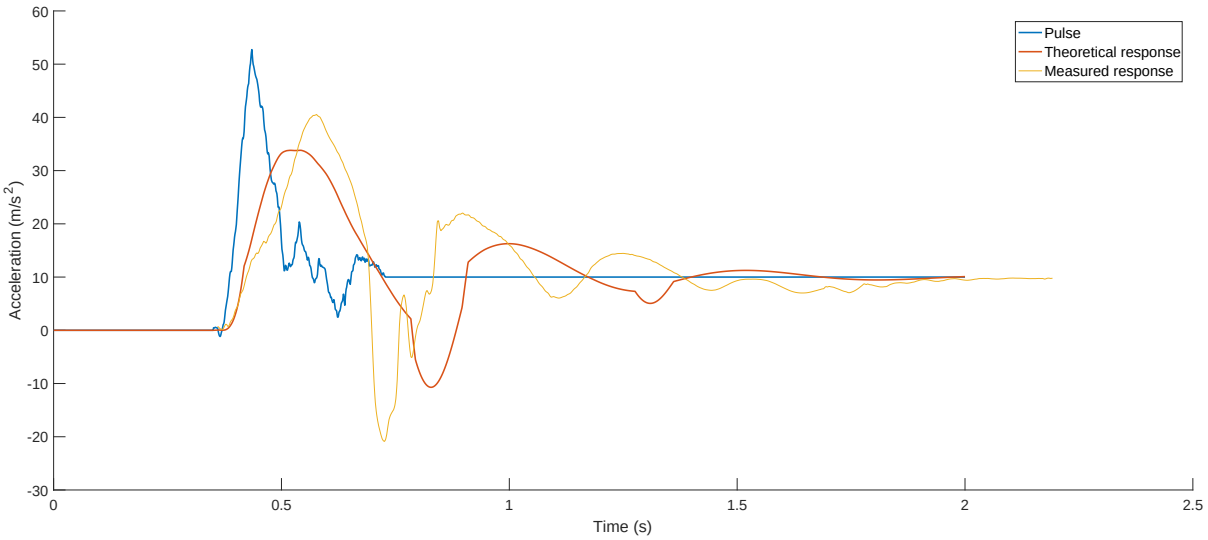

Figure 5.14: Optimised response for m=60 kg

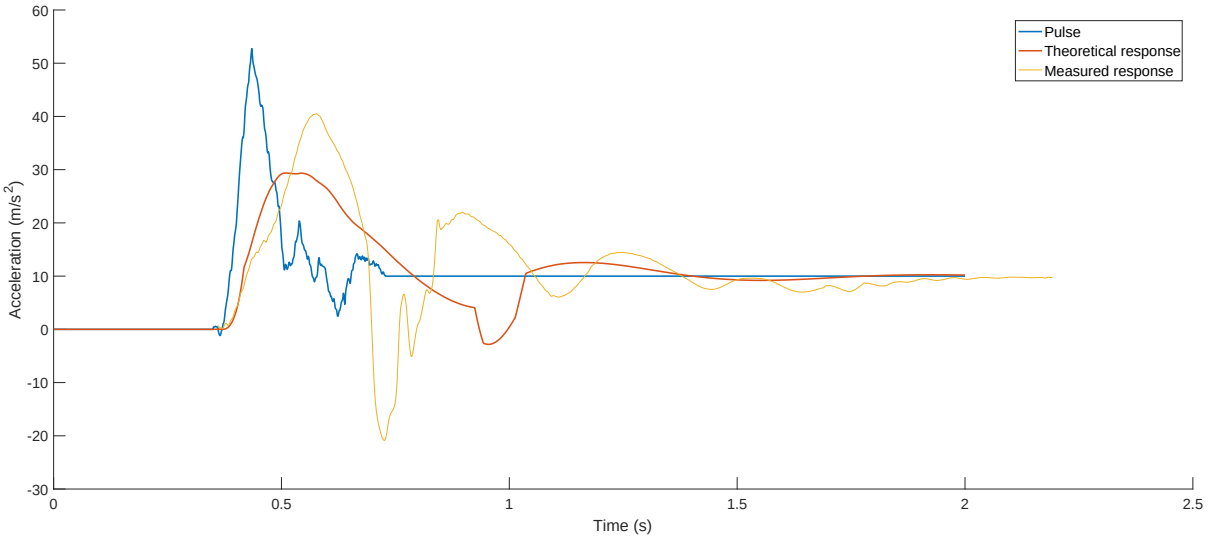

Figure 5.15: Optimised response for m=90 kg

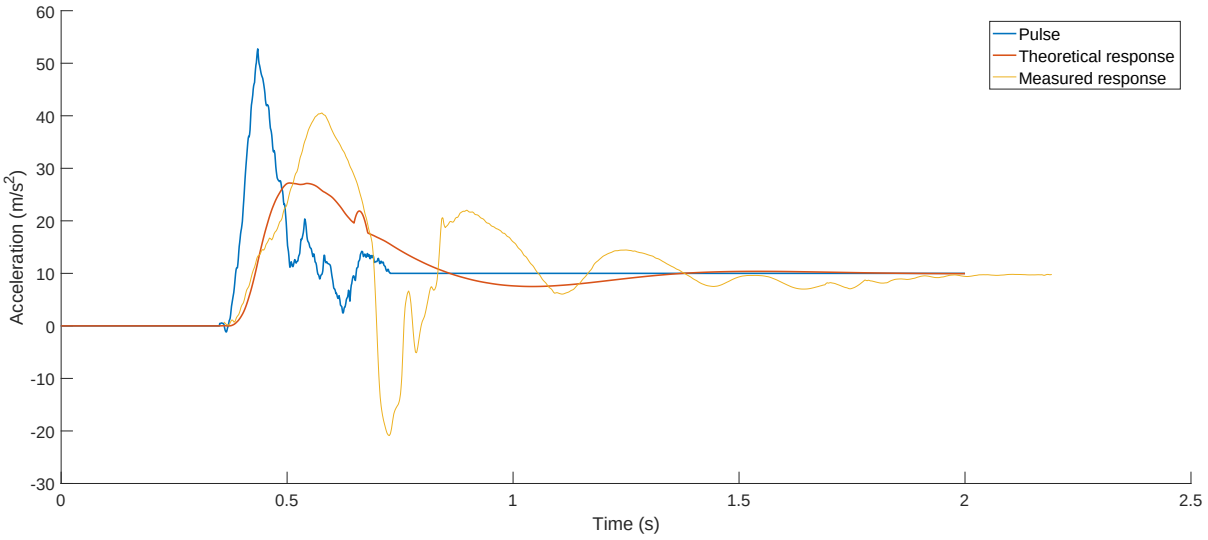

Figure 5.16: Optimised response for m=120 kg

Chapter 6

Conclusions & Recommendations

In this thesis persistent problems with the Jockey Seat for fast planing crafts were identified and tools to further analyse the problem were developed. Past research and existing solutions were presented along with two redesign directions. Both analytical and FE-models were used to efficiently analyse a large amount of designs. This resulted in the production of a first prototype, the Sigma seat. This seat has been tested both statically and dynamically. From this process the following conclusions can be drawn:

6.1 Conclusions

- Both past research and this thesis show that the commercially available Parallel Coil Spring (PCS) and Composite Leaf Spring (CLS) jockey seat do not perform as desired. When operating in severe conditions they do not isolate the Repeated Shocks experienced by the FRISC and other Fast Planing Crafts (FPC). This is due to the resilient parts being too stiff and/or the limited space for compression;

- The currently used Jockey Seat on the FRISC causes excessive loads on the occupants bodies when the FRISC is operated in tough conditions. According to previous research these loads may lead to both acute injuries and long-term damage;

- Redesigning the Jockey Seat is unavoidable to improve the isolating behaviour. As shown in chapter 1 the problems experienced cannot be solved with simple modifications to existing designs. The existing designs lack the right force-displacement behaviour and sufficient travel in compression ;

- When redesigning the Jockey Seat one should identify the worst case loads and design for them accordingly. These load have been identified in previous research and used in this thesis for the design of the Sigma seat prototype [2];

- A composite redesign based on the CLS jockey seats has been identified in this thesis as the best possibility for a final design that can cope with the worst case scenario loads;

- The analytical model developed allows for efficient analysis of two design directions. The first design is the CLS Jockey seat and the second one is a C-shaped design on which the Sigma seat prototype has been based. The model allows for variation of several variables like stiffness, dimensions and angle of the plates. The influence of these variables has been identified and used in the development of the prototype. Results have been compared with linear Finite Element models and are in agreement. The same FE-models have been used for non-linear analysis and results for the force-displacement behaviour are in agreement with the prototype;

- Dynamic behaviour of the redesigned Jockey Seat was simulated using a MatLab model. This model uses the non-linear force-displacement characteristic in combination with a mass-spring-damper model. The results correspond well with existing data, but anomalies like hitting the lower and upper support are harder to accurately model;

- Results of the dynamic model can be further improved by using a representative Repeated Shocks measured on the craft on which the Jockey Seats will be used. These shock can be measured during sea trials or by hoisting the craft up and dropping it into the water. Previous research suggests approximating the shock with a sine input pulse. If this method is used in the dynamic models more accurate results are obtained when the pulse starts with an acceleration of 0 m/s^2 and ends at 9.81 m/s^2. This is physically in agreement with a craft falling down and striking the water;

- The dynamic model also allows for testing the influence of many variables. These include occupant mass, seat damping, pulse time and maximum amplitude of the repeated shock. Furthermore, it allows for the use of custom non-linear force-displacement curves;

- The produced prototypes yield satisfying performance, isolating the Repeated Shocks better and thus outperforming any available commercial model.

6.2 Recommendations

Based on this thesis the follow recommendations for improvement and future research are suggested:

- As requested several design tools and models have been developed. TNO is recommended to use the tools described in this thesis to further improve the suggested designs;

- Only accelerations and forces in the vertical plane have been accounted for in this thesis. It is recommended to further research the influence of moments and horizontal accelerations on the construction to ensure good performance of future designs;

- It is recommended to perform further research into the effects of Repeated Shocks on occupants so thresholds can be defined for both short-term and long-term exposure. Until then users of Fast Planning Crafts are advised to undergo regular medical check-ups given the accelerations observed in testing of current jockey seats;

- Develop a custom damper for the prototype to further improve its performance. The damping coefficient should be around 25% of the critical damping coefficient and therefore the damping should be adjustable to adapt to different occupant weights;

- A standardized testing platform should be developed which accurately resembles the FRISC. This way, more prototypes can be testing and theoretical calculations made in this thesis and/or by TNO can be validated faster. A pontoon with a similar shape or FRISC frame outfitted with sensors should be produced for this purpose.

References

[1] TNO Netherlands. Frisc test run raport. *TNO*, 2015.

[2] T. E. Coe et all. Development of an international standard for comparing shock mitigating boat seat performance. *Innovation in Small Craft Technology*, 2016.

[3] Army motors. http://www.flmvpa.org/articles/armymotors_gill.htm. Accessed: 2010-10-18.

[4] Mitcalc spring calculation. http://http://www.mitcalc.com/doc/springs/help/en/springs.htm. Accessed: 2017-03-06.

[5] C. Liam. Testing and modeling of shock mitigating seats for high speed craft. Master's thesis, Virginia Polytechnic, 2006.

[6] Wave spring. http://www.tfc.eu.com/files/images/568x326/Spring_Comparator_15_1843x964.jpg. Accessed: 2010-10-18.

[7] D. M. Correa et all. Negative stiffness honeycombs for recoverable shock isolation. *The University of Texas at Austin*, 2014.

[8] Extract from Part 19 Commission Decision C(2014)4995. HORIZON 2020 âĂŞ WORK PROGRAMME 2014-2015 General Annexes. Technology readiness levels (trl). Technical report, European Commission, 2014.

[9] LTZ3(TD) S. Vredeveldt. Analyse van de huidige schokdempende stoelen op de friscs. B.s. thesis, Faculty of Military Sciences Netherlands, March 2016.

[10] H. Verschuren. *Designing a research project*. Boom Lemma Uitgevers, 2010.

[11] S. Myers et all. Effectiveness of suspension seats in maintaining performance following military high-speed boat transits. *Human Factors*, pages 264–276, September 2012.

[12] Koninklijke Landmacht. Beproevingsrapport trillingsmetingen frisc en boston whaler. *DMI*, 2014.

[13] R. Riley et all. Acceleration response mode decomposition for quantifying wave impact load in high speed planing craft. *Naval Surface Warfare Center*, Apr. 2014.

[14] KPM Marine. S2j scotseat, 2017.

[15] Anil K. Chopra. *Dynamics of structures*. Pearson Global, 2015.

[16] M. Aitken. Design and manufacture of leaf springs. *SAE Technical Papers*, 1993.

[17] S. Krall and R. Zemann. Investigation of the dynamic behaviour of cfrp leaf springs. *Procedia Engineering*, 100:646–655, 2015.

[18] M. Shokrieh and D. Rezaei. Analysis and optimization of a composite leaf spring. *Composite Structures*, 60(3):317–325, May 2003.

[19] S. Rajesh et al. Performance of leaf springs made of composite material subjected to low frequency impact loading. *Journal of Mechanical Science and Technology*, 30(9):4291–4298, May 2016.

[20] T. Loganathan et al. Significance of cyclic loading parameters on the flexural response of the gfrp composites. *Journal of Mechanical Science and Technology*, 30(7):3127–3136, March 2016.

[21] T. Loganathan et al. Investigation on flexural response of gfrp composite laminate subjected to low velocity cyclic loading. *Indian Journal of Science and Technology*, 8(15), July 2015.

[22] C. Subramanian and S. Senthilvelan. Effect of reinforced fiber length on the joint performance of thermoplastic leaf spring. *Materials & Design*, 31(8):3733–3741, September 2010.

[23] C. Subramanian and S. Senthilvelan. Joint performance of the glass fiber reinforced polypropylene leaf spring. *Composite Structures*, 93(2):759–766, January 2011.

[24] Y. Prawoto et al. Design and failure modes of automotive suspension springs. *Engineering Failure Analysis*, 15(8):1155–1174, December 2008.

[25] P. Pavani et al. Design, modeling and structural analysis of wave springs. *Procedia Materials Science*, 6:988–995, 2014.

[26] H. Erfanian-Naziftoosi et al. Composite wave springs: Theory and design. *Materials & Design*, 95:48–53, April 2016.

[27] E. Mahdi and A. Hamouda. An experimental investigation into mechanical behaviour of hybrid and non-hybrid composite semi-elliptical springs. *Materials & Design*, 52:504–513, December 2013.

[28] A. Talib et al. Developing a composite based elliptic spring for automotive applications. *Materials & Design*, 31(1):475–484, January 2010.

[29] E. Mahdi et al. Light composite elliptic springs for vehicle suspension. *Composite Structures*, 75(1-4):24–28, September 2006.

[30] R. Lakes. High damping composite materials: Effect of structural hierarchy. *Composite Materials*, 36(3), March 2001.

[31] D. Chung. Structural composite materials tailored for damping. *Journal of Alloys and Compounds*, 355(1-2):216–223, June 2003.

[32] S. Ashworth et al. Mechanical and damping properties of resin transfer moulded jute-carbon hybrid composites. *Composites Part B: Engineering*, 105:60–66, August 2016.

[33] M. Segiet and D. Chung. Discontinuous surface-treated submicron-diameter carbon filaments as an interlaminar filler in carbon fiber polymer-matrix composites for vibration reduction. *Composite Interfaces*, 7(4):257–275, 2000.

[34] J. Madeira et al. Multiobjective design of viscoelastic laminated composite sandwich panels. *Composites Part B: Engineering*, 77:391–401, 2015.

[35] E. Zheng T. Marquardt. History of 3d printing.

[36] R.C. Hibbeler. *Mechanics of Materials*. Pearson, 8th edition, 2011.

[37] Isaac M. Daniel and Ori Ishai. *Engineering Mechanics of Composite Materials, 2nd edition*. Oxford University Press, 2006.

[38] E. Riks. An incremental approach to the solution to the solution of buckling and snapping problems. *Int. J. Solids Struct.*, 15:524–551, 1979.

Appendix A

Test setup TNO drop tower

Figures A.1 and A.2 shows the test setup used by TNO to test jockey seats. This rig consists of two steel columns which guide a drop weight of $1000kg$. The jockey seats are mounted to drop weight with a bolted connection. Occupant weight is simulated by strapping lead weights to the seats. The test setup is fitted with several accelerometers to gather relevant data.

Figure A.1: TNO Netherlands drop tower

Figure A.2: Drop tower close-up

Appendix B

Mass-spring-damper calculation model

To study the response to the earlier presented load cases a simple but effective mass-spring-damper model has been constructed. The model is based on Newton's equations of motion with base excitation and is expressed in equation B.1.

$$m\frac{d^2x}{dt^2} = -k(x - x_b) - \lambda(\frac{dx}{dt} - \frac{dx_b}{dt}) \tag{B.1}$$

and:

$$\omega_n = \sqrt{\frac{k}{m}} \tag{B.2}$$

$$\zeta = \frac{\lambda}{2\sqrt{km}} \tag{B.3}$$

As can be seen in equation B.1 the system has a base excitation. This agrees with the behaviour one can expect for a craft slamming on the water. x_b is the displacement of the base of the boat. k is used to express the spring stiffness, λ is used for the damping coëfficient. In expression B.2 and B.3 ω_n is used for the natural frequency and ζ is the damping ratio.

x_b is derived from the prescribed acceleration pulse for the base that is used as the input pulse and can be seen in figure 1.5. An example of the seat response is shown in figure B.1. The model's behaviour has been validated through comparision with earlier mentioned literature and is in agreement.

The numerical integration in the MatLab is performed according to the Midpoint method, also called Modified Euler method. It is a first order method for numerical integration. Therefore, the equations of motion for the mass-spring-damper system are split into two first order systems:

$$\frac{dv}{dt} = -\frac{k}{m}(x - x_b) - \frac{\lambda}{m}(v - v_b) \tag{B.4}$$

$$\frac{dx}{dt} = v \tag{B.5}$$

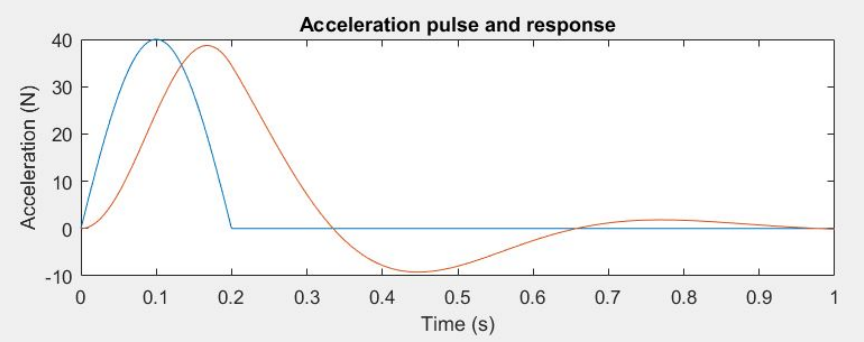

Figure B.1: Example of seat response to excitation pulse

With the Midpoint method we now first apply Euler's method halfway across the interval, which is defined by the step size. The derivatives are recomputed and the values of the estimated midpoint derivatives are then used to calculate the values belonging to the new step. This method is mathematically expressed as follows:

$$y_{N+1/2} = y_N + \frac{\Delta t}{2} \left.\frac{dy}{dt}\right|_N \tag{B.6}$$

$$y_{N+1} = y_N + \Delta t \left.\frac{dy}{dt}\right|_{N+1/2} \tag{B.7}$$

And is implemented in the following order:

$$\begin{aligned} u_1 &= 0 \\ v_1 &= 0 \\ a_1 &= -\frac{\lambda}{m}(v_1 - v_{b1}) - \frac{k}{m}(u_1 - u_{b_1}) \end{aligned} \tag{B.8}$$

After the initial conditions are set the midpoint values are calculated:

$$\begin{aligned} u_{1\frac{1}{2}} &= u_1 + \frac{\Delta t}{2} v_1 \\ v_{1\frac{1}{2}} &= v_1 + \frac{\Delta t}{2} a_1 \\ a_{1\frac{1}{2}} &= -\frac{\lambda}{m}(v_{1\frac{1}{2}} - v_{b1\frac{1}{2}}) - \frac{k}{m}(u_{1\frac{1}{2}} - u_{b1\frac{1}{2}}) \end{aligned} \tag{B.9}$$

Lastly, the values for the second step are calculated:

$$\begin{aligned} u_2 &= u_1 + v_{1\frac{1}{2}} \Delta t \\ v_2 &= v_1 + a_{1\frac{1}{2}} \Delta t \\ a_2 &= -\frac{\lambda}{m}(v_2 - v_{b2}) - \frac{k}{m}(u_2 - u_{b2}) \end{aligned} \tag{B.10}$$

These steps are repeated until the desired number of steps have been calculated. The relative error of the Midpoint method to the exact solution is of the order Δt^2.

This model is used in this thesis to analyse the response of several designs. It is referred to in section 1.2.

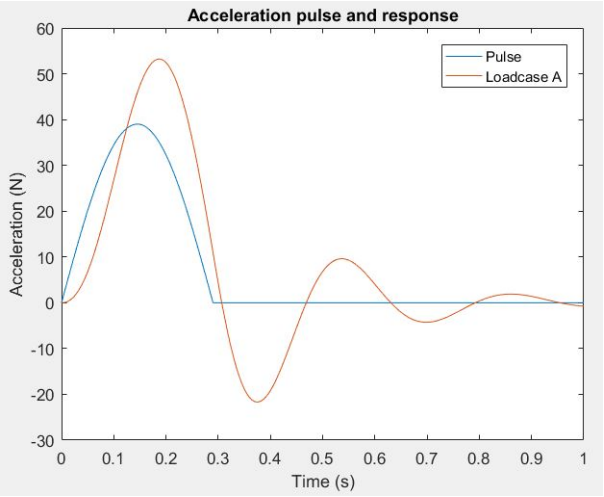

Figure B.2: Response for loadcase A

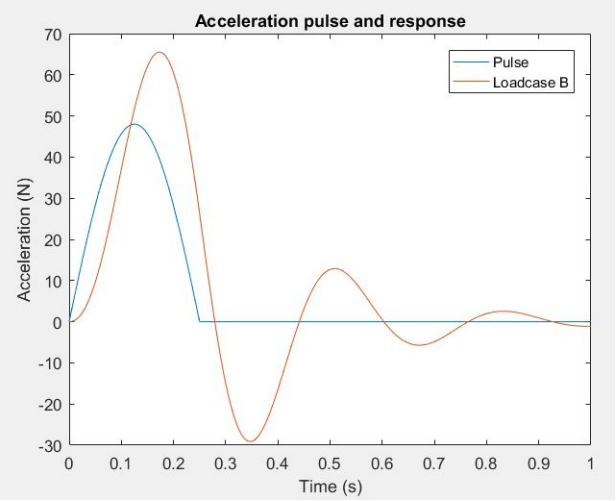

Figure B.3: Response for loadcase B

Technology Readiness Level table

In table B.1 the Technology Readiness Levels are shown. These levels indicate the maturity of a technology by differentiating in levels from 1, in which basic scientic principles are observed, through 9, an actual 'flight-proven system'.

TRL	Description
1	basic principles observed
2	technology concept formulated
3	experimental proof of concept
4	technology validated in lab
5	technology validated in relevant environment
6	technology demonstrated in relevant environment
7	system prototype demonstration in operational environment
8	system complete and qualified
9	actual system proven in operational environment

Table B.1: Technology Readiness Levels according to the European Comission [8]

Appendix C

Analytical Derivations

In this appendix parts of the analytical derivations for the C-shaped design of chapter 3 can be found.

Derivation for C-shaped design

In figure C.1 the statically determined construction is shown. This is achieved by introducing two cuts. One at beam CD and another one for beam EF. It is now impossible for these beams to transfer any loads. The FBD are shown in figure C.2 and figure C.3. These result in the following equations for the FBD's of the four beams:

Equilibrium equations for beam AB:

$$\begin{aligned} N^0(\xi) &= H_L \cos(\alpha) + V_L \sin(\alpha) \\ V^0(\xi) &= H_L \sin(\alpha) - V_L \cos(\alpha) \\ M^0(\xi) &= H_L \left((a-\xi)\sin(\alpha) - \frac{1}{2}h \right) - V_L(a-\xi)\cos(\alpha) - M_L \end{aligned} \tag{C.1}$$

Equilibrium equations for beam CD:

$$\begin{aligned} N^0(\mu) &= 0 \\ V^0(\mu) &= 0 \\ M^0(\mu) &= 0 \end{aligned} \tag{C.2}$$

Equilibrium equations for beam EF:

$$\begin{aligned} N^0(\phi) &= 0 \\ V^0(\phi) &= 0 \\ M^0(\phi) &= 0 \end{aligned} \tag{C.3}$$

Equilibruim equations for beam GH

$$\begin{aligned} N^0(\chi) &= -H_L \cos(\alpha) + V_L \sin(\alpha) \\ V^0(\chi) &= -H_L \sin(\alpha) - V_L \cos(\alpha) \\ M^0(\chi) &= H_L \left(\frac{3}{2}h + b + a\sin(\alpha) + \chi \sin(\alpha)\right) - V_L \left((a-\chi)\cos(\alpha)\right) - M_L \end{aligned} \tag{C.4}$$

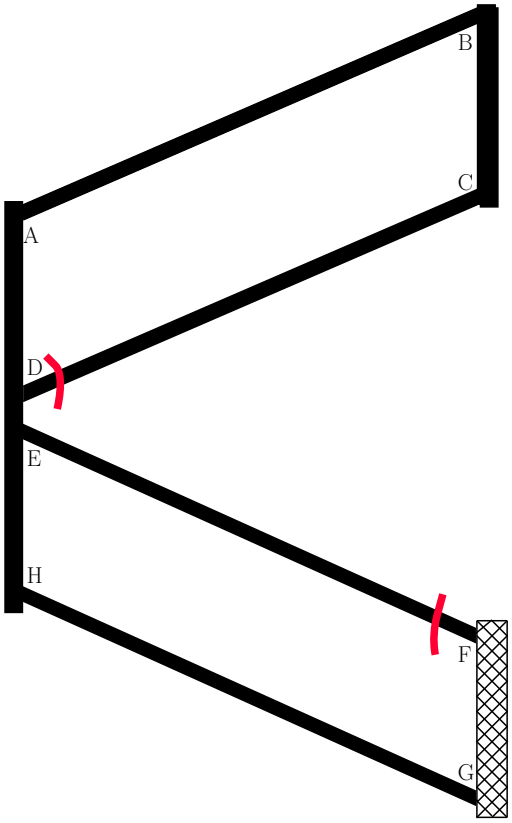

Figure C.1: Statically determined construction

We now continue with the internally indeterminate system. The system is shown in figure C.4 and the resulting FBD's are shown in figures C.5 and C.6. The resulting equations are:

Equilibrium equations for beam AB:

$$\begin{aligned} N^1(\xi) &= H_D \cos(\alpha) + V_D \sin(\alpha) \\ V^1(\xi) &= H_D \sin(\alpha) - V_D \cos(\alpha) \\ M^1(\xi) &= -H_D \left(h + a\sin(\alpha) - (\alpha - \xi)\sin(\alpha)\right) + V_D \left(a\cos(\alpha) - (a-\xi)\cos(\alpha)\right) - M_D \end{aligned} \tag{C.5}$$

Equilibrium equations for beam CD:

$$\begin{aligned} N^1(\mu) &= -H_D \cos(\alpha) - V_D \sin(\alpha) \\ V^1(\mu) &= H_D \sin(\alpha) - V_D \cos(\alpha) \\ M^1(\mu) &= -H_D \mu \sin(\alpha) + V_D \mu \cos(\alpha) - M_D \end{aligned} \tag{C.6}$$

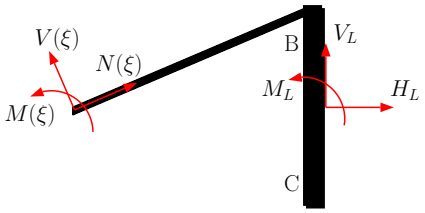

Figure C.2: Free Body Diagram IV

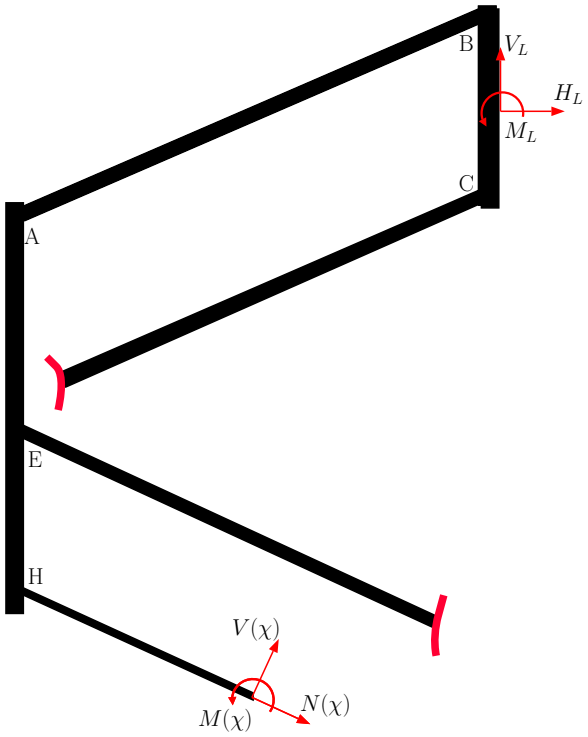

Figure C.3: Free Body Diagram V

Equilibrium equations for beam EF:

$$\begin{aligned} N^1(\phi) &= 0 \\ V^1(\phi) &= 0 \\ M^1(\phi) &= 0 \end{aligned} \tag{C.7}$$

Equilibrium equations for beam GH:

$$\begin{aligned} N^1(\chi) &= 0 \\ V^1(\chi) &= 0 \\ M^1(\chi) &= 0 \end{aligned} \tag{C.8}$$

We now continue with the statically indeterminate clamp at point F as can be seen in figure C.7. The FBD's for beam EF and GH can be seen in figures C.8 and C.9. This results in the following FBD equilibrium equations:

Equilibrium equations for beam AB:

$$\begin{aligned} N^2(\xi) &= 0 \\ V^2(\xi) &= 0 \\ M^2(\xi) &= 0 \end{aligned} \tag{C.9}$$

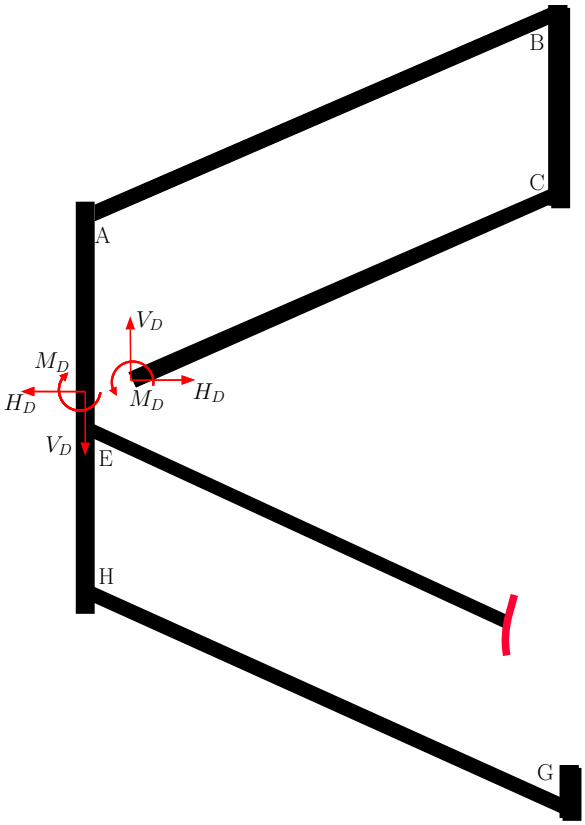

Figure C.4: Internally determinate construction

Equilibrium equations for beam CD:

$$\begin{aligned} N^2(\mu) &= 0 \\ V^2(\mu) &= 0 \\ M^2(\mu) &= 0 \end{aligned} \tag{C.10}$$

Equilibrium equations for beam EF:

$$\begin{aligned} N^2(\phi) &= H_F \cos(\alpha) - V_F \sin(\alpha) \\ V^2(\phi) &= -H_F \sin(\alpha) - V_F \cos(\alpha) \\ M^2(\phi) &= -H_F(a-\phi)\sin(\alpha) - V_F(a-\phi)\cos(\alpha) - M_F \end{aligned} \tag{C.11}$$

Equilibrium equations for beam GH

$$\begin{aligned} N^2(\chi) &= -H_F \cos(\alpha) + V_F \sin(\alpha) \\ V^2(\chi) &= -H_F \sin(\alpha) - V_F \cos(\alpha) \\ M^2(\chi) &= H_F\left(h - a\sin(\alpha) + \chi\sin(\alpha)\right) - V_F\left(a\cos(\alpha) - \chi\cos(\alpha)\right) - M_F \end{aligned} \tag{C.12}$$

Through superposition of the three described systems the final equilibrium equations for the design are obtained.

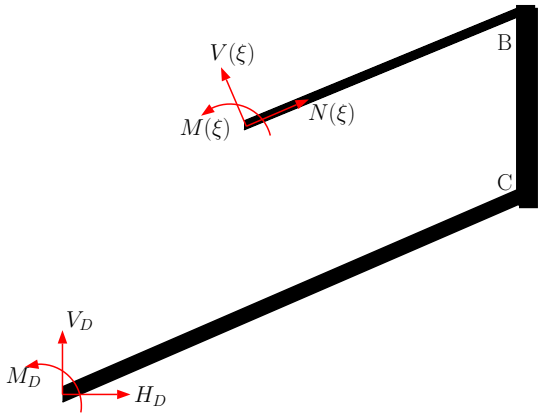

Figure C.5: Free Body Diagram VI

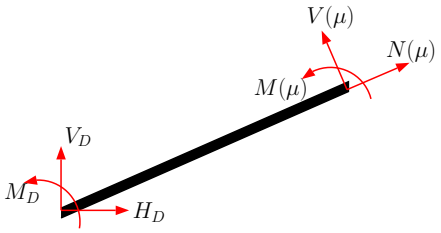

Figure C.6: Free Body Diagram VII

Equilibrium equations for beam AB:

$$\begin{aligned} N(\xi) &= H_L\cos(\alpha) + V_L\sin(\alpha) + H_D\cos(\alpha) + V_D\sin(\alpha) \\ M(\xi) &= H_L\left((a-\xi)\sin(\alpha) - \frac{1}{2}h\right) - V_L(a-\xi)\cos(\alpha) - M_L \\ &\quad - H_D\left(h + a\sin(\alpha) - (a-\xi)\sin(\alpha)\right) \\ &\quad + V_D\left(a\cos(\alpha) - (a-\xi)\cos(\alpha)\right) - M_D \end{aligned} \tag{C.13}$$

Equilibrium equatinos for beam CD:

$$\begin{aligned} N(\mu) &= -H_D\cos(\alpha) - V_D\sin(\alpha) \\ M(\mu) &= -H_D\mu\sin(\alpha) + V_D\mu\cos(\alpha) - M_D \end{aligned} \tag{C.14}$$

Equilibrium equations for beam EF:

$$\begin{aligned} N(\phi) &= H_F\cos(\alpha) - V_F\sin(\alpha) \\ M(\phi) &= -H_F(a-\phi)\sin(\alpha) - V_F(a-\phi)\cos(\alpha) - M_F \end{aligned} \tag{C.15}$$

Equilibrium equations for beam GH:

$$\begin{aligned} N(\chi) &= -H_L\cos(\alpha) + V_L\sin(\alpha) - H_F\cos(\alpha) + V_F\sin(\alpha) \\ M(\chi) &= H_L\left(\frac{3}{2}h + b + a\sin(\alpha) + \chi\sin(\alpha)\right) - V_L\left((a-\chi)\cos(\alpha)\right) \\ &\quad - M_L + M_F\left(h - a\sin(\alpha) + \chi\sin(\alpha)\right) - V_F\left(a\cos(\alpha) - \chi\cos(\alpha)\right) - M_F \end{aligned} \tag{C.16}$$

The strain energy U is now given by:

$$\begin{aligned} U = &\frac{1}{2}\int_{\xi=0}^{a}\left(\frac{N(\xi)^2}{E_mA} + \frac{M(\xi)^2}{E_bI}\right)d\xi + \frac{1}{2}\int_{\mu=0}^{a}\left(\frac{N(\mu)^2}{E_mA} + \frac{M(\mu)^2}{E_bI}\right)d\mu \\ &+ \frac{1}{2}\int_{\phi=0}^{a}\left(\frac{N(\phi)^2}{E_mA} + \frac{M(\phi)^2}{E_bI}\right)d\phi + \frac{1}{2}\int_{\chi=0}^{a}\left(\frac{N(\chi)^2}{E_mA} + \frac{M(\chi)^2}{E_bI}\right)d\chi \end{aligned} \tag{C.17}$$

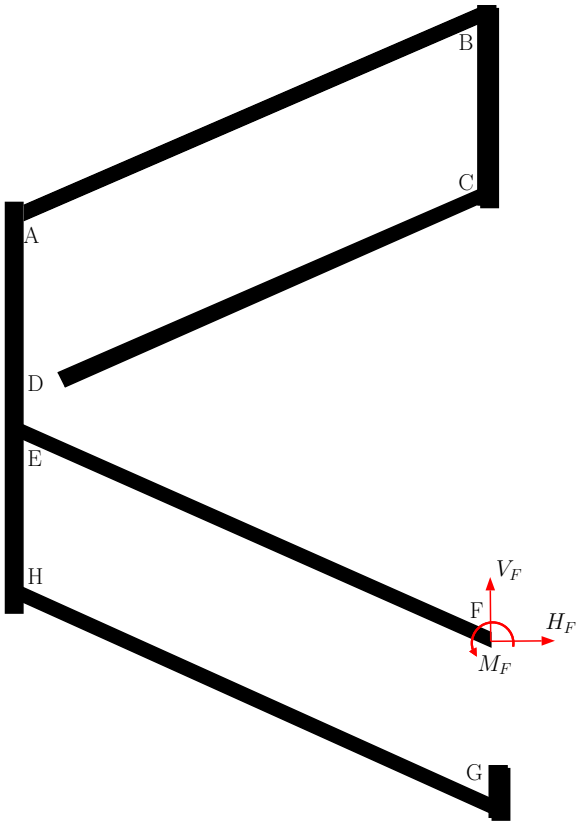

Figure C.7: Statically indeterminate clamp point F

This expression is used together with the boundary conditions for the six unknowns:

$$\begin{array}{lll} \dfrac{\partial U}{\partial H_D} = 0 & \dfrac{\partial U}{\partial V_D} = 0 & \dfrac{\partial U}{\partial M_D} = 0 \\ \dfrac{\partial U}{\partial H_F} = 0 & \dfrac{\partial U}{\partial V_F} = 0 & \dfrac{\partial U}{\partial M_F} = 0 \end{array} \tag{C.18}$$

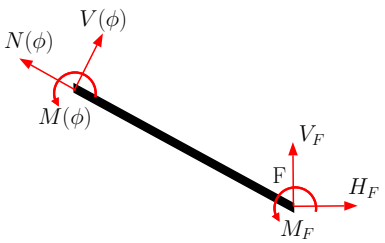

Figure C.8: Free body diagram VIII

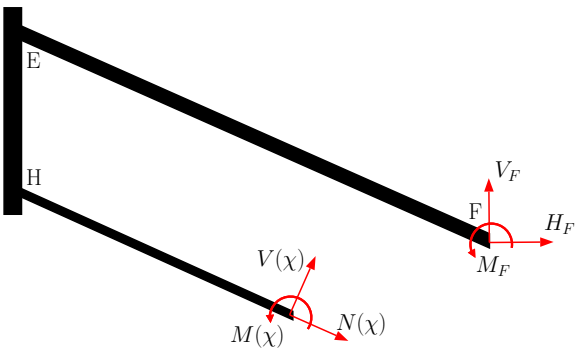

Figure C.9: Free body diagram IIX

Partial derivatives C-shaped design

$$\begin{aligned}\frac{\partial U}{\partial H_D} = &\underbrace{\left(\frac{2}{3}\frac{a^3\sin^2(\alpha)}{EI} + \frac{a^2 h\sin(\alpha)}{EI} + \frac{ah^2}{EI} + \frac{2\cos^2(\alpha)a}{EA}\right)}_{\text{A11}} H_D \\ &+ \underbrace{\left(-\frac{2}{3}\frac{a^3\cos(\alpha)\sin(\alpha)}{EI} - \frac{1}{2}\frac{a^2 h\cos(\alpha)}{EI} + \frac{2a\cos(\alpha)\sin(\alpha)}{EA}\right)}_{\text{A12}} V_D \\ &+ \underbrace{\left(\frac{a^2\sin(\alpha)+ah}{EI}\right)}_{\text{A13}} M_D \\ &+ \underbrace{\left(\frac{1}{3}\frac{a^3\sin^2(\alpha)}{EI} + \frac{1}{2}\frac{a^2 h\sin(\alpha)}{EI}\right.}_{B11} \\ &\underbrace{\left. -\frac{1}{2}\frac{(a\sin(\alpha)-\frac{1}{2}h)\sin(\alpha)a^2}{EI} - \frac{(a\sin(\alpha)-\frac{1}{2}h)ah}{EI} + \frac{a\cos^2(\alpha)}{EA}\right)}_{B11} H_L \\ &+ \underbrace{\left(\frac{1}{6}\frac{a^3\cos(\alpha)\sin(\alpha)}{EI} + \frac{1}{2}\frac{a^2 h\cos(\alpha)}{EI} + \frac{a\cos(\alpha)\sin(\alpha)}{EA}\right)}_{\text{B12}} V_L \\ &+ \underbrace{\left(\frac{1}{2}\frac{a^2\sin(\alpha)+ah}{EI}\right)}_{\text{B13}} M_L\end{aligned} \tag{C.19}$$

$$\begin{aligned}\frac{\partial U}{\partial V_D} = &\underbrace{\left(-\frac{2}{3}\frac{a^3\cos(\alpha)\sin(\alpha)}{EI} - \frac{1}{2}\frac{ha^2\cos(\alpha)}{EI} + \frac{2a\cos(\alpha)\sin(\alpha)}{EA}\right)}_{\text{A21}} H_D \\ &+ \underbrace{\left(\frac{2}{3}\frac{a^3\cos^2(\alpha)}{EI} + \frac{2a\sin^2(\alpha)}{EA}\right)}_{\text{A22}} V_D \\ &\underbrace{\left(-\frac{a^2\cos(\alpha)}{EI}\right)}_{A23} M_D \\ &\underbrace{\left(-\frac{1}{3}\frac{a^3\cos(\alpha)\sin(\alpha)}{EI} + \frac{1}{2}\frac{(a\sin(\alpha)-\frac{1}{2}h)a^2\cos(\alpha)}{EI} + \frac{a\cos(\alpha)\sin(\alpha)}{EA}\right)}_{B21} H_L \\ &\underbrace{\left(-\frac{1}{6}\frac{a^3\cos^2(\alpha)}{EI} + \frac{a\sin^2(\alpha)}{EA}\right)}_{B22} V_L \\ &\underbrace{\left(-\frac{1}{2}\frac{a^2\cos(\alpha)}{EI}\right)}_{B23} M_L\end{aligned} \tag{C.20}$$

$$
\begin{aligned}
\frac{\partial U}{\partial M_D} = & \underbrace{\left(\frac{a^2\sin(\alpha)+ah}{EI}\right)}_{A31} H_D \\
& - \underbrace{\left(\frac{a^2\cos(\alpha)}{EI}\right)}_{A32} V_D \\
& + \underbrace{\left(\frac{2a}{EI}\right)}_{A33} M_D \\
& + \underbrace{\left(\frac{1}{2}\frac{a^2\sin(\alpha)}{EI} - \frac{(a\sin(\alpha)-\frac{1}{2}h)a}{EI}\right)}_{B31} H_L \\
& + \underbrace{\left(\frac{1}{2}\frac{a^2\cos(\alpha)}{EI}\right)}_{B32} H_L \\
& + \underbrace{(a)}_{B33} H_L
\end{aligned}
\tag{C.21}
$$

$$
\begin{aligned}
\frac{\partial U}{\partial H_F} = & \underbrace{\left(\frac{1}{3}\frac{a^3\sin^2(\alpha)}{EI} + \frac{2a\cos^2(\alpha)}{EA}\right)}_{\text{A44}} H_F \\
& + \underbrace{\left(\frac{1}{3}\frac{a^2\cos(\alpha)\sin(\alpha)}{EI} + \frac{2a\cos^2(\alpha)}{EA}\right)}_{\text{A45}} V_F \\
& + \underbrace{\left(\frac{1}{2}\frac{a^2\sin(\alpha)}{EI}\right)}_{\text{A46}} M_F \\
& + \underbrace{\left(\frac{a\cos^2(\alpha)}{EA}\right)}_{\text{B41}} H_L \\
& - \underbrace{\left(\frac{a\cos(\alpha)\sin(\alpha)}{EA}\right)}_{\text{B42}} V_L \\
& \underbrace{(0)}_{\text{B43}} M_L
\end{aligned}
\tag{C.22}
$$

$$\frac{\partial U}{\partial V_F} = \underbrace{\left(\frac{1}{3}\frac{a^3\cos(\alpha)\sin(\alpha)}{EI} - \frac{2a\cos(\alpha)\sin(\alpha)}{EA}\right)}_{\text{A54}} H_F$$
$$+ \underbrace{\left(\frac{2}{3}\frac{a^3\cos^2(\alpha)}{EI} + \frac{2a\sin^2(\alpha)}{EA}\right)}_{\text{A55}} V_F$$
$$+ \underbrace{\left(\frac{1}{2}\frac{a^2\cos(\alpha)}{EI} - \frac{1}{6}\frac{a^3\cos(\alpha)\sin(\alpha)}{EI} - \frac{1}{2}\frac{(-a\sin(\alpha)+h-1)\cos(\alpha)a^2}{EI}\right)}_{\text{A56}} M_F$$
$$+ \underbrace{\left(-\frac{1}{6}\frac{a^3\cos(\alpha)\sin(\alpha)}{EI} - \frac{1}{2}\frac{(\frac{3}{2}h+b+a\sin(\alpha))\cos(\alpha)a^2}{EI} - \frac{a\cos(\alpha)\sin(\alpha)}{EA}\right)}_{\text{B51}} H_L$$
$$+ \underbrace{\left(\frac{1}{3}\frac{a^3\cos^2(\alpha)}{EI} + \frac{a\sin^2(\alpha)}{EA}\right)}_{\text{B52}} V_L$$
$$+ \underbrace{\left(\frac{1}{2}\frac{a^2\cos(\alpha)}{EI}\right)}_{\text{B53}} M_L \tag{C.23}$$

$$
\begin{aligned}
\frac{\partial U}{\partial M_F} = & \underbrace{\left(\frac{1}{2}\frac{a^2\sin(\alpha)}{EI}\right)}_{\text{A64}} H_F \\
& + \underbrace{\left(\frac{1}{2}\frac{a^2\cos(\alpha)}{EI} - \frac{1}{6}\frac{a^3\cos(\alpha)\sin(\alpha)}{EI} - \frac{1}{2}\frac{(-a\sin(\alpha)+h-1)\cos(\alpha)a^2}{EI}\right)}_{\text{A65}} V_F \\
& + \underbrace{\left(\frac{a}{EI} + \frac{1}{3}\frac{a^3\sin^2(\alpha)}{EI} + \frac{(-a\sin(\alpha)+h-1)\sin(\alpha)a^2}{EI} + \frac{(-a\sin(\alpha)+h-1)^2 a}{EI}\right)}_{\text{A66}} M_F \\
& + \underbrace{\left(\frac{1}{3}\frac{a^3\sin^2(\alpha)}{EI} + \frac{1}{2}\frac{(-a\sin(\alpha)+h-1)\sin(\alpha)a^2}{EI}\right.}_{B61} \\
& \quad \underbrace{\left. + \frac{1}{2}\frac{(\frac{3}{2}h+b+a\sin(\alpha))\sin(\alpha)a^2}{EI} + \frac{(\frac{3}{2}h+b+a\sin(\alpha))a(-a\sin(\alpha)+h-1)}{EI}\right)}_{B61} H_L \\
& + \underbrace{\left(-\frac{1}{6}\frac{a^3\cos(\alpha)\sin(\alpha)}{EI} - \frac{1}{2}\frac{(-a\sin(\alpha)+h-1)\cos(\alpha)a^2}{EI}\right)}_{\text{B62}} V_L \\
& + \underbrace{\left(-\frac{1}{2}\frac{a^2\sin(\alpha)}{EI} - \frac{(-a\sin(\alpha)+h-1)a}{EI}\right)}_{\text{B63}} M_L
\end{aligned}
\tag{C.24}
$$

Solving the system of equations

Determining the partial derivatives gives the following result:

$$
\begin{bmatrix}A\end{bmatrix}\begin{pmatrix}H_D\\V_D\\M_D\\H_F\\V_F\\M_F\end{pmatrix} + \begin{bmatrix}B_{11} & B_{12} & B_{13}\\ B_{21} & B_{22} & B_{23}\\ B_{31} & B_{32} & B_{33}\\ B_{41} & B_{42} & B_{43}\\ B_{51} & B_{52} & B_{53}\\ B_{61} & B_{62} & B_{63}\end{bmatrix}\begin{pmatrix}H_L\\V_L\\M_L\end{pmatrix} = \begin{pmatrix}\frac{\partial U}{\partial H_D}\\ \frac{\partial U}{\partial V_D}\\ \frac{\partial U}{\partial M_D}\\ \frac{\partial U}{\partial H_F}\\ \frac{\partial U}{\partial V_F}\\ \frac{\partial U}{\partial M_F}\end{pmatrix} = \begin{pmatrix}0\\0\\0\\0\\0\\0\end{pmatrix} \tag{C.25}
$$

with:

$$
[A] = \begin{bmatrix}A_{11} & A_{12} & A_{13} & A_{14} & A_{15} & A_{16}\\ A_{21} & A_{22} & A_{23} & A_{24} & A_{25} & A_{26}\\ A_{31} & A_{32} & A_{33} & A_{34} & A_{35} & A_{36}\\ A_{41} & A_{42} & A_{43} & A_{44} & A_{45} & A_{46}\\ A_{51} & A_{52} & A_{53} & A_{54} & A_{55} & A_{56}\\ A_{61} & A_{62} & A_{63} & A_{64} & A_{65} & A_{66}\end{bmatrix} \tag{C.26}
$$

and:

$$[B] = \begin{bmatrix} B_{11} & B_{12} & B_{13} \\ B_{21} & B_{22} & B_{23} \\ B_{31} & B_{32} & B_{33} \\ B_{41} & B_{42} & B_{43} \\ B_{51} & B_{52} & B_{53} \\ B_{61} & B_{62} & B_{63} \end{bmatrix} \tag{C.27}$$

This is rearranged giving:

$$\begin{pmatrix} H_D \\ V_D \\ M_D \\ H_F \\ V_F \\ M_F \end{pmatrix} = -[A^{-1}][B] \begin{pmatrix} H_L \\ V_L \\ M_L \end{pmatrix} = [C] \begin{pmatrix} H_L \\ V_L \\ M_L \end{pmatrix} \tag{C.28}$$

Now the displacement of point L under influence of the loads H_L,V_L and M_L can be determined. The strain energy is given by:

$$\begin{aligned} U = &\int_0^a \left(\frac{N(\xi)^2}{E_m A} + \frac{M(\xi)^2}{E_b I} \right) d\xi + \int_0^a \left(\frac{N(\mu)^2}{E_m A} + \frac{M(\mu)^2}{E_b I} \right) d\mu \\ &+ \int_0^a \left(\frac{N(\phi)^2}{E_m A} + \frac{M(\phi)^2}{E_b I} \right) d\phi + \int_0^a \left(\frac{N(\chi)^2}{E_m A} + \frac{M(\chi)^2}{E_b I} \right) d\chi \end{aligned} \tag{C.29}$$

And the displacement of point L is given by:

$$\begin{aligned} u_L &= \frac{\partial U}{H_L} \\ v_L &= \frac{\partial U}{V_L} \\ \phi_L &= \frac{\partial U}{M_L} \end{aligned} \tag{C.30}$$

Appendix D

Matlab

In this appendix the MatLab files used for the dynamic model are shown.

MainProgram.m

```
% master program

clc
clear all
close all

Mass = 100;

%input pulse

Apulse = 40;
Tpulse = 0.2;
dT = 0.001;
time = 1;
Fpulse = 1/(2*Tpulse);
%-------------------------------------------------------------------------
% Spring characteristic constants

        %Spring characteristic 1
U1 = xlsread('SpringC.xlsx',1,'A3:A22');
F1 = xlsread('SpringC.xlsx',1,'B3:B22');
U1 = U1.';
F1 = F1.';

        %Spring characteristic 2
U2 = xlsread('SpringC.xlsx',1,'D3:D25');
F2 = xlsread('SpringC.xlsx',1,'E3:E25');
U2 = U2.';
F2 = F2.';
        %Spring characteristic 3
U3 = xlsread('SpringC.xlsx',1,'G3:G25');
F3 = xlsread('SpringC.xlsx',1,'H3:H25');
```

```
33 U3 = U3.';
34 F3 = F3.';
35
36 % Damping constants for compression and extension
37
38 Ccom = 1000;
39 Cext = 1000;
40
41 % Main Function
42
43 [ddte,dte,ue,t,ddt,dt,u,Uspring,Fspring,IF]              = ...
       MainFunction(Apulse,Tpulse,dT,time,Mass,Ccom,Cext,U1,F1);
44 [ddte2,dte2,ue2,t2,ddt2,dt2,u2,Uspring2,Fspring2,IF2 ]   = ...
       MainFunction(Apulse,Tpulse,dT,time,Mass,Ccom,Cext,U2,F2);
45 [ddte3,dte3,ue3,t3,ddt3,dt3,u3,Uspring3,Fspring3,IF3 ]   = ...
       MainFunction(Apulse,Tpulse,dT,time,Mass,Ccom,Cext,U3,F3);
46
47 % Print of characteristic used
48
49 Uused = min(ue-u):0.001:max(ue-u);
50 Fused = interp1(U1,F1,Uused,'linear','extrap');
51 U2used = min(ue2-u2):0.001:max(ue2-u2);
52 F2used = interp1(U2,F2,U2used,'linear','extrap');
53 U3used = min(ue3-u3):0.001:max(ue3-u3);
54 F3used = interp1(U3,F3,U3used,'linear','extrap');
55
56 % Plot of characteristics, response and compression in time
57
58 figure('units','normalized','outerposition',[0 0 1 1])
59 subplot(3,1,1)
60 hold on
61 plot(Uused,Fused)
62 % plot(U2used,F2used,U3used,F3used)
63 hold off
64 xlabel('Compression (m)')
65 ylabel('Force (N)')
66 axis([min([Uused,U2used,U3used]) max([Uused,U2used,U3used]) ...
       min([Fused,F2used,F3used]) max([Fused,F2used,F3used])])
67 ax.Box = 'off';
68 ax = gca;
69 ax.XAxisLocation = 'origin';
70 ax.YAxisLocation = 'origin';
71 title('Spring characteristic')
72
73 subplot(3,1,2)
74 plot(t,ddte,t,ddt)
75 % plot(t,ddt2,t,ddt3)
76 xlabel('Time (s)')
77 ylabel('Acceleration (N)')
78 title('Acceleration pulse and response')
79 legend('Puls','Prod1','Prod2','Prod3')
80
81 subplot(3,1,3)
82 plot(t,ue-u)
83 % plot(t,ue2-u2,t,ue3-u3)
84 xlabel('Time (s)')
85 ylabel('Compression (N)')
86 title('Compression in time')
87 legend('Prod1','Prod2','Prod3')
88
89 f = figure(2);
```

```
t = uitable(f,'ColumnWidth',{120 60});
data = {'Spring stiffness','NaN';'Damping ratio','NaN';'Isolation ...
    Factor',IF;'Apulse',Apulse;'Maximum ...
    response',max(ddt);'Mass',Mass;'Damping compression,',Ccom;'Damping ...
    Extension',Cext; 'Pulse frequency',Fpulse;'Pulsetime',Tpulse};
t.Data = data;
t.ColumnName = {'Variable','Value'};

% Range experiment 1

ss = get(0,'screensize'); %The screen size
width = ss(3);
height = ss(4);
vert = 0.5*height; %300 vertical pixels
horz = 0.5*width; %600 horizontal pixels

for Mass=50:25:150

[ ddte,dte,ue,t,ddt,dt,u,Uspring,Fspring,IF ] = MainFunction( ...
    Apulse,Tpulse,dT,time,Mass,Ccom,Cext,U1,F1 );

    MassFigure = figure(3);
    hold on
    set(MassFigure,'OuterPosition',[width-horz, height-(vert+30), horz, vert]);
    plot(t,ddt)
    title('Mass variation')
    xlabel('Time (s)')
    ylabel('Acceleration (m/s^2)')
    str(Mass/25) = {strcat('Mass = ' , num2str(Mass))};
    legend(str{:})
    hold off

end

Mass=100;

for Tpulse=0.05:0.05:0.25

[ ddte,dte,ue,t,ddt,dt,u,Uspring,Fspring,IF ] = MainFunction( ...
    Apulse,Tpulse,dT,time,Mass,Ccom,Cext,U1,F1 );

    PulseFigure = figure(5);
    hold on
    set(PulseFigure,'OuterPosition',[0, 0, horz, vert]);
    plot(t,ddt)
    title('Pulse time variation')
    xlabel('Time (s)')
    ylabel('Acceleration (m/s^2)')
    str(round(Tpulse/0.05)) = {strcat('Pulse time = ' , num2str(Tpulse))};
    legend(str{:})
    hold off

end

Tpulse = 0.2;

for Ccom=500:250:1500

    Cext=Ccom;

```

```
[ ddte,dte,ue,t,ddt,dt,u,Uspring,Fspring,IF ] = MainFunction( ...
    Apulse,Tpulse,dT,time,Mass,Ccom,Cext,U1,F1 );

    DampingFigure = figure(6);
    hold on
    set(DampingFigure,'OuterPosition',[width-horz, 0, horz, vert]);
    plot(t,ddt)
    title('Damping variation')
    xlabel('Time (s)')
    ylabel('Acceleration (m/s^2)')
    str((Ccom-250)/250) = {strcat('Damping = ' , num2str(Ccom))};
    legend(str{:})
    hold off

end

Ccom=1000;
Cext=1000;

%-------------------------------------------------------------------------
StiffFigure = figure(4);
hold on
set(StiffFigure,'OuterPosition',[0, height-(vert+30), horz, vert]);
plot(t,ddt)
%plot(t2,ddt2)
%plot(t3,ddt3)
title('Stiffness variation')
xlabel('Time (s)')
ylabel('Acceleration (m/s^2)')
%str(b/4000) = {strcat('Stiffness = ' , num2str(b))};
%legend(str{:})
hold off
%-------------------------------------------------------
% Pretension investigation for prod1

%F1(1)=F1(1)+15;
F1(3:20)=F1(3:20)+500;
[ddte4,dte4,ue4,t4,ddt4,dt4,u4,Uspring4,Fspring4,IF4 ]  = ...
    MainFunction(Apulse,Tpulse,dT,time,Mass,Ccom,Cext,U1,F1);
U4used = min(ue4-u4):0.001:max(ue4-u4);
F4used = interp1(U1,F1,U4used,'linear','extrap');

%F1(1)=F1(1)+15;
F1(3:20)=F1(3:20)+500;
[ddte5,dte5,ue5,t5,ddt5,dt5,u5,Uspring5,Fspring5,IF5 ]  = ...
    MainFunction(Apulse,Tpulse,dT,time,Mass,Ccom,Cext,U1,F1);
U5used = min(ue5-u5):0.001:max(ue5-u5);
F5used = interp1(U1,F1,U5used,'linear','extrap');

figure(7)
plot(t,ddte,t,ddt,t,ddt4,t,ddt5)
xlabel('Time (s)')
ylabel('Acceleration (N)')
title('Acceleration pulse and response')
legend('Puls','Prod1','Prod1+500','Prod1+1000')

figure(8)
hold on
plot(Uused,Fused,U4used,F4used,U5used,F5used)
hold off
xlabel('Compression (m)')
```

```
ylabel('Force (N)')
axis([min([Uused,U4used,U5used]) max([Uused,U4used,U5used]) ...
    min([Fused,F4used,F5used]) max([Fused,F4used,F5used])])
ax.Box = 'off';
ax = gca;
ax.XAxisLocation = 'origin';
ax.YAxisLocation = 'origin';
title('Spring characteristic')
legend('prod1','prod1+500','prod1+1000')

% figure()
% plot(Uspring,ddt*Mass)
```

MainFunction.m

```
function [ ddte,dte,ue,t,ddt,dt,u,Uspring,Fspring,IF ] = MainFunction( ...
    Apulse,Tpulse,dT,time,Mass,Ccom,Cext,U1,F1 )
% This function contains the all calculation for the response calculation
% and makes use of several other functions. These are: InputPulse,
% FuncSpring and Seat
%

% Calculation of Input Pulse
[ddte,dte,ue,t] = InputPulse(Apulse,Tpulse,dT,time);

% Calculation of GLOBAL seat movement
[ddt,dt,u,Uspring,Fspring] = Seat(Mass,Ccom,Cext,t,dte,ue,dT,U1,F1);

% Calculation of damping ratio
%dzeta = (100*Ccom)/(2*sqrt(Mass*b));

% Isolation factor
IF = max(ddt)/max(ddte);


end
```

InputPulse.m

```
function [ddte,dte,ue,t] = InputPulse(Apulse,Tpulse,dT,time)
% This function creates an input pulse for the mass spring damper system

%Input argument
%Apulse     Amplitude of pulse
%Tpulse     duration of pulse
%dT         time step used for integration
%time       duration

global ddte
global dte
global ue
global t
```

```
14
15 Gstart = 0;
16 ddte(1) = Gstart;
17 dte(1) = 0;
18 ue(1) = 0;
19
20 t = 0:dT:time;
21
22 for i = 1:length(t)
23     if i≤(Tpulse/dT)
24             ddte(i+1)= (Apulse*sin(2*pi()/Tpulse*0.5*i*dT))+Gstart;
25             dte(i+1)= dte(i)+ddte(i)*dT;
26             ue(i+1)= ue(i)+dte(i)*dT;
27     else
28             ddte(i)=0;
29             dte(i)= dte(i−1)+ddte(i−1)*dT;
30             ue(i)= ue(i−1)+dte(i−1)*dT;
31     end
32
33 end
34
35 ddte2=ddte(0.5*Tpulse/dT:end);
36 ddte2(ddte2<0)=0;
37 ddte(0.5*Tpulse/dT:end)=ddte2;
38 end
```

Seat.m

```
1  function [ ddt,dt,u,Uspring,Fspring ] = Seat( Mass,Ccom,Cext,t,dte,ue,dT,U1,F1)
2  %UNTITLED2 Summary of this function goes here
3  %   Detailed explanation goes here
4
5  global u
6  global dt
7  global ddt
8  global Uspring
9  global Fspring
10
11 C=Ccom;
12 u(1)=0;
13 dt(1)=0;
14 Uspring(1) = ue(1)−u(1);
15 [Fspring(1)] = FuncSpring(U1,F1,Uspring(1));
16 ddt(1)=(1/Mass)*(−C*(dt(1)−dte(1))+Fspring(1));
17
18 for i=2:length(t)
19
20     dt(i)=dt(i−1)+ddt(i−1)*dT;
21     u(i)=u(i−1)+dt(i)*dT;
22
23     if dt(i)−dte(i)<0
24         C=Ccom;
25     else
26         C=Cext;
27     end
28
```

```
29      Uspring(i) = ue(i)-u(i);
30      [Fspring(i)] = FuncSpring(U1,F1,Uspring(i));
31
32      ddt(i)=(1/Mass)*(-C*(dt(i)-dte(i))+Fspring(i));
33
34  end
35
36
37
38
39  end
```

FuncSpring.m

```
1   function [ Fspring ] = FuncSpring( U1,F1,Uspring)
2   %UNTITLED3 Summary of this function goes here
3   %   Detailed explanation goes here
4
5   Fspring = interp1(U1,F1,Uspring,'linear','extrap');
6
7   % if Uspring≥0
8   %     Fspring = a*Uspring^2+b*Uspring+c;
9   % else
10  %     Fspring = d*Uspring;
11  % end
12
13  end
```

Appendix E

Abaqus Finite Element Models

Design31

```
*Heading
** Job name: Design31 Model name: Design31
** Generated by: Abaqus/CAE 6.14-1
*Preprint, echo=NO, model=NO, history=NO, contact=NO
**
** PARTS
**
*Part, name=Part-1
*End Part
**
**
** ASSEMBLY
**
*Assembly, name=Assembly
**
*Instance, name=Part-1-1, part=Part-1
*Node
      <845 nodes with their coordinates>
*Element, type=S4R
      <768 elements with their node numbers>
*Nset, nset=_PickedSet28, internal
   1,   2,   3,   4,   5,   6,  11,  12,  13,  14,  15,  16,  17,  18,  19,  20
  21,  22,  23,  24,  25,  26,  27,  28,  29,  30,  31,  32,  33,  34,  35,  36
  37,  38,  39,  40,  41,  42,  43,  44,  45,  46,  47,  48,  49,  50,  51,  52
  53,  54,  55, 186, 187, 188, 189, 190, 191, 192, 193, 194, 195, 196, 197, 198
 199, 200, 201, 202, 203, 204, 205, 206, 207, 208, 209, 210, 211, 212, 213, 214
 215, 216, 217, 218, 219, 220, 221, 222, 223, 224, 225, 226, 227, 228, 229, 230
 231, 232, 233, 234, 235, 236, 237, 238, 239, 240, 241, 242, 243, 244, 245, 246
 247, 248, 249, 250, 251
*Elset, elset=_PickedSet28, internal, generate
  1,  96,   1
*Nset, nset=_PickedSet46, internal
   2,   3,   5,   6,   7,   8,   9,  10,  11,  12,  13,  14,  15,  16,  17,  18
  19,  20,  21,  39,  40,  41,  42,  43,  44,  45,  46,  47,  48,  49,  56,  57
  58,  59,  60,  61,  62,  63,  64,  65,  66,  67,  68,  69,  70,  71,  72,  73
```

```
 74,  75,  76,  77,  78,  79,  80,  81,  82,  83,  84,  85,  86,  87,  88,  89
 90,  91,  92,  93,  94,  95,  96,  97,  98,  99, 100, 101, 102, 103, 104, 105
106, 107, 108, 109, 110, 111, 112, 113, 114, 115, 116, 117, 118, 119, 120, 121
122, 123, 124, 125, 126, 127, 128, 129, 130, 131, 132, 133, 134, 135, 136, 137
138, 139, 140, 141, 142, 143, 144, 145, 146, 147, 148, 149, 150, 151, 152, 153
154, 155, 156, 157, 158, 159, 160, 161, 162, 163, 164, 165, 166, 167, 168, 169
170, 171, 172, 173, 174, 175, 176, 177, 178, 179, 180, 181, 182, 183, 184, 185
252, 253, 254, 255, 256, 257, 258, 259, 260, 261, 262, 263, 264, 265, 266, 267
268, 269, 270, 271, 272, 273, 274, 275, 276, 277, 278, 279, 280, 281, 282, 283
284, 285, 286, 287, 288, 289, 290, 291, 292, 293, 294, 295, 296, 297, 298, 299
300, 301, 302, 303, 304, 305, 306, 307, 308, 309, 310, 311, 312, 313, 314, 315
316, 317, 318, 319, 320, 321, 322, 323, 324, 325, 326, 327, 328, 329, 330, 331
332, 333, 334, 335, 336, 337, 338, 339, 340, 341, 342, 343, 344, 345, 346, 347
348, 349, 350, 351, 352, 353, 354, 355, 356, 357, 358, 359, 360, 361, 362, 363
364, 365, 366, 367, 368, 369, 370, 371, 372, 373, 374, 375, 376, 377, 378, 379
380, 381, 382, 383, 384, 385, 386, 387, 388, 389, 390, 391, 392, 393, 394, 395
396, 397, 398, 399, 400, 401, 402, 403, 404, 405, 406, 407, 408, 409, 410, 411
412, 413, 414, 415, 416, 417, 418, 419, 420, 421, 422, 423, 424, 425, 426, 427
428, 429, 430, 431, 432, 433, 434, 435, 436, 437, 438, 439, 440, 441, 442, 443
444, 445, 446, 447, 448, 449, 450, 451, 452, 453, 454, 455, 456, 457, 458, 459
460, 461, 462, 463, 464, 465, 466, 467, 468, 469, 470, 471, 472, 473, 474, 475
476, 477, 478, 479, 480, 481, 482, 483, 484, 485, 486, 487, 488, 489, 490, 491
492, 493, 494, 495, 496, 497, 498, 499, 500, 501, 502, 503, 504, 505, 506, 507
508, 509, 510, 511, 512, 513, 514, 515, 516, 517, 518, 519, 520, 521, 522, 523
524, 525, 526, 527, 528, 529, 530, 531, 532, 533, 534, 535, 536, 537, 538, 539
540, 541, 542, 543, 544, 545, 546, 547, 548, 549, 550, 551, 552, 553, 554, 555
556, 557, 558, 559, 560, 561, 562, 563, 564, 565, 566, 567, 568, 569, 570, 571
572, 573, 574, 575, 576, 577, 578, 579, 580, 581, 582, 583, 584, 585, 586, 587
588, 589, 590, 591, 592, 593, 594, 595, 596, 597, 598, 599, 600, 601, 602, 603
604, 605, 606, 607, 608, 609, 610, 611, 612, 613, 614, 615, 616, 617, 618, 619
620, 621, 622, 623, 624, 625, 626, 627, 628, 629, 630, 631, 632, 633, 634, 635
636, 637, 638, 639, 640, 641, 642, 643, 644, 645, 646, 647, 648, 649, 650, 651
652, 653, 654, 655, 656, 657, 658, 659, 660, 661, 662, 663, 664, 665, 666, 667
668, 669, 670, 671, 672, 673, 674, 675, 676, 677, 678, 679, 680, 681, 682, 683
684, 685, 686, 687, 688, 689, 690, 691, 692, 693, 694, 695, 696, 697, 698, 699
700, 701, 702, 703, 704, 705, 706, 707, 708, 709, 710, 711, 712, 713, 714, 715
716, 717, 718, 719, 720, 721, 722, 723, 724, 725, 726, 727, 728, 729, 730, 731
732, 733, 734, 735, 736, 737, 738, 739, 740, 741, 742, 743, 744, 745, 746, 747
748, 749, 750, 751, 752, 753, 754, 755, 756, 757, 758, 759, 760, 761, 762, 763
764, 765, 766, 767, 768, 769, 770, 771, 772, 773, 774, 775, 776, 777, 778, 779
780, 781, 782, 783, 784, 785, 786, 787, 788, 789, 790, 791, 792, 793, 794, 795
796, 797, 798, 799, 800, 801, 802, 803, 804, 805, 806, 807, 808, 809, 810, 811
812, 813, 814, 815, 816, 817, 818, 819, 820, 821, 822, 823, 824, 825, 826, 827
828, 829, 830, 831, 832, 833, 834, 835, 836, 837, 838, 839, 840, 841, 842, 843
844, 845
*Elset, elset=_PickedSet46, internal, generate
  97,  768,    1
** Section: Section-1
*Shell Section, elset=_PickedSet28, material=GRPM10E
0.006, 5
*Orientation, name=Ori-1
0.866025403784439,          0.5,           0.,           0.,           0., ...
             -1.
3, 0.
** Region: (CompositeLayup-1-1: Generated From Layup)
*Elset, elset=CompositeLayup-1-1, generate
  97,  768,    1
** Section: CompositeLayup-1-1
*Shell Section, elset=CompositeLayup-1-1, composite, orientation=Ori-1, ...
    layup=CompositeLayup-1
0.00075, 3, GRPM10E, 45., Ply-1
```

```
0.00075, 3, GRPM10E, -45., Ply-2
0.00075, 3, GRPM10E, 90., Ply-3
0.00075, 3, GRPM10E, 0., Ply-4
0.00075, 3, GRPM10E, 0., Ply-5
0.00075, 3, GRPM10E, 90., Ply-6
0.00075, 3, GRPM10E, -45., Ply-7
0.00075, 3, GRPM10E, 45., Ply-8
*End Instance
**
*Node
      1,  0.303108901,  0.275000006,  0.075000003
*Nset, nset=_PickedSet24, internal
 1,
*Nset, nset=_PickedSet25, internal, instance=Part-1-1
   1,   2,   3,   4,   5,   6,  11,  12,  13,  14,  15,  16,  17,  18,  19,  20
  21,  22,  23,  24,  25,  26,  27,  28,  29,  30,  31,  32,  33,  34,  35,  36
  37,  38,  39,  40,  41,  42,  43,  44,  45,  46,  47,  48,  49,  50,  51,  52
  53,  54,  55, 186, 187, 188, 189, 190, 191, 192, 193, 194, 195, 196, 197, 198
 199, 200, 201, 202, 203, 204, 205, 206, 207, 208, 209, 210, 211, 212, 213, 214
 215, 216, 217, 218, 219, 220, 221, 222, 223, 224, 225, 226, 227, 228, 229, 230
 231, 232, 233, 234, 235, 236, 237, 238, 239, 240, 241, 242, 243, 244, 245, 246
 247, 248, 249, 250, 251
*Elset, elset=_PickedSet25, internal, instance=Part-1-1, generate
  1,  96,   1
*Nset, nset=_PickedSet27, internal, instance=Part-1-1
   7,   8,   9,  10,  83,  84,  85,  86,  87,  88,  89,  90,  91,  92,  93, 148
 149, 150, 151, 152, 153, 154, 155, 156, 157, 158
*Elset, elset=_PickedSet27, internal, instance=Part-1-1, generate
 124,  768,   28
*Elset, elset=__PickedSurf26_E4, internal, instance=Part-1-1, generate
  1,  12,   1
*Surface, type=ELEMENT, name=_PickedSurf26, internal
__PickedSurf26_E4, E4
** Constraint: Constraint-1
*Rigid Body, ref node=_PickedSet24, elset=_PickedSet25
*End Assembly
**
** MATERIALS
**
*Material, name=GRP7781
*Elastic, type=LAMINA
 2.97e+10, 2.97e+10,     0.17,  5.3e+09,  5.3e+09,  4.3e+09
*Fail Stress
 3.67e+08, 5.49e+08, 3.67e+08, 5.49e+08, 9.71e+07,       0.,       0.
*Material, name=GRPM10E
*Elastic, type=LAMINA
 2.45e+10, 2.38e+10,     0.11,  4.7e+09,  2.6e+09,  3.6e+09
*Fail Stress
 4.33e+08, 3.77e+08, 3.86e+08, 3.35e+08,  8.4e+07,       0.,       0.
** ----------------------------------------------------------------
**
** STEP: Riks
**
*Step, name=Riks, nlgeom=YES
*Static, riks
1., 1., 1e-05, 5., ,
**
** BOUNDARY CONDITIONS
**
** Name: BC-1 Type: Symmetry/Antisymmetry/Encastre
*Boundary
```

```
_PickedSet27, ENCASTRE
**
** LOADS
**
** Name: Load-1   Type: Shell edge load
*Dsload
_PickedSurf26, EDNOR, 150.
**
** OUTPUT REQUESTS
**
*Restart, write, frequency=0
**
** FIELD OUTPUT: F-Output-2
**
*Output, field
*Element Output, elset=Part-1-1.CompositeLayup-1-1, directions=YES
2, 5, 8, 11, 14, 17, 20, 23
CFAILURE, LE, PE, PEEQ, PEMAG, S
**
** FIELD OUTPUT: F-Output-1
**
*Output, field, variable=PRESELECT
**
** HISTORY OUTPUT: H-Output-2
**
*Output, history
*Element Output, elset=Part-1-1.CompositeLayup-1-1
2, 5, 8, 11, 14, 17, 20, 23
TSAIH,
**
** HISTORY OUTPUT: H-Output-1
**
*Output, history, variable=PRESELECT
*End Step
```

Design32

```
*Heading
** Job name: Design32 Model name: Design32
** Generated by: Abaqus/CAE 6.14-1
*Preprint, echo=NO, model=NO, history=NO, contact=NO
**
** PARTS
**
*Part, name=Part-1
*End Part
**
**
** ASSEMBLY
**
*Assembly, name=Assembly
**
*Instance, name=Part-1-1, part=Part-1
*Node
      <1010 nodes with their coordinates>
*Element, type=S4R
```

```
      <909 elements with their nodes>
*Nset, nset=_PickedSet46, internal
   1,   2,   3,   4,   5,   6,   7,   8,  10,  11,  13,  14,  17,  18,  39,  40
  41,  42,  43,  44,  45,  46,  67,  68,  69,  70,  71,  72,  73,  74,  75,  76
  77,  78,  79,  80,  81,  82,  83,  84,  85,  86,  87,  88,  89,  90, 111, 112
 113, 114, 115, 116, 117, 118, 139, 140, 141, 142, 143, 144, 145, 146, 167, 168
 169, 170, 171, 172, 173, 174, 203, 204, 205, 206, 207, 208, 209, 210, 211, 212
 213, 214, 215, 216, 217, 218, 267, 268, 269, 270, 271, 272, 273, 274, 435, 436
 437, 438, 439, 440, 441, 442, 443, 444, 445, 446, 447, 448, 449, 450, 451, 452
 453, 454, 455, 456, 457, 458, 459, 460, 461, 462, 463, 464, 465, 466, 627, 628
 629, 630, 631, 632, 633, 634, 635, 636, 637, 638, 639, 640, 641, 642, 643, 644
 645, 646, 647, 648, 649, 650, 651, 652, 653, 654, 655, 656, 657, 658, 819, 820
 821, 822, 823, 824, 825, 826, 827, 828, 829, 830, 831, 832, 833, 834, 835, 836
 837, 838, 839, 840, 841, 842, 843, 844, 845, 846, 847, 848, 849, 850
*Elset, elset=_PickedSet46, internal
 190, 191, 192, 193, 194, 195, 196, 197, 198, 199, 200, 201, 202, 203, 204, 205
 206, 207, 208, 209, 210, 211, 212, 213, 214, 215, 216, 217, 218, 219, 220, 221
 222, 223, 224, 225, 226, 227, 228, 229, 230, 231, 232, 233, 234, 424, 425, 426
 427, 428, 429, 430, 431, 432, 433, 434, 435, 436, 437, 438, 439, 440, 441, 442
 443, 444, 445, 446, 447, 448, 449, 450, 451, 452, 453, 454, 455, 456, 457, 458
 459, 460, 461, 462, 463, 464, 465, 466, 467, 468, 658, 659, 660, 661, 662, 663
 664, 665, 666, 667, 668, 669, 670, 671, 672, 673, 674, 675, 676, 677, 678, 679
 680, 681, 682, 683, 684, 685, 686, 687, 688, 689, 690, 691, 692, 693, 694, 695
 696, 697, 698, 699, 700, 701, 702, 892, 893, 894, 895, 896, 897, 898, 899, 900
 901, 902, 903, 904, 905, 906, 907, 908, 909
*Orientation, name=Ori-1
0.866025403784439,          0.5,           0.,           0.,           0., ...
             -1.
3, 0.
** Region: (CompositeLayup-1-1: Generated From Layup), (Controls:EC-1)
*Elset, elset=CompositeLayup-1-1
   1,   2,   3,   4,   5,   6,   7,   8,   9,  10,  11,  12,  13,  14,  15,  16
  17,  18,  19,  20,  21,  22,  23,  24,  25,  26,  27,  28,  29,  30,  31,  32
  33,  34,  35,  36,  37,  38,  39,  40,  41,  42,  43,  44,  45,  46,  47,  48
  49,  50,  51,  52,  53,  54,  55,  56,  57,  58,  59,  60,  61,  62,  63,  64
  65,  66,  67,  68,  69,  70,  71,  72,  73,  74,  75,  76,  77,  78,  79,  80
  81,  82,  83,  84,  85,  86,  87,  88,  89,  90,  91,  92,  93,  94,  95,  96
  97,  98,  99, 100, 101, 102, 103, 104, 105, 106, 107, 108, 109, 110, 111, 112
 113, 114, 115, 116, 117, 118, 119, 120, 121, 122, 123, 124, 125, 126, 127, 128
 129, 130, 131, 132, 133, 134, 135, 136, 137, 138, 139, 140, 141, 142, 143, 144
 145, 146, 147, 148, 149, 150, 151, 152, 153, 154, 155, 156, 157, 158, 159, 160
 161, 162, 163, 164, 165, 166, 167, 168, 169, 170, 171, 172, 173, 174, 175, 176
 177, 178, 179, 180, 181, 182, 183, 184, 185, 186, 187, 188, 189, 235, 236, 237
 238, 239, 240, 241, 242, 243, 244, 245, 246, 247, 248, 249, 250, 251, 252, 253
 254, 255, 256, 257, 258, 259, 260, 261, 262, 263, 264, 265, 266, 267, 268, 269
 270, 271, 272, 273, 274, 275, 276, 277, 278, 279, 280, 281, 282, 283, 284, 285
 286, 287, 288, 289, 290, 291, 292, 293, 294, 295, 296, 297, 298, 299, 300, 301
 302, 303, 304, 305, 306, 307, 308, 309, 310, 311, 312, 313, 314, 315, 316, 317
 318, 319, 320, 321, 322, 323, 324, 325, 326, 327, 328, 329, 330, 331, 332, 333
 334, 335, 336, 337, 338, 339, 340, 341, 342, 343, 344, 345, 346, 347, 348, 349
 350, 351, 352, 353, 354, 355, 356, 357, 358, 359, 360, 361, 362, 363, 364, 365
 366, 367, 368, 369, 370, 371, 372, 373, 374, 375, 376, 377, 378, 379, 380, 381
 382, 383, 384, 385, 386, 387, 388, 389, 390, 391, 392, 393, 394, 395, 396, 397
 398, 399, 400, 401, 402, 403, 404, 405, 406, 407, 408, 409, 410, 411, 412, 413
 414, 415, 416, 417, 418, 419, 420, 421, 422, 423
** Section: CompositeLayup-1-1
*Shell Section, elset=CompositeLayup-1-1, composite, orientation=Ori-1, ...
    controls=EC-1, layup=CompositeLayup-1
0.00075, 3, GRPM10E, 0., Ply-1
0.00075, 3, GRPM10E, 90., Ply-2
0.00075, 3, GRPM10E, -45., Ply-3
```

```
0.00075, 3, GRPM10E, 45., Ply-4
0.00075, 3, GRPM10E, 45., Ply-5
0.00075, 3, GRPM10E, -45., Ply-6
0.00075, 3, GRPM10E, 90., Ply-7
0.00075, 3, GRPM10E, 0., Ply-8
** Section: Section-1
*Shell Section, elset=_PickedSet46, material=GRP7781
0.05, 5
*Orientation, name=Ori-2
0.866025403784439,         -0.5,           0.,           0.,           0., ...
             -1.
3, 0.
** Region: (CompositeLayup-1-Copy-1: Generated From Layup), (Controls:EC-1)
*Elset, elset=CompositeLayup-1-Copy-1
 469, 470, 471, 472, 473, 474, 475, 476, 477, 478, 479, 480, 481, 482, 483, 484
 485, 486, 487, 488, 489, 490, 491, 492, 493, 494, 495, 496, 497, 498, 499, 500
 501, 502, 503, 504, 505, 506, 507, 508, 509, 510, 511, 512, 513, 514, 515, 516
 517, 518, 519, 520, 521, 522, 523, 524, 525, 526, 527, 528, 529, 530, 531, 532
 533, 534, 535, 536, 537, 538, 539, 540, 541, 542, 543, 544, 545, 546, 547, 548
 549, 550, 551, 552, 553, 554, 555, 556, 557, 558, 559, 560, 561, 562, 563, 564
 565, 566, 567, 568, 569, 570, 571, 572, 573, 574, 575, 576, 577, 578, 579, 580
 581, 582, 583, 584, 585, 586, 587, 588, 589, 590, 591, 592, 593, 594, 595, 596
 597, 598, 599, 600, 601, 602, 603, 604, 605, 606, 607, 608, 609, 610, 611, 612
 613, 614, 615, 616, 617, 618, 619, 620, 621, 622, 623, 624, 625, 626, 627, 628
 629, 630, 631, 632, 633, 634, 635, 636, 637, 638, 639, 640, 641, 642, 643, 644
 645, 646, 647, 648, 649, 650, 651, 652, 653, 654, 655, 656, 657, 703, 704, 705
 706, 707, 708, 709, 710, 711, 712, 713, 714, 715, 716, 717, 718, 719, 720, 721
 722, 723, 724, 725, 726, 727, 728, 729, 730, 731, 732, 733, 734, 735, 736, 737
 738, 739, 740, 741, 742, 743, 744, 745, 746, 747, 748, 749, 750, 751, 752, 753
 754, 755, 756, 757, 758, 759, 760, 761, 762, 763, 764, 765, 766, 767, 768, 769
 770, 771, 772, 773, 774, 775, 776, 777, 778, 779, 780, 781, 782, 783, 784, 785
 786, 787, 788, 789, 790, 791, 792, 793, 794, 795, 796, 797, 798, 799, 800, 801
 802, 803, 804, 805, 806, 807, 808, 809, 810, 811, 812, 813, 814, 815, 816, 817
 818, 819, 820, 821, 822, 823, 824, 825, 826, 827, 828, 829, 830, 831, 832, 833
 834, 835, 836, 837, 838, 839, 840, 841, 842, 843, 844, 845, 846, 847, 848, 849
 850, 851, 852, 853, 854, 855, 856, 857, 858, 859, 860, 861, 862, 863, 864, 865
 866, 867, 868, 869, 870, 871, 872, 873, 874, 875, 876, 877, 878, 879, 880, 881
 882, 883, 884, 885, 886, 887, 888, 889, 890, 891
** Section: CompositeLayup-1-Copy-1
*Shell Section, elset=CompositeLayup-1-Copy-1, composite, orientation=Ori-2, ...
    controls=EC-1, layup=CompositeLayup-1-Copy
0.00075, 3, GRPM10E, 0., Ply-1
0.00075, 3, GRPM10E, 90., Ply-2
0.00075, 3, GRPM10E, -45., Ply-3
0.00075, 3, GRPM10E, 45., Ply-4
0.00075, 3, GRPM10E, 45., Ply-5
0.00075, 3, GRPM10E, -45., Ply-6
0.00075, 3, GRPM10E, 90., Ply-7
0.00075, 3, GRPM10E, 0., Ply-8
*End Instance
**
*Node
      1,  0.303108901,  0.264999986,  0.075000003
*Node
      2,           0., 0.0900000036,  0.075000003
*Nset, nset=_PickedSet56, internal
 1,
*Nset, nset=_PickedSet58, internal
 2,
*Nset, nset=_PickedSet59, internal, instance=Part-1-1
   1,   4,   7,   8,  10,  11,  13,  14,  67,  68,  69,  70,  71,  72,  73,  74
```

```
 111, 112, 113, 114, 115, 116, 117, 118, 139, 140, 141, 142, 143, 144, 145, 146
 167, 168, 169, 170, 171, 172, 173, 174, 203, 204, 205, 206, 207, 208, 209, 210
 211, 212, 213, 214, 215, 216, 217, 218, 627, 628, 629, 630, 631, 632, 633, 634
 635, 636, 637, 638, 639, 640, 641, 642, 643, 644, 645, 646, 647, 648, 649, 650
 651, 652, 653, 654, 655, 656, 657, 658, 819, 820, 821, 822, 823, 824, 825, 826
 827, 828, 829, 830, 831, 832, 833, 834, 835, 836, 837, 838, 839, 840, 841, 842
 843, 844, 845, 846, 847, 848, 849, 850
*Elset, elset=_PickedSet59, internal, instance=Part-1-1
 424, 425, 426, 427, 428, 429, 430, 431, 432, 433, 434, 435, 436, 437, 438, 439
 440, 441, 442, 443, 444, 445, 446, 447, 448, 449, 450, 451, 452, 453, 454, 455
 456, 457, 458, 459, 460, 461, 462, 463, 464, 465, 466, 467, 468, 658, 659, 660
 661, 662, 663, 664, 665, 666, 667, 668, 669, 670, 671, 672, 673, 674, 675, 676
 677, 678, 679, 680, 681, 682, 683, 684, 685, 686, 687, 688, 689, 690, 691, 692
 693, 694, 695, 696, 697, 698, 699, 700, 701, 702, 892, 893, 894, 895, 896, 897
 898, 899, 900
*Nset, nset=_PickedSet62, internal, instance=Part-1-1
   9,  12,  15,  16, 195, 196, 197, 198, 199, 200, 201, 202, 239, 240, 241, 242
 243, 244, 245, 246
*Elset, elset=_PickedSet62, internal, instance=Part-1-1
 469, 490, 511, 532, 553, 574, 595, 616, 637, 723, 744, 765, 786, 807, 828, 849
 870, 891
*Nset, nset=_PickedSet63, internal, instance=Part-1-1
   2,   3,   5,   6,  17,  18,  39,  40,  41,  42,  43,  44,  45,  46,  75,  76
  77,  78,  79,  80,  81,  82,  83,  84,  85,  86,  87,  88,  89,  90, 267, 268
 269, 270, 271, 272, 273, 274, 435, 436, 437, 438, 439, 440, 441, 442, 443, 444
 445, 446, 447, 448, 449, 450, 451, 452, 453, 454, 455, 456, 457, 458, 459, 460
 461, 462, 463, 464, 465, 466
*Elset, elset=_PickedSet63, internal, instance=Part-1-1
 190, 191, 192, 193, 194, 195, 196, 197, 198, 199, 200, 201, 202, 203, 204, 205
 206, 207, 208, 209, 210, 211, 212, 213, 214, 215, 216, 217, 218, 219, 220, 221
 222, 223, 224, 225, 226, 227, 228, 229, 230, 231, 232, 233, 234, 901, 902, 903
 904, 905, 906, 907, 908, 909
*Elset, elset=__PickedSurf60_E2, internal, instance=Part-1-1, generate
 194,  234,    5
*Surface, type=ELEMENT, name=_PickedSurf60, internal
__PickedSurf60_E2, E2
*Elset, elset=__PickedSurf61_E2, internal, instance=Part-1-1, generate
 901,  909,    1
*Surface, type=ELEMENT, name=_PickedSurf61, internal
__PickedSurf61_E2, E2
*Elset, elset=__PickedSurf64_E4, internal, instance=Part-1-1, generate
 901,  909,    1
*Surface, type=ELEMENT, name=_PickedSurf64, internal
__PickedSurf64_E4, E4
** Constraint: Constraint-1
*Rigid Body, ref node=_PickedSet56, elset=_PickedSet63
** Constraint: Constraint-2
*Rigid Body, ref node=_PickedSet58, elset=_PickedSet59
*End Assembly
**
** ELEMENT CONTROLS
**
*Section Controls, name=EC-1, second order accuracy=YES
1., 1., 1.
**
** MATERIALS
**
*Material, name=GRP7781
*Elastic, type=LAMINA
 2.97e+10, 2.97e+10,     0.17,  5.3e+09,  5.3e+09,  4.3e+09
*Fail Stress
```

```
 3.67e+08, 5.49e+08, 3.67e+08, 5.49e+08, 9.71e+07,       0.,       0.
*Material, name=GRPM10E
*Elastic, type=LAMINA
 2.45e+10, 2.38e+10,     0.11,  4.7e+09,  2.6e+09,  3.6e+09
*Fail Stress
 4.33e+08, 3.77e+08, 3.86e+08, 3.35e+08,  8.4e+07,       0.,       0.
** ----------------------------------------------------------------
**
** STEP: Riks
**
*Step, name=Riks, nlgeom=YES, inc=60
*Static, riks
1., 1., 1e-05, 25., ,
**
** BOUNDARY CONDITIONS
**
** Name: BC-1 Type: Symmetry/Antisymmetry/Encastre
*Boundary
_PickedSet62, ENCASTRE
**
** LOADS
**
** Name: Load-1   Type: Shell edge load
*Dsload
_PickedSurf64, EDNOR, 30.
**
** OUTPUT REQUESTS
**
*Restart, write, frequency=0
**
** FIELD OUTPUT: F-Output-1
**
*Output, field
*Element Output, elset=Part-1-1.CompositeLayup-1-1, directions=YES
2, 5, 8, 11, 14, 17, 20, 23
CFAILURE, LE, PE, PEEQ, PEMAG, S
**
** FIELD OUTPUT: F-Output-3
**
*Element Output, elset=Part-1-1.CompositeLayup-1-Copy-1, directions=YES
2, 5, 8, 11, 14, 17, 20, 23
CFAILURE, LE, PE, PEEQ, PEMAG, S
**
** FIELD OUTPUT: F-Output-2
**
*Output, field, variable=PRESELECT
**
** HISTORY OUTPUT: H-Output-1
**
*Output, history
*Element Output, elset=Part-1-1.CompositeLayup-1-1
2, 5, 8, 11, 14, 17, 20, 23
TSAIH,
**
** HISTORY OUTPUT: H-Output-3
**
*Element Output, elset=Part-1-1.CompositeLayup-1-Copy-1
2, 5, 8, 11, 14, 17, 20, 23
TSAIH,
**
** HISTORY OUTPUT: H-Output-2
```

```
260 **
261 *Output, history, variable=PRESELECT
262 *End Step
```

Appendix F

MatLab drop test data reader

DataLoader.m

```
clc
clear all
close all
A = 0;
B = 0;
% known bug: GCDC ullman = GCDC sigma!!!!

% Data loader KNRM drop test 5-10-2017
% Ullman standard vs Sigma Seat
% 8 tri axis recorders -> 24 channels
% Channel 0 - Base of boat at sigmaseat - vertical plane down positive
% Channel 1 - Base of boat at sigmaseat - long. direction bow positive
% Channel 2 - Base of boat at sigmaseat - trans. direction portside pos.
% Channel 3 - Ullman longitudinal direction stern positive
% Channel 4 - Ullman vertical plane up positive
% Channel 5 - Ullman transversal direction portside positive
% Channel 6 - Sigma seat longitudnal direction bow positive
% Channel 7 - Sigma seat vertical plane up positive
% Channel 8 - Sigma seat transversal direction starboard


% Processing first DAT file 17100507

% Open file and get file ID
fileID = fopen('Block1.DAT','r');
[filename,permission,machineformat,encoding] = fopen(fileID);

% Enable to load ALL GPS data
% Longitude = fread(fileID,[1030,1],'float32',28812);
% fseek(fileID,4,'bof');
% Latitude = fread(fileID,[1030,1],'float32',28812);
% fseek(fileID,8,'bof');
% Speed = fread(fileID,[1030,1],'int16',28814);
% fseek(fileID,10,'bof');
% Cog = fread(fileID,[1030,1],'int16',28814);
```

```
36
37 % Loading ALL Timestamp data (note timestamp 300-600Hz bug!
38 fseek(fileID,12,'bof');
39 Timestamp = fread(fileID,[1030,1],'int32',28812);
40
41 % Loading Channel 0,1 and 2
42 for A = 1:1:1024
43
44 fseek(fileID,16+28816*(A-1),'bof');
45 CH0(:,A) = fread(fileID,[600,1],'int16',46);
46
47 end
48 for A = 1:1:1024
49
50 fseek(fileID,18+28816*(A-1),'bof');
51 CH1(:,A) = fread(fileID,[600,1],'int16',46);
52
53 end
54 for A = 1:1:1024
55
56 fseek(fileID,20+28816*(A-1),'bof');
57 CH2(:,A) = fread(fileID,[600,1],'int16',46);
58
59 end
60
61 % Loading channel 3,4,5
62 for A = 1:1:1024
63
64 fseek(fileID,22+28816*(A-1),'bof');
65 CH3(:,A) = fread(fileID,[600,1],'int16',46);
66
67 end
68 for A = 1:1:1024
69
70 fseek(fileID,24+28816*(A-1),'bof');
71 CH4(:,A) = fread(fileID,[600,1],'int16',46);
72
73 end
74 for A = 1:1:1024
75
76 fseek(fileID,26+28816*(A-1),'bof');
77 CH5(:,A) = fread(fileID,[600,1],'int16',46);
78
79 end
80
81 % Loading channel 6,7,8
82 for A = 1:1:1024
83
84 fseek(fileID,28+28816*(A-1),'bof');
85 CH6(:,A) = fread(fileID,[600,1],'int16',46);
86
87 end
88 for A = 1:1:1024
89
90 fseek(fileID,30+28816*(A-1),'bof');
91 CH7(:,A) = fread(fileID,[600,1],'int16',46);
92
93 end
94 for A = 1:1:1024
95
96 fseek(fileID,32+28816*(A-1),'bof');
```

```
97  CH8(:,A) = fread(fileID,[600,1],'int16',46);
98
99  end
100
101 % Manipulate data Channel 1,2 and 3
102 CH0 = reshape(CH0,[600*1024,1]);
103 CH1 = reshape(CH1,[600*1024,1]);
104 CH2 = reshape(CH2,[600*1024,1]);
105
106 % Manipulate data Chanel 4,5,6
107 CH3 = reshape(CH3,[600*1024,1]);
108 CH4 = reshape(CH4,[600*1024,1]);
109 CH5 = reshape(CH5,[600*1024,1]);
110
111 % Manipulate data chanel 7,8,9
112 CH6 = reshape(CH6,[600*1024,1]);
113 CH7 = reshape(CH7,[600*1024,1]);
114 CH8 = reshape(CH8,[600*1024,1]);
115
116 % Manipulate timeaxis
117 timeaxis = 0:1/600:1024-(1/600);
118
119 % Close the file
120 fclose(fileID);
121
122 % Continuing with Lord recorders
123 % Lord drop 1
124 Lord1 = xlsread('LordPrototypeSigmaDrops.xlsx',1,'B2:B9661');
125 Lord2 = xlsread('LordPrototypeSigmaDrops.xlsx',1,'C2:C9661');
126 lordtime = xlsread('LordPrototypeSigmaDrops.xlsx',1,'F2:F9661');
127 lordtime = lordtime+897.305-2.72; % translation of timeaxis for plot purpose
128 Drop1Lord1(:,1) = lordtime;
129 Drop1Lord1(:,2) = Lord1;
130 Drop1Lord2(:,1) = lordtime;
131 Drop1Lord2(:,2) = Lord2;
132 Drop1Lord1(any(isnan(Drop1Lord1), 2), :) = [];
133 Drop1Lord2(any(isnan(Drop1Lord2), 2), :) = [];
134 % Lord drop 2
135 Drop2Lord1(:,1) = xlsread('LordPrototypeSigmaDrops.xlsx',1,'L2:L30721');
136 Drop2Lord1(:,2) = xlsread('LordPrototypeSigmaDrops.xlsx',1,'I2:I30721');
137 % Lord drop 3
138 Drop3Lord1(:,1) = xlsread('LordPrototypeSigmaDrops.xlsx',1,'R2:R4872');
139 Drop3Lord1(:,2) = xlsread('LordPrototypeSigmaDrops.xlsx',1,'O2:O4872');
140
141
142 % continuing with GCDC recorders
143 GCDCbase1 = csvread('GCDCdataBase1.csv',9);
144 GCDCbase2 = csvread('GCDCdataBase2.csv',9);
145 GCDCullman = csvread('GCDCdataUllman.csv',9);
146 GCDCsigma = csvread('GCDCdataSigma.csv',9);
147
148 GCDCbase1time = GCDCbase1(:,1);%-(1144.97-897.32);
149 GCDCullmantime = GCDCullman(:,1);%-(1163.50-897.32);
150 GCDCsigmatime = GCDCsigma(:,1);%-(1124.66-897.31);
151
152 % Plot overlap of all z-channels after filtering
153 % Savitzky Golay filtering of channels 0,4,7 and Lord1
154 windowWidth = 35;
155 polynomialOrder = 2;
156 smoothCH0 = sgolayfilt(CH0, polynomialOrder, windowWidth);
157 smoothCH4 = sgolayfilt(CH4, polynomialOrder, windowWidth);
```

```
158 smoothCH7 = sgolayfilt(CH7, polynomialOrder, windowWidth);
159 smoothLord1 = sgolayfilt(Drop1Lord1(:,2), polynomialOrder, windowWidth);
160 smoothGCDCbase1 = sgolayfilt(GCDCbase1(:,4), polynomialOrder, windowWidth);
161 smoothGCDCullman = sgolayfilt(GCDCullman(:,2), polynomialOrder, windowWidth);
162 smoothGCDCsigma = sgolayfilt(GCDCsigma(:,2), polynomialOrder, windowWidth);
163
164 figure(1)
165 hold on
166 plot(timeaxis,smoothCH0/100*-1,timeaxis,smoothCH4/100*-1,timeaxis,smoothCH7/100*-1)
167 legend('Base MARECS','Ullman MARECS','Sigma MARECS')
168 hold off
169 figure(2)
170 hold on
171 plot(Lordtime1(:,1),smoothLord1*10,Lordtime2(:,1),Lordtime2(:,2)*-10)
172 legend('Lord Sigma','Lord Base')
173 hold off
174 figure(3)
175 hold on
176 plot(GCDCsigmatime,smoothGCDCsigma*-1/2048,GCDCullmantime,smoothGCDCullman*-1/2048,GCDCbase1ti
177 legend('GCDC Ullman','GCDC Sigma','GCDC Base')
178 hold off
```

Appendix G

Graphical results drop test IJmuiden

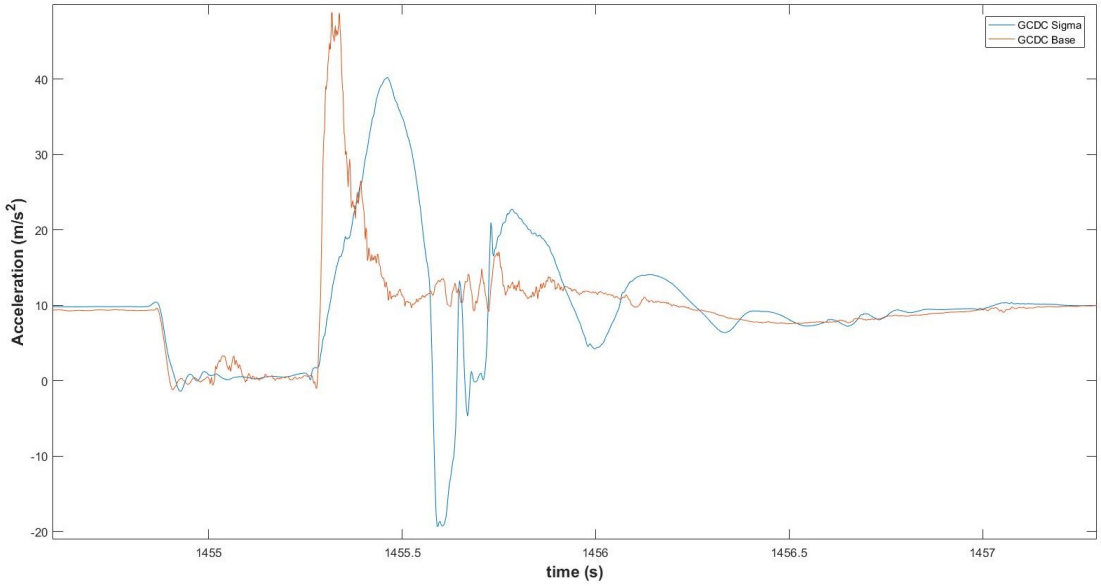

Figure G.1: Second drop GCDC recorder

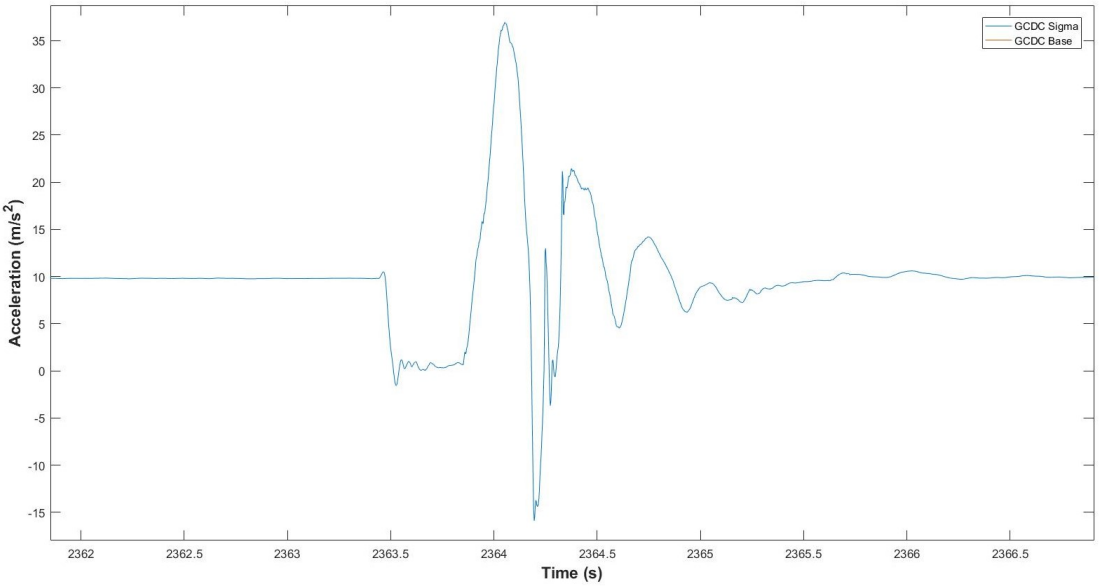

Figure G.2: Third drop GCDC recorder

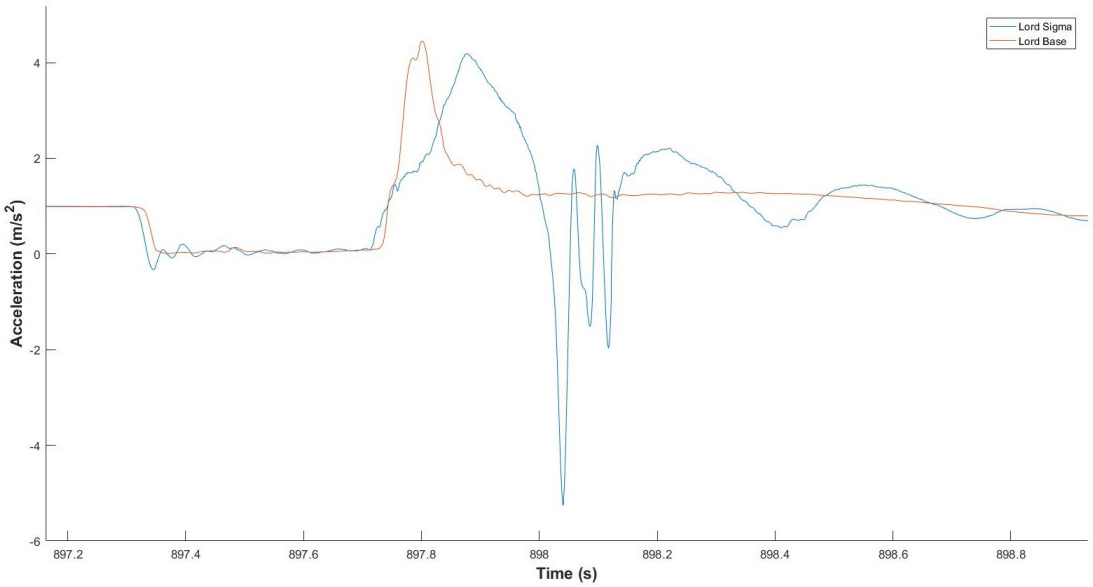

Figure G.3: First drop LORD recorder

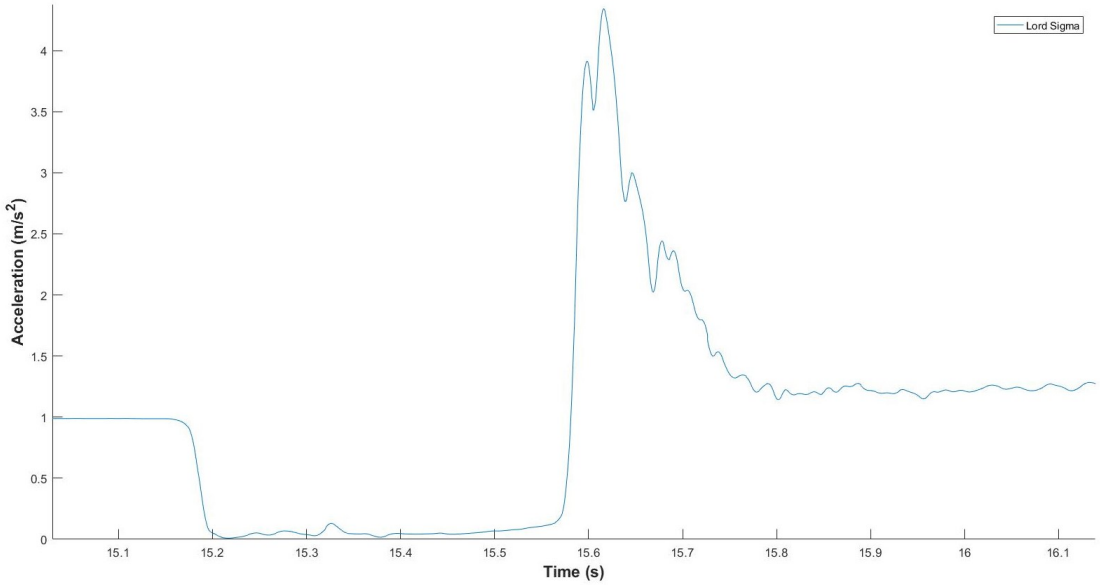

Figure G.4: Second drop LORD recorder

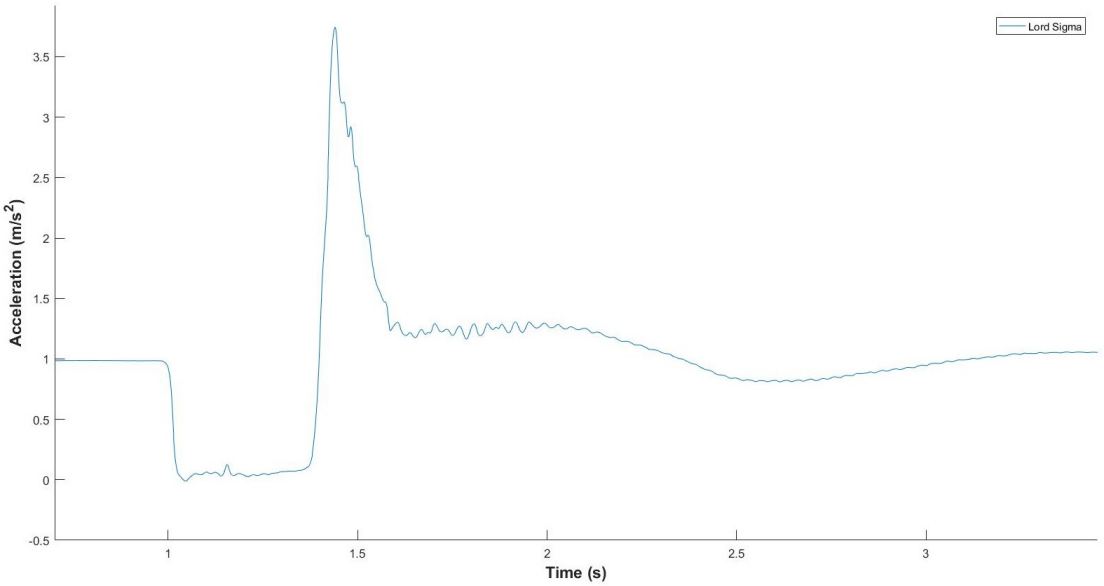

Figure G.5: Third drop LORD recorder